SPACEBORNE MULTIBASELINE SAR TOMOGRAPHY FOR RETRIEVING FOREST HEIGHTS

A DISSERTATION
SUBMITTED TO THE DEPARTMENT OF ELECTRICAL
ENGINEERING
AND THE COMMITTEE ON GRADUATE STUDIES
OF STANFORD UNIVERSITY
IN PARTIAL FULFILLMENT OF THE REQUIREMENTS
FOR THE DEGREE OF
DOCTOR OF PHILOSOPHY

Qiuhua Lin
March 2017

I certify that I have read this dissertation and that, in my opinion, it is fully adequate in scope and quality as a dissertation for the degree of Doctor of Philosophy.

(Howard Zebker) Principal Adviser

I certify that I have read this dissertation and that, in my opinion, it is fully adequate in scope and quality as a dissertation for the degree of Doctor of Philosophy.

(John Pauly)

I certify that I have read this dissertation and that, in my opinion, it is fully adequate in scope and quality as a dissertation for the degree of Doctor of Philosophy.

(Ivan Linscott)

Approved for the Stanford University Committee on Graduate Studies

Abstract

Climate change is perhaps the biggest challenge of our time, impacting all life on Earth. During the last 50-100 years, changes in global climate have been much bigger and happened much faster than any such changes the planet has ever seen in recorded human history. Forests play a key role in the global carbon cycle, and hence in the global climate. The yearly carbon flux from forests to atmosphere is still an order of magnitude greater than that from human activities. However, the role of forests remains poorly quantitatively characterized as compared to other ecosystems, due to the practical difficulties in measuring forest biomass stocks globally. Without a quantitative model of the global carbon cycle, sensible policies and actions can be hard to make.

Synthetic aperture radar (SAR) is a promising candidate for measuring forest biomass. Since low frequency microwaves penetrate the forest canopy, SAR systems operating at low frequencies can provide essential information in the elevation direction for assessing the forest biomass. In addition, a significant number of satellites equipped with SAR sensors will be scheduled and launched in the next five to ten years. Vast amounts of image data will be generated by current and future spaceborne SAR systems. This calls for new algorithms to exploit the diverse SAR images for forest mapping.

In this thesis, we present a new technology, called SAR tomography, to retrieve forest heights. SAR tomography utilizes multiple images acquired from slightly different orbital locations to form a synthetic aperture in the elevation direction. Hence, it can achieve a full three dimentional (3-D) reconstruction of the imaged scenes.

We first introduce the basic concepts of the SAR imaging system, and then establish the signal model for SAR tomography. Based on the signal model, we propose the Capon beamformer as the reconstruction algorithm and test its performance via simulation. In the second part, we investigate particular problems when using spaceborne repeat-pass SAR systems on forest areas, including phase errors, forest distributed scatterers and temporal decorrelation. For each problem, we propose a mitigation method and evaluate the performance via simulation. In the last part, we show two case studies using the proposed SAR tomography to reconstruct the elevation profiles in urban and forest areas. The SAR images used in this thesis are from the Advanced Land and Ocean Sensor (ALOS).

Acknowledgement

Pursuing a doctoral degree is an amazing journey, especially in the sunny and beautiful Stanford campus. The joy of the journey comes from exploring the unknown, exchanging ideas with the brightest minds and the ultimate intellectual freedom to venture out in any direction. However, it is not an easy one, with challenging research problems, loneliness and even self doubt. In those dark moments, I realize the importance of the guidance from the experienced, unconditional love from family and warm companionship from close friends. I am so grateful to have all of these along the journey.

First and for most, I own the most credit to my beloved adviser, Prof. Howard Zebker. His amazing work got me interested in this field when I was still a undergraduate in China. Even with such a fame and prestige, he is one of the most friendly and accessible professors to work with. Since I started working with him, Prof. Zebker has always been patiently guiding me along the way, teaching me how to think systematically, scientifically, and helping me formulate and solve meaningful research questions. Prof. Zebker is also a good educator, loving to work with students and answering all the questions. Taking his lectures is a great pleasure. During the classes, Prof. Zebker turns the complicate radar technology to clear and intuitive concepts and ideas. During my senior years, Prof. Howard gave me so much freedom and trust that I could try and test my own ideas. Especially when I get stuck and feel frustrated in this project, he always encourages me and gives full support to help me continue.

I also want to thank two other readers in my dissertation committee, Professor John Pauly and Dr. Ivan Linscott, for providing valuable feedback and suggestions.

I feel extremely honored to be part of Stanford Remote Sensing Group and thank all the group members with whom I have shared lots of fun. As a junior member, I deeply appreciate all their help in processing and analysis the dataset and their valuable research suggestions on this project. Also, they create a warm and fun group environment, making me feel at home. I will always remember all the stimulating discussions, the sleepless nights we worked together and all the fun we had in the past few years. The list includes Albert Chen, Cody Wortham, Jessica Reeves, Jingyi Chen, Jamie Lien, Tao Chu, Liu Lin,Will Woods, Clara Yoon, Ryan Smith and Yujie Zheng.

I want to thank Stanford Graduate Student Office, Stanford Electrical Engineering Department staff and Vaden Health Center, especailly my therapist Valaiporn Rusmintratip for providing constant care and help during my struggle with depression.

Last but not least, I want to thank my parents and sister for supporting me throughout my Ph.D and life in general. They selflessly encourage me to explore on my own and never settle until I find things I sincerely love. Without their sacrifice, the journey would not be possible.

Contents

List of Tables

List of Figures

List of Acrynoms

2-D	two dimentional
3-D	three dimentional
ALOS	Advanced Land and Ocean Sensor
CAT	Computed Axial Tomography
CDF	cumulative distribution functions
DEM	Digital Elevation Model
DFT	Discrete Fourier Transform
DInSAR	Differential SAR Interferometry
DS	distributed scatter
EM	Electromagnetic
FT	Fourier transform
Gt C	gigatonnes
InSAR	SAR interferometry
JAXA	Japan Aerpspace Exploration Agency
MLE	Maximum Likelihood Estimation

MVB	Advanced Land and Ocean Sensor
pdf	probability density function
PolIn	Polarimetric Interferometry
ppmv	parts per million volume
PRF	Pulse Repetition Frequency
PS	Persistant Scatter
PSF	Point Spread Function
RVoG	random volume over ground
SAR	Synthetic Aperture Radar
SLC	Single Look Complex
SNR	Signal to Noise Ratio
SOI	signal of interest
SRTM	Shuttle Radar Topography Mission
TEC	total electron content
TomoSAR	SAR tomography

Chapter 1

Introduction

1.1 Motivation for Mapping Global Forest Biomass

1.1.1 Climate Change & Global Carbon Cycle

Climate change is a global-scale problem that has major impacts on human and natural ecosystems. Earth's climate has operated for millennia within a balance between the atmosphere, ocean and terrestrial systems. However, recent years see increasing temperatures in many regions, and also increasing number and extremities of weather patterns, including severe heat waves, hurricanes,droughts and wildfires [Karl and Trenberth (2003); Justus and Fletcher (2001)]. Global climate change is thus widely recognized as the greatest threat facing the planet, a fundamental challenge to global prosperity. Most climate scientists agree that the main cause of the current global warming trend is the human expansion of the greenhouse effect, in which heat generated from sunlight at the Earth's surface is trapped by greenhouse gasses and prevented from escaping through atmosphere. Among the greenhouse gases, carbon dioxide (CO_2) is the most significant one. In addition to the natural fluxes of carbon through the Earth system, human activities, particularly fossil fuel burning and deforestation, have released billions of tons of carbon dioxide into the atmosphere, thus pushing the global carbon cycle out of balance.

Figure 1.1 covers hundreds of thousands of years and provides the evidence that atmospheric CO_2 level is closely related to the global temperature. The figure also shows the

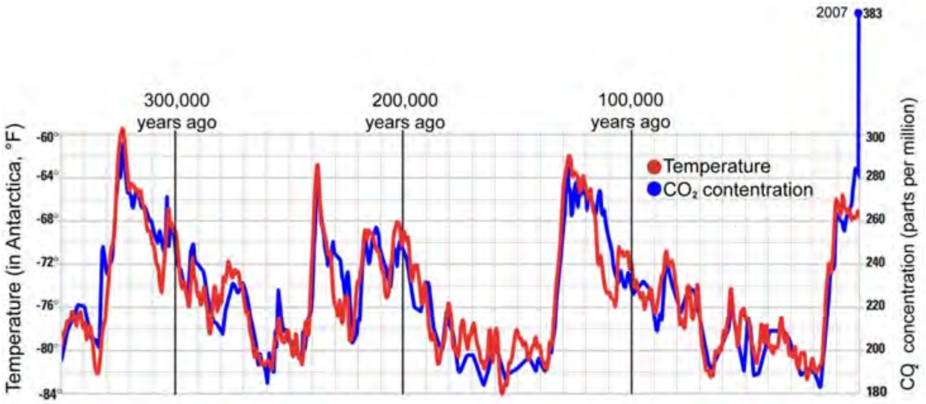

Figure 1.1: Atmospheric carbon dioxide concentration over years (Credit: Vostok ice core data/J.R. Petit et al.; NOAA Mauna Loa CO_2 record).

atmospheric CO_2 concentration has dramatically increased since the Industrial Revolution. Over the 400,000 years prior to Industrial Revolution, the atmospheric concentration of CO_2 only varied between ˜80 ppmv (parts per million volume) and ˜180 ppmv, which is remarkably narrow. In contrast, atmospheric CO_2 concentration has risen to ˜ 370 ppmv, approximately 35% above the natural background level, and has risen to that level at a rate at least 10 and possibly 100 times faster than at any other time in the past 400,000 years [Falkowski et al. (2000)]. To understand the overall effect of the increased carbon emission, it is necessary to examine the whole perspective. In the big picture, atmospheric carbon dioxide is part of the complex global carbon cycle, as showed in Figure 1.2.

Although much of the modern increase in the atmospheric carbon pool results from human activities, the future trajectory of the atmosphere also depends on the response of terrestrial and ocean systems to the changing climate [Tollefson (2009)]. Natural fluxes of carbon in and out of terrestrial and ocean reservoirs are an order of magnitude larger than the perturbation from fossil fuels and land use change (IPCC 2007), as shown in Figure 1.3.

Accordingly, for better understanding the climate change and designing mitigation policies, both the amount of CO_2 humans continue to release and the future carbon uptake and storage by land and ocean are needed. In short, a quantitative global carbon cycle model is required.

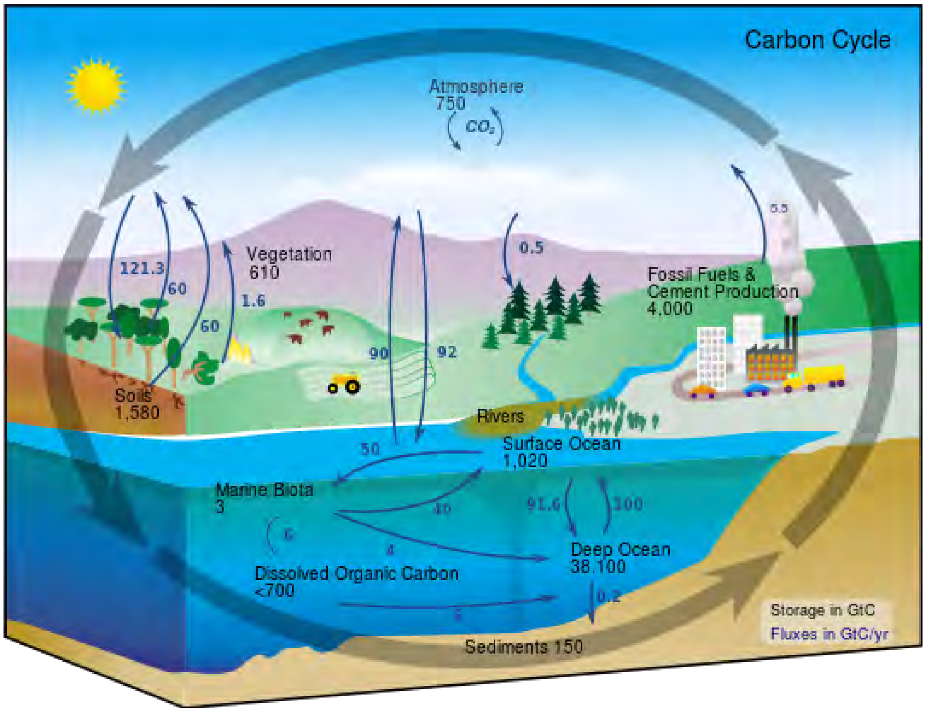

Figure 1.2: The global carbon cycle shows how carbon atoms flow between various reservoirs in the Earth system.

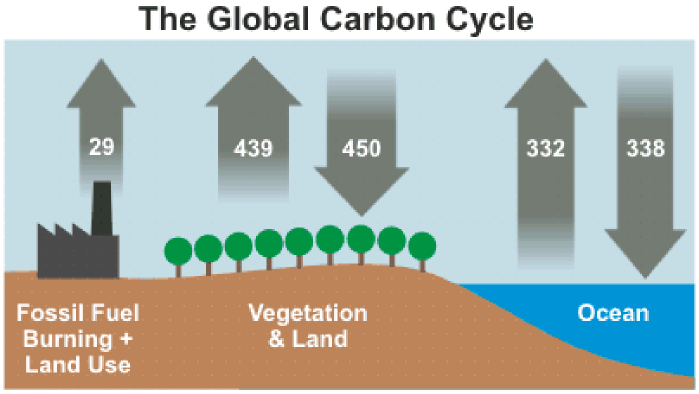

Figure 1.3: The human CO_2 emission compared to the natural CO_2 emission. Numbers represent flux of carbon dioxide in gigatonnes. (Source : IPCC AR4)

1.1.2 Significance of Forests in Global Carbon Cycle

One of the greatest uncertainties affecting the global carbon budget arises from the lack of information on forests. Forests cover approximately 38.5 million km^2, 28% of the land surface, and contain 77% of the terrestrial above ground carbon [Pan et al. (2011)]. In basic terms, forests are made up of trees and woody plants. The mass of trees is often referred as “biomass”, meaning “living mass ,” and is composed of nearly half of carbon when water is discounted. The total forest carbon stock is estimated at 861 Gt C (gigatonnes of carbon, 1 GtC = 10^9 tonnes C = 3.67 Gt CO_2), which is 1.5 times more than the total anthropocentric carbon emission since Industrial Revolution. Of the total forest carbon stock, 363 Gt C are held in living biomass, 116 Gt C are in litter and dead wood, and 383 Gt C are stored in the soil [Pan et al. (2011)].

Forests play a key role in the global carbon cycle, continuously cycling carbon via photosynthesis, growth, respiration, death and decay. Terrestrial vegetation alone cycles over 120 Gt of carbon each year, taking up approximately 123 Gt C and respiring 119 Gt C [Quéré et al. (2013); Figure 1.3]. This is about 15 times more than the total anthropogenic emission from burning fossil fuels and producing cement each year (˜8 Gt C). On land, these fluxes are dominated by forests. The significance of forests in the global carbon cycle is demonstrated by seasonal variation (variation within a year) of atmospheric CO_2 concentration. The visible sawtooth effect in Figure 1.4 shows that the atmospheric carbon concentration corresponds to the growing season in the northern hemisphere, where most forests exist [Graven et al. (2013)].

Forests have also played, and continue to play, a huge role in slowing the rate of climate change thus far. Mature and regrowing forests have been sequestering over 4 Gt of carbon each year since the 1990s. Thus, because of forests, the atmospheric concentration of CO_2 are not rising as rapidly as would be by simply adding all the anthropogenic emission to the current level in the atmosphere. This phenomenon has been called a ‘loan from nature’ and a ‘buffer to climate change’[Phillips and Lewis (2014)].

Besides its role in global carbon cycle, forest biomass is also profoundly important as a source of energy and material for human use. It is a major energy source in subsistence economies, contributing around 9–13% of the global supply of energy [Haberl and Erb

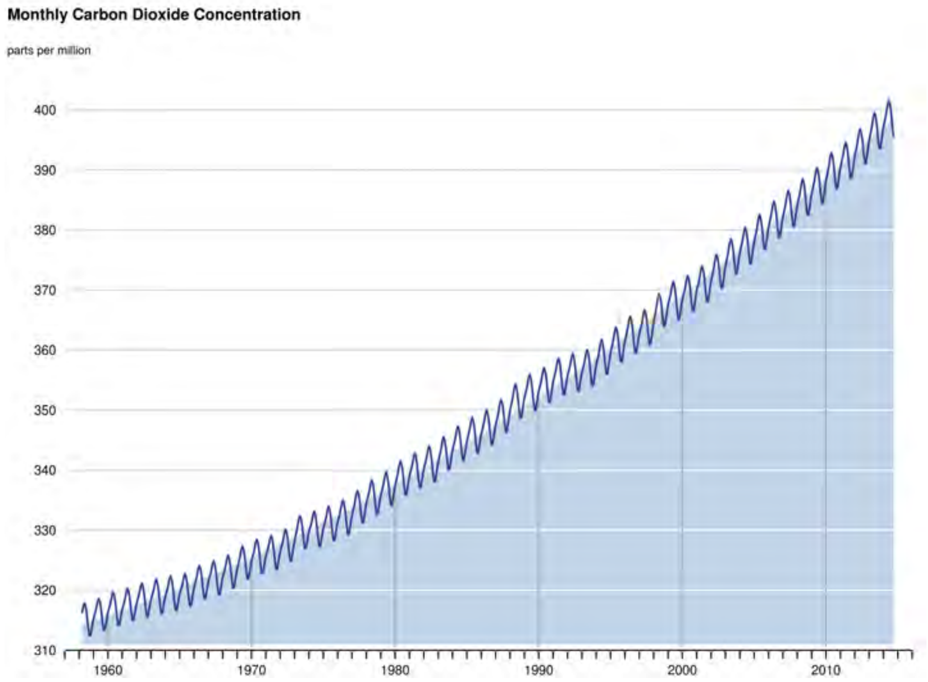

Figure 1.4: Monthly carbon dioxide concentration. Sawtooth effect in atmospheric carbon dioxide is caused by seasonal change in northen hemisphere terrestrial forests growth.

(2006)]. Biomass and biomass change also act as indicators of other ecosystem services. Field studies have shown how large-scale and rapid changes in the dynamics and biomass of tropical forests lead to forest fragmentation and the increasing vulnerability of plants and animals to fires [Malhi and Phillips (2004)]. Current research also shows that above-ground biomass is strongly related to biodiversity [Bunker et al. (2005)]. Regional to global information on human impacts on biodiversity therefore requires accurate determination of forest structure and forest degradation, especially in areas of fragmented forest cover. This is also fundamental for ecological conservation. The provision of regular, consistent, high-resolution mapping of biomass and its changes would be a major step towards meeting this information need.

As a result, forest biomass is defined by the United Nations Framework Convention on Climate Change (UNFCCC) as an essential climate variable needed to be reduce uncertainties in our knowledge of the climate system. Further strong need to improve methods for measuring global biomass comes from the Reduction of Emissions due to Deforestation and Forest Degradation (REDD) mechanism,which was introduced in the UNFCCC Committee of the Parties (COP-13) Bali Action Plan. Its implementation relies fundamentally on developing systems to monitor carbon emissions due to loss of biomass from deforestation and forest degradation. Lack of information on forest biomass has become one of the greatest uncertainties concerning the global carbon budge.

All these statements highlight an urgent need for global forest biomass mapping based on an accurate, timely, cost-effect method. However, despite the obvious need, currently there is no existing global observation program for forest biomass.

1.1.3 Relating Forest Biomass to Forest Vertical Structure

Forest biomass is related to several parameters, including the tree height, diameter and crown width, as shown in Figure 1.5. In forestry, the biomass calculation is based on measurements of trunk diameter and height of the sample population of trees [Whittaker et al. (1974)] as

$$Biomass_{forest} = N \cdot \pi \cdot (1/2dbh_{mid})^2 \cdot h_{mid} \cdot \rho \cdot f_z, \tag{1.1}$$

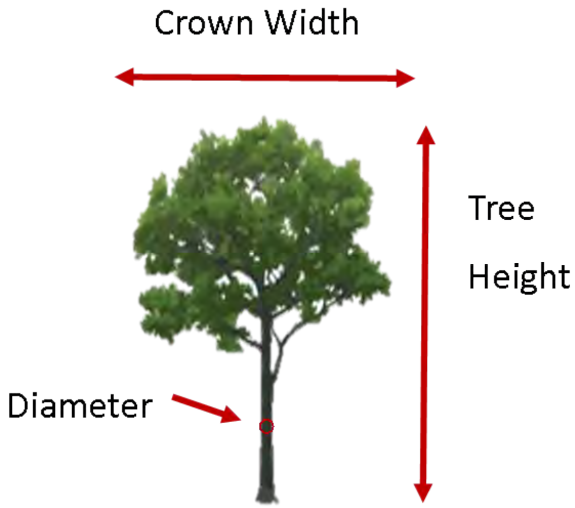

Figure 1.5: Forest biomass is related with trunk diameter, height of the tree and crown width.

where $Biomnass_{forest}$ is defined as above ground woody of trunk and branches which exceed $7cm$ diameter, $dbh_{mid}[cm]$ is the mean diameter at the breast height 1.3 m, $h_{mid}[m]$ is the height of dbh_{mid} tree, $\rho[g/cm^3]$ is the species-specific wood density, f_z is a form factor (roughly $0.4-0.5$), and N is the tree density (tree number per area unit). The product of $N \cdot \pi \cdot (1/2dbh_{mid})^2$ is also called basal area g .

Usually, forest biomass can be directly related to the tree height by a power law

$$Biomass_{forest} = a \cdot height^c, \tag{1.2}$$

where a and c depend on forest species and other natural conditions [Woodhouse (2006)]. Equations of this form have been developed for trees in different forest zones, with c ranging from 0 to 4. A special case exists for values c near 0, which means the height of the trees no longer indicate forest biomass density. This is due to that for certain forest types, the increase in tree biomass is balanced out by a rapid reduction in number tree density so that over a stand evolution there is no change of biomass (and eventually a reduction) with the increasing tree height. Using the allometric equation to derive biomass presents the importance of measuring the forest height. However, in practice, the height-biomass allometry has been of little use up to now, because height measurements are far more difficult than measurements of the tree diameter, the tree density or the basal area.

With advancing remote sensing technology, especially the rapid development of synthetic aperture radar, measuring forest vertical structure can be achieved in a global, continuous and low-cost way.

1.2 Spaceborne Synthetic Aperture Radar

The most promising tool for forest biomass monitoring is spaceborne synthetic aperture radar (SAR). SAR systems operating with long (decimetric or metric) radio wavelength possess the capability of penetrating deep into forest volume, making them an ideal sensor for forest investigations [Woodhouse (2006); Le Toan et al. (1992)]. In addition, spaceborne SAR has unique imaging capability. Compared to other sensors, it can provide global coverage, long time regular acquisition and high resolution. Thus, SAR becomes a key tool for environmental monitoring in the modern changing and dynamic world [Curlander and McDonough (1991); Oliver and Quegan (2004); Soumekh (1999)]. Since the launch of the first SAR satellite, Seasat, in 1978 [Tapley et al. (1982)], huge development has been achieved in technology, techniques and information retrieval algorithms. Currently, more than 15 Spaceborne SAR sensors are operating and within the next 5-6 years, 10 new SAR systems will be launched [Moreira (2014)]. A summary of state of the art of spaceborne SAR systems is provided in Table 1.1.

The following Figure 1.6 also shows the life spans of several recent and future SAR missions. The solid lines indicate past operational service periods and the dashed lines indicate expected future operational service periods.

We have entered a golden age for spaceborne SAR remote sensing. Not only will more SAR images be available, but also more diverse information be enabled by the polarimetric operation, multiple frequencies, improved range and azimuth resolutions and the observation angle diversity. Thanks to the recent advances of space technology, the number of images of the same scene is expected to significantly grow in the future. Even with existing satellites, archives are filled by datasets acquired at different times and with varying

Sensor	Operation	Band (Polaris)	Industry/ Country
TerraSAR-X	2007-today	X(quad)	DLR/Astrium , Germany
TanDEM-X	2007-today	X(quad)	DLR/Astrium , Germany
Radarsat-2	2007 – today	C(quad)	CSA, Canada
COSMO-SkyMed-1/4	2007 … 2010 – today	X(dual)	ASI, MiD
HJ-1C	2012 –today	S(VV)	CRESDA/CAST , NRSCC, China
Sentinel-1a/1b	2014– today	C (dual)	ESA, Europe
ALOS–2	2014 – today	L (quad)	JAXA, Japan
SAOCOM – 1/2	scheduled.: 2014/2015	L (quad)	CONAE, Argentina
Radarsat Constellation	scheduled.: 2017	C(quad)	CSA, Canada

Table 1.1: Selected Current and Future Spaceborne SAR System.

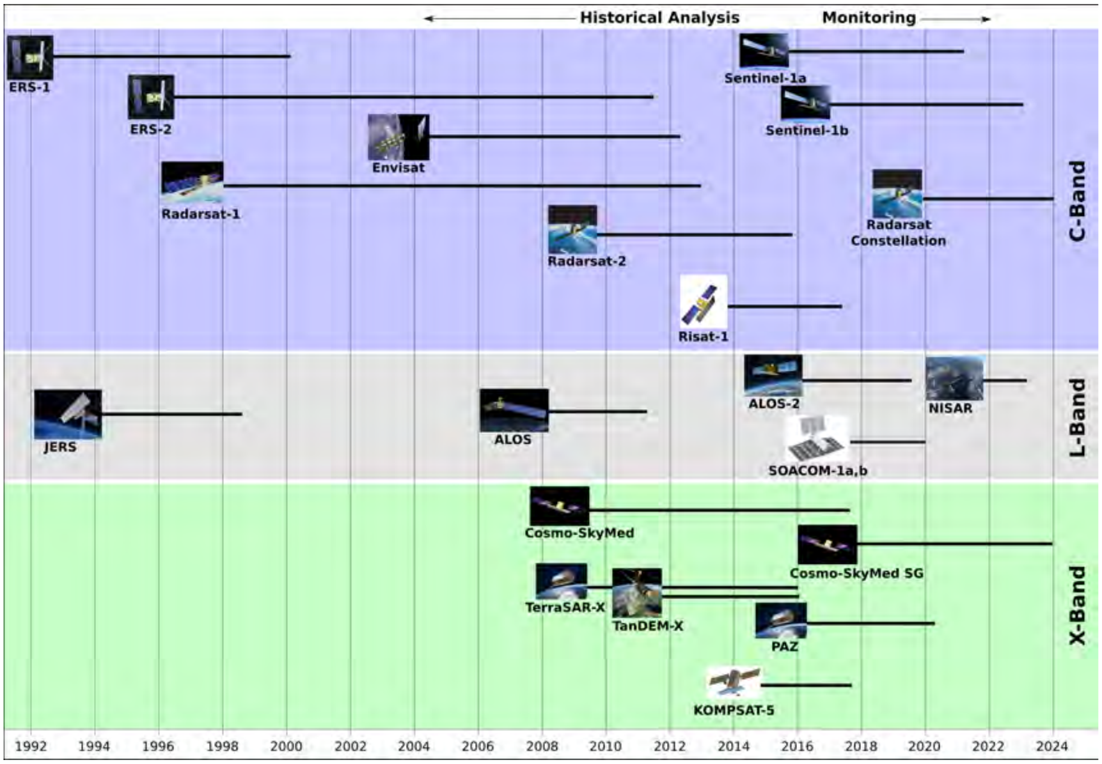

Figure 1.6: Life spans of recent SAR missions.The solid lines indicate past operational service periods and the dashed lines indicate expected future operational service periods. (By courtesy of Lin Liu)

imaging geometries over the same scene. For these reasons, current research is pushed toward the development of innovative processing techniques, aimed at extracting all valuable information lying in the current and future available datasets to produce new and more accurate physical measures [Moreira (2013)].

Within this context, we propose a new algorithm for solving the old problem, retrieving forest biomass density from the wealth of past and future L-band SAR data. Through this, we try to provide valuale insights for future research.

1.3 Literature Review on Measuring Forest Biomass using SAR Images

Deriving forest biomass from synthetic aperture radar data has been of great interest in the SAR community for decades. At the beginning, a number of experiments from synthetic aperture radar sensors have demonstrated that the radar backscatter is often statistically correlated with the forest above-ground biomass [Le Toan et al. (1992); Haberl and Erb (2006); Beaudoin et al. (1994)]. However, this is limited by the issue of saturation [Imhoff (1993, 1995)], where the increasing biomass does not increase the backscatter intensity proportionately at high biomass levels. Techniques in SAR interferometry can also provide estimates of carbon stocks through measurements of the forest height and vertical structure. The topographic sensitivity of an interferometer can be used to retrieve the tree height, but the knowledge of the true ground surface and canopy penetration characteristics must also be available [Kellndorfer et al. (2004); Walker et al. (2007); Simard et al. (2006)].

In the previous decade, another promising SAR technique using a single baseline fully polarimetric data, called Polarimetric SAR Interferometry (PolIn SAR) has been widely exploited to invert the forest height through model-based inversions [Cloude and Papathanassiou (1998, 2003); Papathanassiou and Cloude (2001); Mette et al. (2003)]. It is based on the fact that volume interferometric coherence is directly related to the vertical distribution of scatters seen by radar at the given frequency and polarization. The volume coherence is given by the Fourier transform of the vertical distribution of the scatters. The estimation of the vertical forest structure function in terms of PolIn SAR measurement is then performed using model based inversion. PolIn SAR utilizes a random volume over ground (RVoG) model, which relates the interferometric coherence to a set of forest parameters, such as ground and canopy elevation, ground to volume amplitude ratio. It requires a solution of a non-linear optimization problem.This technique suffers several drawbacks. First, it cannot separate targets which exhibit the same scattering mechanism. Second, the complicated model inversion involves too many input parameters depending on the specific forest type and situation. Also this model requires the forest to stay the same during the repeat visit period, equivalent to temporal decorrelation close to 1.

In contrast, in this thesis, SAR tomography we propose is a nonparametric and model free methodology. By exploiting multiple SAR images to synthesize an aperture in the elevation direction, this methodology requires few assumptions, is easy to implement and is rather robust to noise.

1.4 Thesis Contribution

The thesis is a first attempt to utilize the available spaceborne repeat pass SAR images to reconstruct the forest vertical structure. In this study, we use data from the Advanced Land Observing Satellite (ALOS), launched by the Japan Aerospace Exploration Agency (JAXA) in 2006. It carried an instrument called phased array type L-band synthetic aperture radar (PALSAR), which acquired the data used here. Our study is carried on in the Harvard Forest, Massachusetts. Located near the Quabbin reservoir in Western Massachusetts, Harvard Forest is a temperate zone mixed phase forest consisting of a variety of transition hardwood regrowth. As one of the nine NASA funded Bigfoot sites for connecting remote sensing measurements to ground process observations of carbon flux and net primary production, Harvard Forest has been a resource for a wide variety of ecological studies. The results from our study could further contribute to other research in this ecosystem.

The main contributions in this thesis are as follows:

- We develop the scheme of spaceborne SAR tomography and propose to use adaptive beamforming to retrieve the forest vertical structure. Special focus is taken on analyzing different limitations of spaceborne repeat-pass SAR datasets and their effects on the reconstruction results.

- We develop a new spatially adaptive speckle filter to reduce the effect of distributed scatterers in forests.
- We analyze various phase errors and their impacts on SAR tomography results, and then propose a robust Capon beamforming method to mitigate the phase errors.
- We investigate the temporal decorrelation in real SAR data and analyze its effect in SAR tomography.
- We implement the algorithm pipeline on real ALOS SAR datasets and discuss the performance on both urban and forest regions.

1.5 Outline of Thesis

The remainder of this thesis is organized as follows: After the introduction, Chapter 2 introduces the basic principles of SAR and SAR interferometry as the first attempt to recover the elevation information. Chapter 3 begins with the theoretical basis of SAR tomography. Detailed analysis of the SAR tomography framework shows that the technique finally leads to a spectral estimation problem. Afterward, the Capon beamformer is proposed and tested as our reconstruction method. Based on the theory explained in Chapter 3, Chapters 4, 5 and 6 discuss the specific limitations when the technology is applied in the forest areas. The limitations, listed as distributed scattering properties, phase errors and temporal decorrelation, are analyzed in detail in each chapter.

In Chapter 7, we test the proposed algorithm on real SAR datasets. We select the Golden Gate Bridge in the San Francisco Bay Area as an example for the urban area, showing the reconstructed tomographic profile through 8 SAR images. For the forest area, we choose a scene near the Harvard Forest as an example, reconstructing the forest vertical profile and estimating the forest height.

Finally in Chapter 8, we summarize our conclusions and contributions, and also lay out suggestions for future research.

Chapter 2

Synthetic Aperture Radar Basics

2.1 Introduction

Radar, an acronym for radio detection and ranging, is an active microwave remote sensor. It was first developed during World War II with the purpose of detecting targets. Radar uses the same antenna to send and receive electromagnetic (EM) pulses. Since EM pulses propagate at the speed of light, the distance to the target is proportional to the time it takes between the transmission and reception of the radar echoes. Thus, by analyzing the received echoes, radar is able to detect and locate targets. After World War II, radar experienced rapid growth with numerous applications in environmental remote sensing. The most commonly used radar sensor is the synthetic aperture radar (referred to as SAR). Compared to other optical sensors operating in the visible or infrared bands, SAR has a few distinct advantages:

- SAR is an active sensor providing its own illumination, and hence can operate day and night.
- SAR uses longer wavelength microwaves which can penetrate through cloud cover, haze, dust and heavy rainfall. This property allows it to work in almost all weather and environmental conditions.
- SAR can partially penetrate arid and hyper-arid surfaces, revealing subsurface features of the Earth.

- SAR uses polarized radiation, and therefore can exploit the polarization signature of imaged scatters for obtaining additional information about the structure of the scatter.
- SAR is a coherent imaging method, which enables interferometric applications.

For these reasons, SAR is widely used to generate high resolution images of the Earth surface, especially areas where it is not practical or safe to inspect directly. Since its development in 1960s, SAR has been a valuable tool for a wide variety of applications, including ice and snow monitoring, oil pollution monitoring, oceanography and classification of terrain, providing vital geophysical information for environmental research.

This chapter attempts to explain basic principles of the SAR imaging system. In the first part, we introduce the general principles of SAR, highlighting some specifics of the imaging system. In the second part, we briefly introduce the theory of the SAR interferometry and differential SAR interferometry. Finally, we discuss the phase noise in SAR interferometry and the concept of coherence as the common measurement for the phase noise.

2.2 Geometry of the SAR Imaging System

Synthetic aperture radar is a particular implementation of the imaging radar system, which utilizes the flight path of the platform to synthesize an extremely large antenna in order to generate high resolution remote sensing images. In the standard monostatic architecture, the SAR system is composed of a moving platform with the same antenna as the transmitter and receiver. There are basically three operating modes for the SAR imaging system: strip-map, scan and spot. The most popular one is the strip-map mode. A typical space-based, strip-map, monostatic SAR system is sketched in Figure 2.1.

In this figure, a radar sensor is mounted on a moving platform, typically a satellite or an aircraft. The direction the platform moves is called azimuth or along-track direction, referred to as x, whereas the direction perpendicular to the azimuth is called slant range or cross-track, referred to as r. The swath gives the area illuminated by the antenna. Within the illuminated area, the radar sensor transmits electromagnetic pulses with high power and receives the backscattered echoes from the ground. The pulse transmitted from the antenna

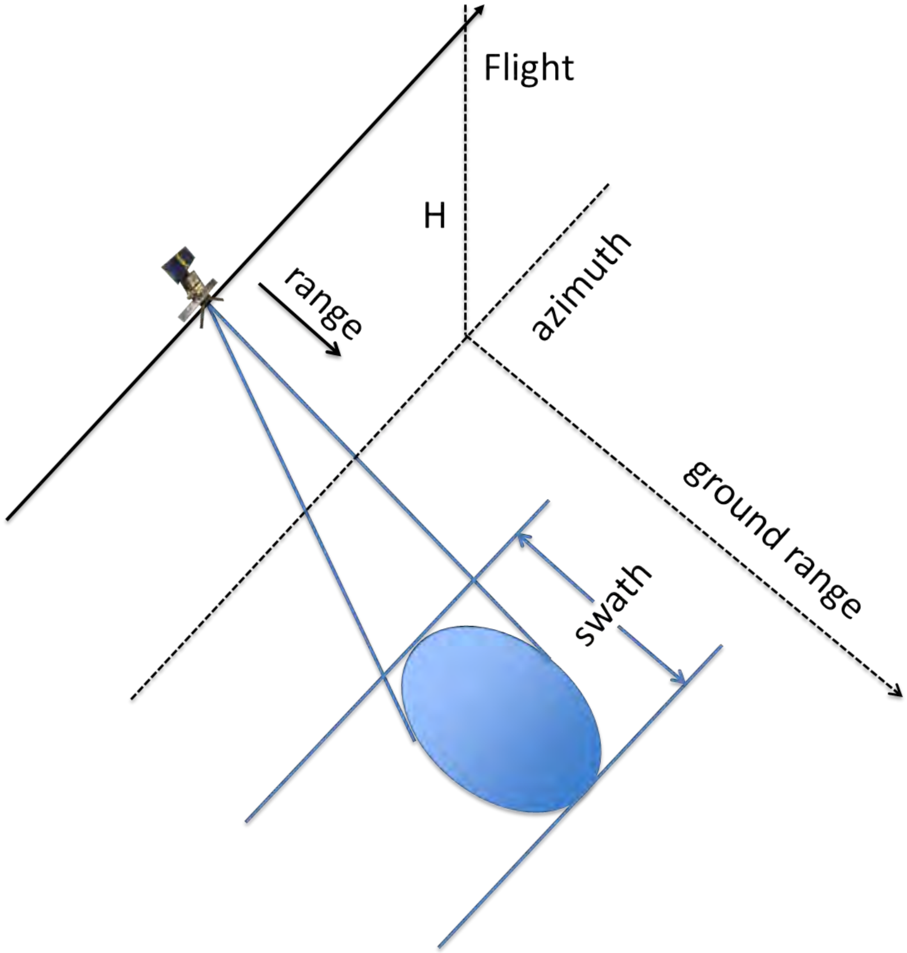

Figure 2.1: Geometry of side-looking strip-map SAR

has a duration τ_p and is repeated at a given frequency, called pulse repetition frequency (PRF). The typical PRF ranges from a few hundred to a few thousand Hertz. The radar operation is coherent, which means that both the return magnitude and phase (with respect to the transmitted signal) are sampled. For each sample, the in-phase and quadrature values (I and Q) are stored. The raw data file is thus an array of complex values. To form an image, the raw data are assembled line by line in a data matrix, usually with the column associated with the range direction and the row with the azimuth direction. In this way, a SAR image is generated with each pixel representing the received echoes from the corresponding illuminated area.

2.3 Resolution of Real Aperture Radar

One of the most important characteristics of the imaging radar system is the resolution. Resolution is defined as the ability of the system to distinguish between two closely spaced targets. Higher resolution in a radar system means that more detailed information can be measured.

2.3.1 Range Resolution

First, consider the resolution in the slant range direction. Suppose two point targets are separated by a distance d_r in the slant range direction. Since the radar waves propagate at the speed of light, the corresponding echoes will be separated by a time difference Δt as:

$$\Delta t = 2 d_r / c, \tag{2.1}$$

where c is the speed of light and the factor 2 is due to the round-trip propagation. If the radar echoes from two targets are separated longer than the pulse length, it is possible to recognize the echoes as from different targets. Thus, the smallest time difference in the radar receiver should be equal to the effective time length of the pulse, τ_p. We can derive the range resolution as:

$$\rho_r = \frac{c\tau_p}{2}. \tag{2.2}$$

It can also be expressed in terms of the pulse bandwidth W as:

$$\rho_r = \frac{c}{2W}. \tag{2.3}$$

From the above equation, it is obvious that by using very short pluses, the range resolution for a given radar can be significantly improved. Unfortunately, using short pulses decreases the average transmitted power. Since the average transmitted power is directly linked to the receiver signal to noise ratio (SNR), it is often desirable to increase the pulse width while simultaneously maintaining adequate range resolution. This can be made possible by using the pulse compression technique.

Pulse compression allows us to achieve a higher transmitted power, while obtaining the range resolution corresponding to a short pulse [Curlander and McDonough (1991), Chapter 3]. The most popular waveform used in range compression is called a chirp (a linear frequency modulation of the narrow band signal). It can be written as:

$$p(t) = cos(2\pi f_c t + \pi K_r t^2) rect\left[\frac{t}{\tau}\right], \tag{2.4}$$

where f_c is the carrier frequency, K_r is the frequency modulation rate, τ is duration, and *rect* is the rectangular function. A portion of the chirp for the ERS radar as well as its power spectrum and impulse response is shown below.

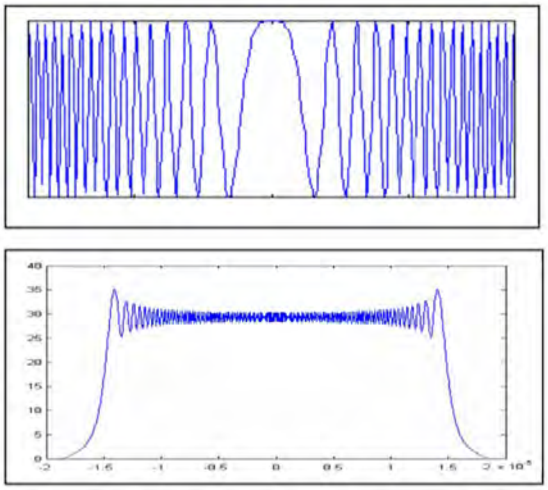

Figure 2.2: A chirp signal in time and frequency domain.

The bandwidth of a chirp signal is

$$W = K_r \tau. \tag{2.5}$$

Now the bandwidth can be increased with an increase of the pulse duration. Since the chirp signal is a phase modulation, a demodulation step is required to retrieve the actual information. This can be accomplished with a matched filter for the chirp. Pulse compression techniques are routinely used for both the generation and the matched filtering of radar waveforms.

2.3.2 Azimuth Resolution

Regarding the azimuth resolution, a single point scatterer will contribute to the raw data matrix as long as it is within the antenna footprint. Hence, the azimuth resolution of a side-looking real aperture radar is determined by azimuth footprint, which, from antenna theory, is inversely proportional to the physical shape and dimension of the antenna [Silver (1949)]. Considering an X-band ($\lambda = 0.03m$) system with an antenna length $L = 3m$ and assuming the range distance, which is the distance from the antenna to the target , r_0 to be 800 km, this yields to the azimuth resolution as:

$$\rho_a = \frac{\lambda}{L} R_0 = \frac{0.03}{3} 800\,km = 8\,km. \tag{2.6}$$

From Equation 2.6, we can see that the azimuth resolution is too coarse for most applications. For an acceptable resolution of the order of a few meters, either the antenna size or the frequency must be increased. However, the frequency is fixed and the unrealistically large antennas like several kilometers cannot be made for structural engineering reasons.

2.4 Synthesizing a Larger Aperture

The synthetic aperture concept was invented to overcome limitations in the azimuth resolution. SAR technology is able to achieve a much higher resolution while using a small antenna. Carl Wiley of Goodyear Aerospace was the first to improve the azimuth resolution through Doppler frequency analysis of signals collected from a moving radar [Wiley (1965); Willey (1985)]. As the radar moves, two targets at different azimuth positions will be at different angles relative to the radar velocity, resulting in different Doppler frequencies. Thus, it is possible to use the Doppler frequency to separate them. In following years, this technique is extended to the principle of the synthetic aperture.

The basic concept of aperture synthesis is that a point is illuminated not just with one single pulse but with a sequence of pulses while the platform is moving. Figure 2.3 illustrates how this is achieved. Once the point first enters the radar beam, the backscattered echoes from each transmitted pulse begin to be recorded. As the platform continues to move forward, echoes from the point for each pulse are recorded during the entire time that the point is within the beam. The flight path where the target is within the view of the radar beam determines the length of the simulated or synthesized antenna length.

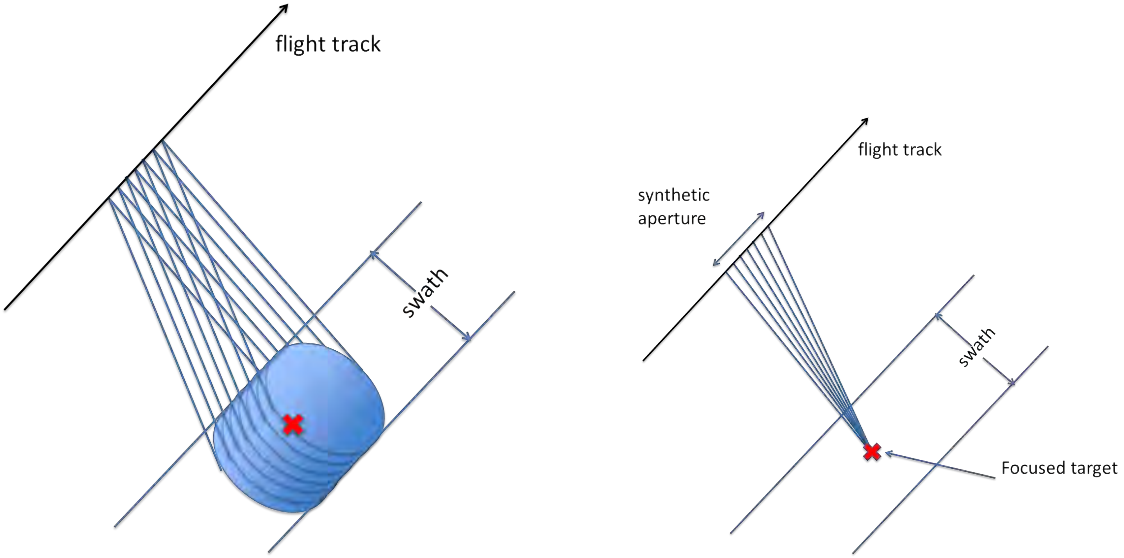

(a) continuously illuminating the target along the path

(b) combining all the echoes and synthesizing a long antenna

Figure 2.3: Graphic illustration of the synthetic aperture principle. All along its path, the radar acquires a series of images that are combined by post processing. The final image looks like an image acquired by an antenna that is the sum of all the basic antennas.

The brief derivation of the azimuth signal property is as follows. As the radar moves, the distance between the radar and the scatterers also changes. Since the signal phase is given by $-4\pi R(s)/\lambda$, the changing distance means the phase of the signal will be different for the different position along the flight path.

Suppose a scatterer initially at distance R_0, as the radar sensor moves at velocity of v , at time s. The distance between the radar sensor and the scatter can be written as:

$$R(s) = \sqrt{R_0^2 + v^2 s^2}. \tag{2.7}$$

For most remote sensing radars, we have $vs \ll R_0$. In this case, we can approximate the range as a function of time as:

$$R(s) \approx R_0 + \frac{v^2 s^2}{2R_0}. \tag{2.8}$$

Then the phase of the signal is

$$\phi(s) = -\frac{4\pi R(s)}{\lambda} \approx -\frac{4\pi R_0}{\lambda} - \frac{2\pi v^2}{R_0\lambda}s^2. \tag{2.9}$$

The instantaneous frequency of the signal becomes

$$f(s) = \frac{1}{2\pi}\frac{\partial\phi(s)}{\partial s} = -\frac{2v^2}{R_0\lambda}s. \tag{2.10}$$

Equation 2.10 shows that the signal in the azimuth direction is also a linear frequency chirp. Hence, as in the range direction, we can also apply a matched filter to obtain fine resolution. To find the bandwidth of the signal, we have to find the time that the scatterer is illuminated by the antenna. For an antenna with a physical length L, the scatterer illuminated time is given by

$$t_{total} = \frac{\lambda R_0}{Lv}. \tag{2.11}$$

In this case, the obtained resolution of the synthesized array is

$$\rho_a = \frac{v}{B_D} = \frac{v}{f(s)t_{total}} = \frac{L}{2}. \tag{2.12}$$

Equation 2.12 gives a very important result, indicating that the azimuth resolution does not depend on the range distance, but only depends on the antenna size. The resolution improves when the effective dimension of the antenna L is reduced. This seems contradict to the real aperture case, however, this is essentially because a smaller antenna has a wider lobe, and a target will be seen for a longer time. As the result, the synthesized array is larger and equivalent beam-width is sharper. Through aperture synthesis, SAR can achieve high resolution with a small antenna.

2.5 Understanding Single-Look Complex SAR images

Since radar interacts with the ground features in ways different from optical radiation, special care has to be taken when interpreting radar images. In order to interpret remote sensing SAR images, it is necessary to understand their particular properties in detail.

First, the raw SAR data have to be compressed in the range and azimuth directions through some SAR processors. In this study, we use the SAR processor described in [Zebker et al. (2010)]. The focused SAR image is called a single look complex (SLC) image and can be seen as a two dimensional array of complex valued pixels. Typically, rows are associated with different azimuth locations while columns with different slant range locations. Each pixel is the coherent sum of microwave field back scattered by all the scatters (rocks, sands, vegetation, buildings, etc.) within corresponding resolution cells projected on the Earth surface. Also, each pixel gives a complex number, in which the amplitude is determined by the backscattered energy and the phase is determined by the slant range distance from the pixel location to the radar sensor. The location and dimension of the resolution cell in azimuth and slant-range coordinates depend on SAR system characteristics.

A single radar image is usually displayed as a gray scale image, in which the intensity of each pixel represents the proportion of microwave energy backscattered from the area on the ground, often called the reflectivity or radar cross section. The reflectivity depends on a variety of factors: types, sizes, shapes and orientations of the scatterer. As a rule of thumb, the higher the backscattered intensity, the rougher is the surface being imaged. Flat surfaces such as calm water and paved roads normally appear to be dark since most of the incident radar pulses are reflected away. Trees and other vegetation areas are usually moderately rough on the wavelength scale. Hence, they appear moderately bright in the image. Very bright targets, such as built-up and man-made features, may appear in the image due to the corner-reflector or the double bounce effect where the radar pulse bounces off the horizontal ground toward the targets and is then reflected from one vertical surface of the target back to the sensor. A typical value of radar cross section for different scatter types is listed in Figure 2.4.

A typical SLC SAR image is showed in Figure 2.5. This is a SAR image of the San Francisco area, taken by Japanese ALOS satellite on March 25, 2011(for detailed information about ALOS, see Chapter 7). The figure agrees with the theory: the Pacific Ocean, belonging to flat surfaces, appears the darkest while downtown San Francisco and Oakland, dominated by corner reflectors, appear to be brightest.

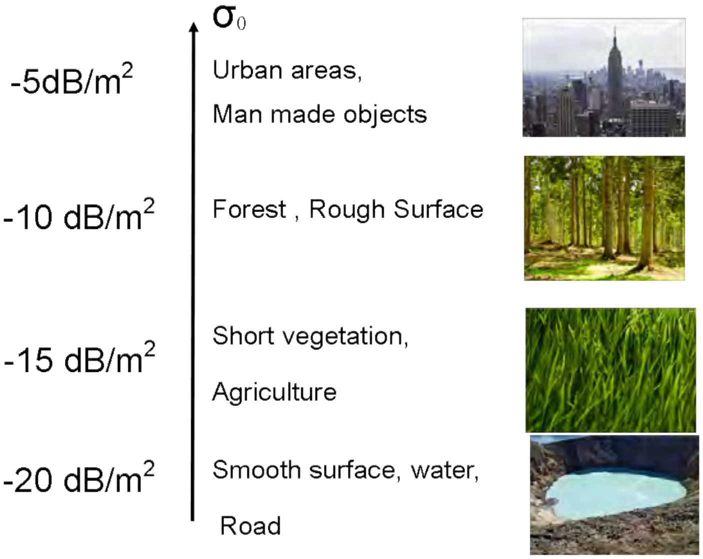

Figure 2.4: Typical radar cross section for different targets

2.6 SAR Interferometry

SAR interferometry (InSAR) is the first powerful and well-established technique for extracting three-dimensional information of the Earth surface through the phase differences between two complex radar signals. Significant applications for providing important geophysical parameters with high accuracy using InSAR are digital elevation model (DEM) generation, geophysical hazard analysis, glacier velocity measurement, and land use classification. The interferogram is generated by combining two complex-valued SAR images of the same scene, acquired at two different but similar look angles. The two SAR images can be acquired simultaneously (with two radars mounted on the same platform) or at different times by exploiting repeated orbits of the same satellite. In most of spaceborne SAR systems, the interferometry is achieved through repeat passes.

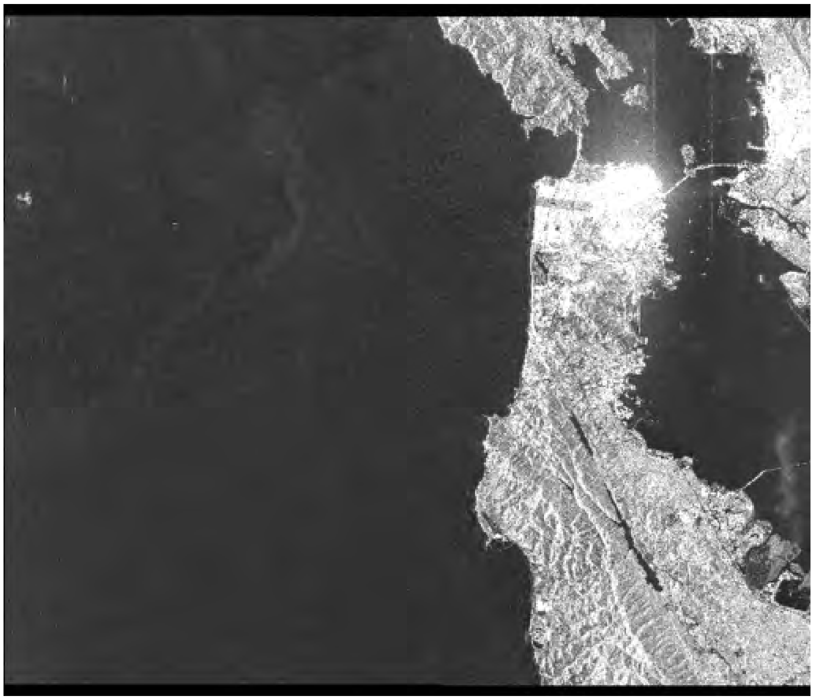

Figure 2.5: A sample SAR image of San Francisco, taken by ALOS on MAR 25, 2011. San Francisco and Oakland urban areas, dominated by corner reflectors, appear to be the brightest, while the Pacific Ocean, belonging to flat surfaces, appears to be darkest in the SAR image.

2.6.1 Across-Track SAR Interferometry for Generating Digital Elevation Map

One of the most widely used applications for InSAR is generating DEMs. Assuming only one dominant target exists within the resolution cell, its location in the elevation direction can be measured by adding another measurement from slightly different angle. In this case, the phase difference of two SAR images depends only on the travel path difference. The principle of interferometric radar has been described in details by many sources [Zebker and Goldstein (1986); Rosen et al. (2000); Rodriguez and Martin (1992)]. For the sake of brevity, we only introduce the main principle and theory in the following section.

The configuration used for the general InSAR is depicted in Figure 2.6.

Two SAR sensors, at an elevation height H, fly on parallel tracks and view the Earth surface from slightly different directions. The separation of the flight path is called baseline,

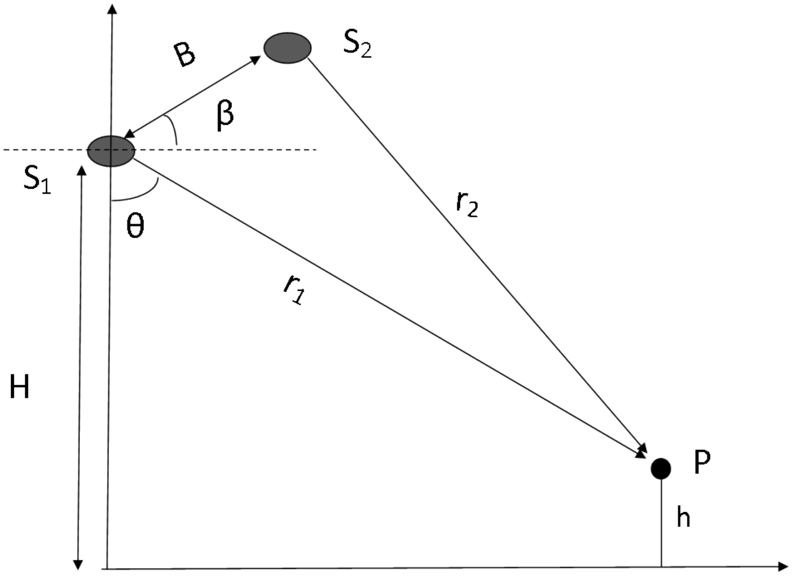

Figure 2.6: Basic configuration of InSAR. $S_1$and S_2 can represent two antennas viewing the same surface simultaneously or one antenna viewing the same surface on two separate passes. The flight pass is perpendicular to the plane of the drawing. θ is the viewing angle, h is the height of the point P above the reference surface and B denotes the spacial distance from two sensor locations.

B , with its component perpendicular to the look direction called perpendicular baseline, referred to as $B_\perp$. For a target on the ground P, the ranges measured from two SAR sensors to the target are r_1,r_2 respectively. If viewing geometry is known, the target height h can be derived from the phase measurement with a high precision. The retailed derivation can be found in [Rosen et al. (2000)]. Briefly, the phase difference is related to the slant range distances as:

$$\Delta\phi = \frac{4\pi}{\lambda}(r_1 - r_2). \tag{2.13}$$

For a spacecraft system, where $r_{1,}r_2 \gg B$, using the plane wave approximation, the path difference is related to the angle as :

$$r_1 - r_2 = B sin(\theta - \beta), \tag{2.14}$$

where β is the orientation angle of the baseline and θ is the look angle. Also from the geometry, we have

$$h = H - r_1 cos(\theta). \tag{2.15}$$

The above equations can be combined to express the unknown topography *h*, as follows:

$$h = H - r_1 sin(cos^{-1}\frac{\Delta\phi\lambda}{2\pi B} - \theta). \tag{2.16}$$

The height sensitivity factor is given by

$$\frac{\partial\Delta\phi}{\partial h} = \frac{4\pi}{\lambda}\frac{B_\perp}{r_1 sin(\theta)}. \tag{2.17}$$

The key parameter measured from two SAR images is the differential phase. To get the differential phase $\Delta\phi$, the common practice is to generate an interferogram. The interferogram for the whole scene is generated by multiplying pixel by pixel the image I_1 with the complex conjugated image I_2 . Figure 6.1 shows an interferogram from Haiwaii Island. The intensity of the image pixel represents the magnitude of the cross correlation and the color represents the differential phase.

Unfortunately, the phase is represented as modulo 2π only, which is called “wrapped phase”. Thus a phase unwrapping step has to be carried out to obtain the absolute phase, which finally can be transformed to the desired height *h* at each point over the range - azimuth plane. In this way, InSAR can be used to generate high-resolution topographic maps of terrain. The procedure of InSAR-DEM production mainly comprises:

1. Two SLC images acquired at slightly different locations first have to be focused, and then co-registered in order to compensate for the range differences between two acquisitions

2. A multi-looking step is needed to reduce the thermal and speckle noise.

3. For each pixel (x, r), estimate the corresponding interferometric phase through averaging adjacent pixels. Denoting *L* as the multi-look size, the phase is obtained as follows:

$$\Delta\phi(x, r) = arg\left\{\sum_{l=1}^{L} y_{1,l}(x, r)y^*_{2,l}(x, r)\right\}. \tag{2.18}$$

4. The resulting phase has to be unwrapped to remove the 2π ambiguity.

5. Finally, the height information can be retrieved through Equation 2.16.

The DEMs we use for our thesis are from the Shuttle Radar Topography Mission (SRTM). The SRTM mission uses a single-pass interferometer with an effective baseline of 30 m to map 80% of the Earth land surface. The absolute vertical accuracy of the elevation data can be 16 meters (at 90% confidence). A typical example DEM generated through an X-band SRTM is shown in Figure 2.7

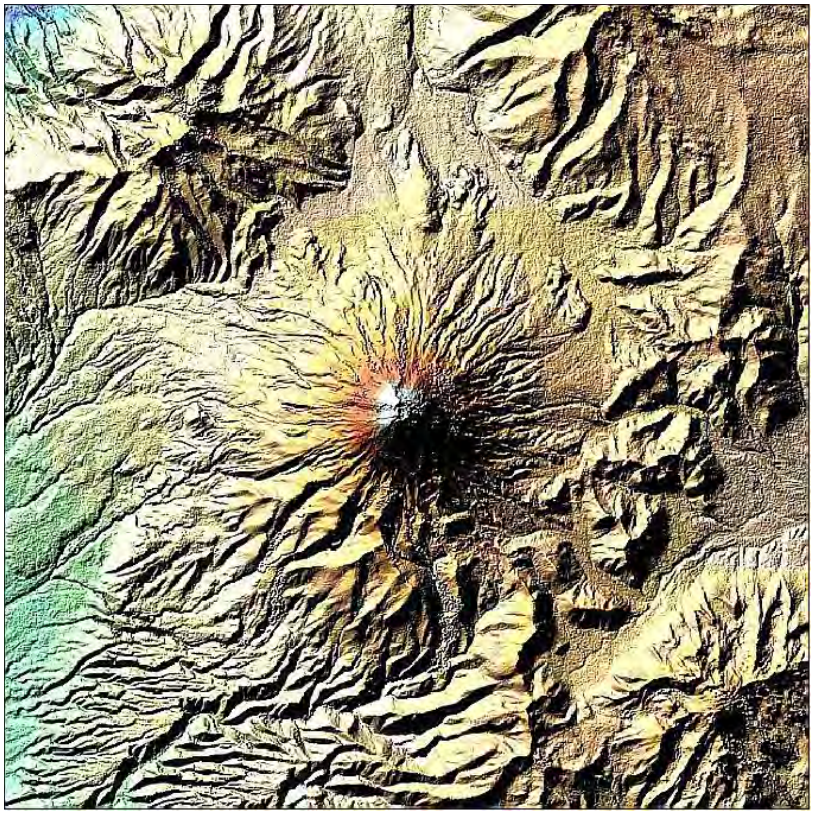

Figure 2.7: The X-SAR/SRTM digital elevation model shows Mt. Cotopaxi in Ecuador, the highest active volcano in the world. (Image credit: DLR, NASA)

2.6.2 Differential SAR Interferometry

The two images used for InSAR can either be obtained by using two different sensors on the same platform (single-pass interferometry) or by using the same sensor at two different parallel or near parallel passes over the area (repeat-pass interferometry). Repeat-pass interferometers utilize a single antenna, hence a small platform, and therefore are less expensive and more realizable. In current InSAR systems, the majority of SAR satellites are in the repeat-pass mode, which means the two images for interferometric processing are acquired at different times. The repeat cycle typically ranges from 20 to 46 days. Figure 2.8 illustrates the repeat-pass scheme.

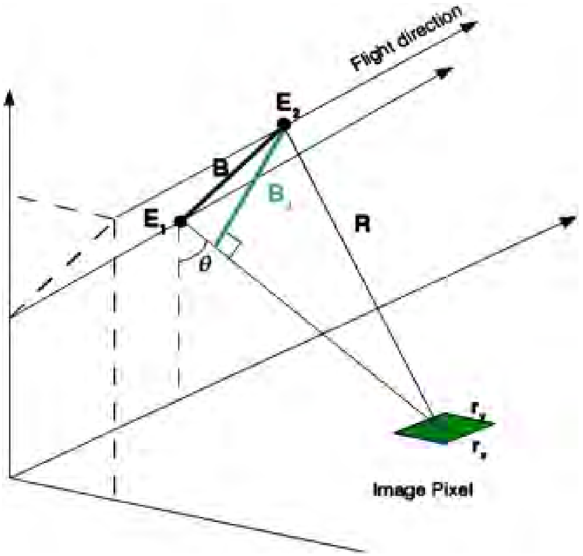

Figure 2.8: A typical configuration for a repeat-pass InSAR. $E_1$and E_2 represent position of the radar for the two passes separated by the baseline B. The InSAR maps pixels of resolution r_x, r_yin the range and azimuth direction from a look angle of θ. Difference in phases of the electrical filed backscattered from the pixel at the two locations is used to derive the height estimation.

During the time interval between two SAR observations, the terrain to be imaged is subjected to changes (subsidence, landslide, earthquake,etc.), as illustrated in Figure 2.9.

A movement in the line-of-sight direction results in an additional differential phase shift

$$\Delta\phi_d = \frac{4\pi}{\lambda}\Delta R \tag{2.19}$$

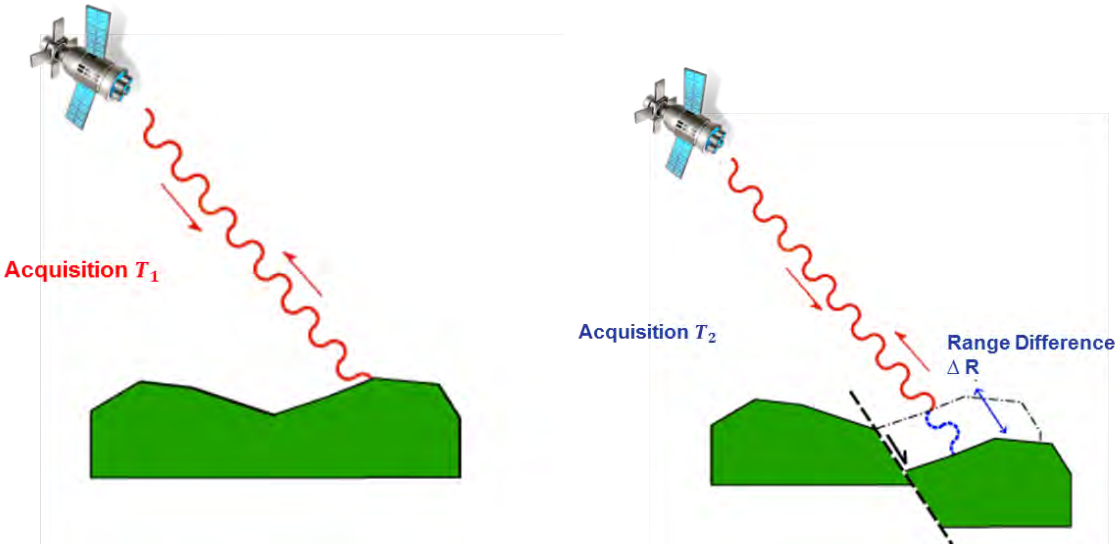

Figure 2.9: Differential SAR interferometry

where ΔR is the relative scatter displacement projected on the slant range direction. This means the differential phase containing both topography and deformation information. If a digital elevation model is available, the topography contribution can be removed and the residual phase is the measurement of deformation. The procedure to remove the topography phase is called phase flattening. This technique is called differential synthetic aperture radar interferometry (DInSAR) [Gabriel et al. (1989); Zebker and Rosen (1994)]. DInSAR has the capacity for mapping the surface deformations with centimeter to millimeter accuracy.

2.6.3 Coherence

The interferometry of two SAR acquisitions is based on the assumption that the scatters and their phases are identical in both images, thus yielding a perfectly defined phase difference. In reality, however, several phenomena will disturb this assumption and lead to different kinds of decorrelation:

- change of the backscattering properties of the scene between the two acquisitions,
- differences in the information content of the images caused by different viewing angles,

- thermal noise of the radar system hardware,
- other errors introduced during the process.

Change in the scene during the two acquisitions, leading to the loss of coherence, is an important error source in InSAR measurements [Zebker and Villasenor (1992)]. In the following, we provide an extensive analysis of the coherence in repeat-pass interferometry.

A commonly used measurement of coherence in InSAR is defined as the mutual correlation coefficient between two images. The coherence value ranges from 0 (complete decorrelation) to 1 (full coherence). The complex coherence between two SAR signals, $s_1$and s_2 ,is defined as

$$\rho = \frac{E\left(s_1 s_2^*\right)}{\sqrt{E\left(|s_1^2|\right)E\left(|s_2^2|\right)}} \tag{2.20}$$

where ρ is the coherence value, $E\left(.\right)$ is the expectation and * is the complex conjugate. From this definition, the coherence is estimated by ensemble average, which means the expectation value can be obtained by using a suite of observations for every single pixel. This requires a large number of interferograms acquired simultaneously and under exactly the same condition. However, in reality, this is impossible since every pixel is observed only once during each SAR acquisition. If one assumes the observation of a small region to be stationary, under the assumption of ergodicity, it is possible to exchange the ensemble average with a spatial average. Thus, to estimate coherence, we choose a local window, typically a rectangular window in radar coordinates representing a square region on the ground. The estimator of coherence $\hat{\rho}$ is

$$\hat{\rho} = \frac{|\sum\limits_{i=1}^{L} s_1 s_2^*|}{|\sum\limits_{i=1}^{L} s_1^2||\sum\limits_{i=1}^{L} s_2^2|} \tag{2.21}$$

where L is the total number of pixels in the local window and the summation is taken over all the pixels within the window. Figure 2.10 shows the interferogram and estimated coherence map for a SAR image acquired over Hawaii. From the coherence map, the soil and rock areas show a high coherence value while the vegetated and sea areas show a low coherence, where the average value drops to below 0.3.

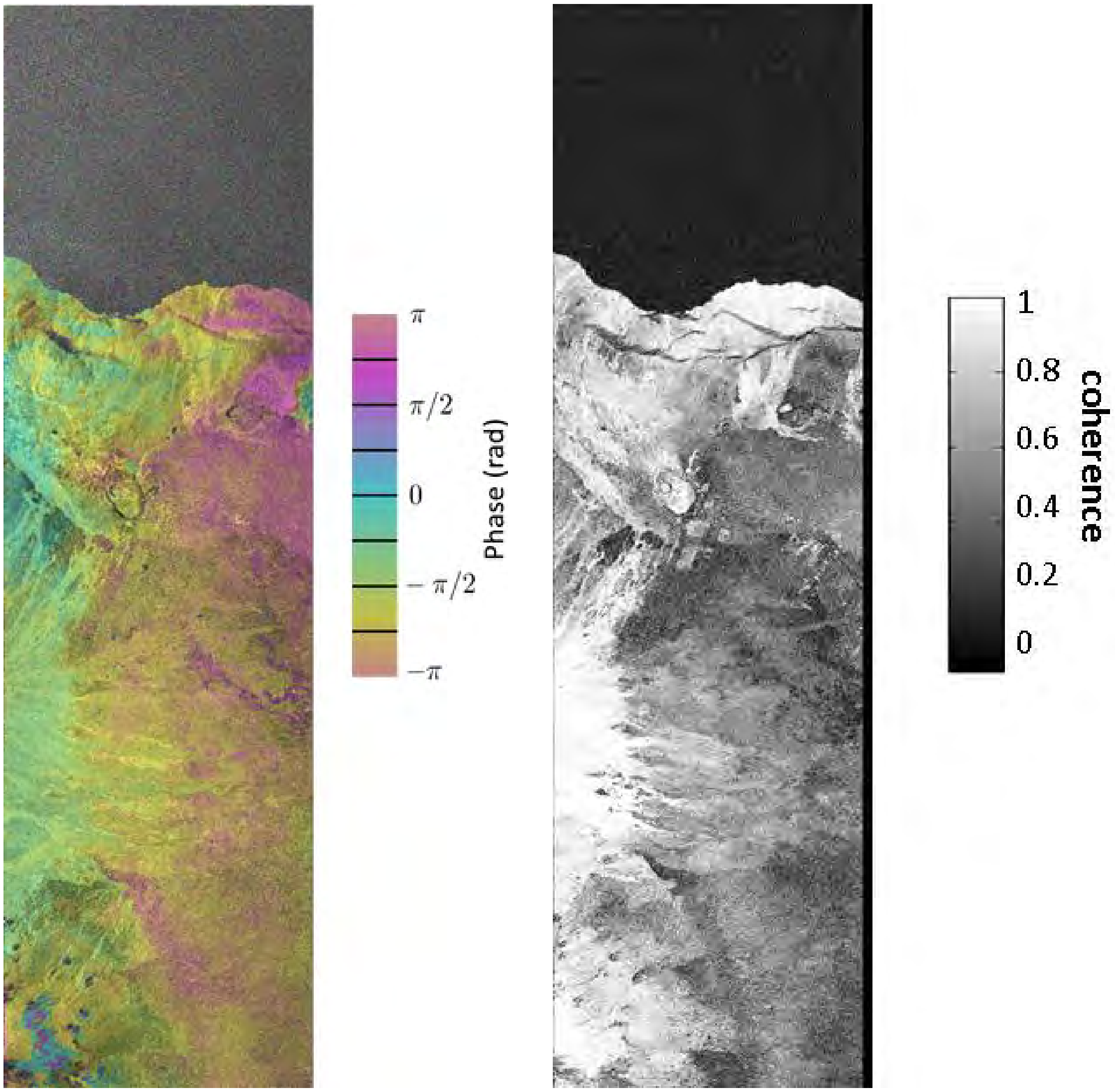

(a) A SAR Interferogram

(b) The Coherence map of the interferogram

Figure 2.10: An Interferogram and its coherence map from Hawaii

2.6.4 Bias in the Sample Coherence Estimation

Even though the coherence estimation in Equation 2.21 is suited for stationary scenes, it is simply the maximum likelihood estimation (MLE) of the coherence magnitude and is still biased. For the coherence of a jointly complex Gaussian process (s_1, s_2), denoting sample coherence magnitude d as the estimation of the true coherence magnitude ρ, L as the number of integrated independent samples and F as the hypergeometric function, an analytical expression for its probability density function (PDF) was derived and presented in [Touzi and Lopes (1996)] as follows:

$$p_d(d|\rho) = 2(L-1)(1-\rho^2)^L d(1-d^2)^{L-2} F(L,L;1;\rho^2 d^2). \tag{2.22}$$

The expected estimated coherence is

$$E(d) = \frac{\Gamma(L)\Gamma(1+1/2)}{\Gamma(L+1/2)} F_{2,3}(3/2,L,L;L+1/2:1:\rho^2)(1-\rho^2)^L. \tag{2.23}$$

Figure 2.11 presents the estimated coherence $E(d)$ as a function of the coherence magnitude ρ and the number of looks L taken. It can be seen that the sample coherence magnitude d is biased towards higher values when the number of independent looks is small. This results in the reduction of contrast, especially between areas of differing low coherence. The bias decreases with increasing number of independent looks L as the MLE estimate is asymptotically unbiased.

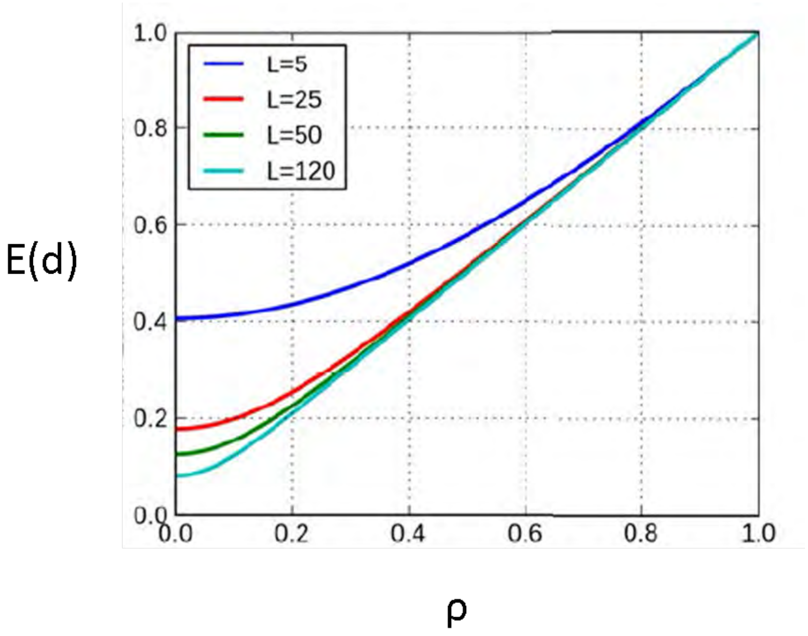

Figure 2.11: Coherence magnitude bias for the various number of statistically independent looks

2.6.5 Decorrelation in Repeat Pass SAR Interferometry

Interferometric phase noises have many independent sources, thus the observed correlation can be broken down to several components [Zebker and Villasenor (1992)]

$$\rho = \rho_{geom} \cdot \rho_{thermal} \cdot \rho_{vol} \cdot \rho_{temp} \cdot \rho_{other}. \tag{2.24}$$

The different factors are also referred to as decorrelation sources, each of them ranges from 0 to 1. The detailed discussion of each source follows.

Geometric Decorrelation

Geometric decorrelation, also referred to as baseline decorrelation, is reflective of loss of the coherence in an interferogram due to a slight change in the viewing geometry. Within a resolution element (r_x, r_y), the sum of the radar returns from several individual scatterers will be different if viewed at two different angles. This change in viewing angles is proportional to the interferometric baseline. Geometric decorrelation can be further broken down into spatial decorrelation and rotational effects, where the former is a function of the perpendicular component of the interferometric baseline and the latter is a function of parallel component. Since the orbits of spaceborne sensors are parallel, rotational effects are essentially zero. Hence the geometric correlation is given in terms of perpendicular baseline :

$$\rho_{geom} = \begin{cases} 1 - |B_\perp|/B_{crit}, & |B_\perp| \leq B_{crit} \\ 0 & otherwise \end{cases}, \tag{2.25}$$

where $B_\perp$is the perpendicular baseline, and the critical baseline B_{crit} is defined in [Zebker and Villasenor (1992)] as:

$$B_{crit} = \frac{R_0\lambda}{2r_y cos\theta}, \tag{2.26}$$

where R_0 is the range to the first range pixel, λ is the wavelength, θ is the look angle, r_y is the range resolution of the radar. From Equation 2.25, we can see when the perpendicular baseline $B_\perp$ goes beyond the critical baseline B_{crit}, the coherence goes to zero, which means no meaningful interferogram can be generated.

Volume Decorrelation

The volumetric decorrelation is reflective of scattering from multiple heights within each resolution element. For area with high penetration, such as pine forests and ice, volume decorrelation dominates. The observed correlation can be modeled as the Fourier transform of the radar backscatter volume as a function of height

$$\rho_{vol} = \frac{\int \sigma(z) exp^{-jk_z z} dz}{\int \sigma(z) dz} \tag{2.27}$$

where $\sigma(z)$ is the effective radar backscatter cross section per unit height z , k_z is the vertical wavenumber given by

$$k_z = \frac{4\pi B_\perp}{\lambda R sin\theta}. \tag{2.28}$$

The function $\sigma(z)$ is dependent on the target. For example, when scatterers are only distributed on the surface, such as a flat field, $\sigma(z)$ can be approximately as an impulse function, $\delta(z - z_0)$ with z_0 being the height of the ground. In this case, there is no volume decorrelation. In another case, a volume scattering target with uniform backscatter as a function of height, such as a forest that extends up to a scattering height of h_v, the volume decorrelation is maximized, reflecting a "worst case" scenario. The corresponding volumetric decorrelation from such a scattering model is given by

$$\rho_{vol} = \frac{2sin(k_z h_v/2)}{k_z h_v}. \tag{2.29}$$

From the above equation, we can see that the tree height can be estimated under the assumption of uniform effective radar backscatter cross section and no surface return. Polarimetric SAR interferometry is based on the same theory but a different volume scatter model to estimate the forest height. However, this methodology is hindered by the presence of other decorrelation sources such as temporal decorrelation and thermal decorrelation, as well as the unquantified bias introduced by the physical models.

Temporal decorrelation

When individual scatterers change relative positions within a resolution element during the time between the two SAR acquisitions, it introduces a loss of coherence called temporal decorrelation. Temporal decorrelation is difficult to quantify since we do not have in situ data on statistical distribution of the scatterer motions. If the scatterers follow standard distribution, the temporal decorrelation can be modeled. For example, when the scatterer motion in horizontal and vertical directions are independent and follow a Gaussian distribution with mean distance of $\sigma_{motion,y}$ and $\sigma_{motion,z}$ respectively, the temporal decorrelation is given analytically by

$$\rho_{temp} = exp\left\{ -\frac{1}{2}\left(\frac{4\pi}{\lambda}\right)^2 \left(\sigma^2_{motion,y} sin^2\theta + \sigma^2_{motion,z} cos^2\theta\right)\right\}. \tag{2.30}$$

Thermal decorrelation

Additive thermal noise ϕ_{noise} in interferometric data reduces coherence. This loss of coherence is referred to as $\rho_{thermal}$. The additive thermal noise is incoherent with the received signal and different in both interferometric channels, leading to another phase error. Since thermal decorrelation results from the variance in thermal noise, it is directly linked to the SNR of the received signal. We can calculated the thermal decorrelation from SNR as :

$$\rho_{therm} = \frac{1}{1+1/SNR}. \tag{2.31}$$

In most cases, the SNR for SAR images is high enough to ignore this effect. Exceptions include special cases when the SNR is significantly low, such as SAR images over a sandy surface.

Other decorrelation factors

Beyond the above decorrelation factors, there are a number of other noises, which are denoted by ρ_{other} in Equation 2.24. Other factors may include missing lines or other errors in the raw data, high phase gradients that are misinterpreted as phase noise, errors in coregistration and other processing errors.

2.7 Summary

In this chapter, we have introduced some of the terms required to understand SAR and InSAR imaging as described in the rest of the text. We have discussed the geometry of SAR imaging, the principles of SAR interferometry and differential SAR interferometry, especially the concept of coherence for measuring phase errors. For a more in-depth treatment of SAR imaging and system engineering, the reader is referred to the following [Skolnik (1970); Rodriguez and Martin (1992); Soumekh (1999); Franceschetti and Lanari (1999); Oliver and Quegan (2004)].

Chapter 3

Synthetic Aperture Radar Tomography

In Chapter 2, we have illustrated that SAR has the ability to generate high resolution two dimensional (2-D) images of the backscatter properties of illuminated areas. However, the Earth is three dimensional (3-D). Due to the intrinsic side-looking geometry of the imaging system, the resulting image is only a projection of the 3-D scene to the azimuth slant-range plane. This means all targets lying in the same constant-range contour will be received by the radar at the same time, and therefore can not be distinguished. The constant-range contours intersect the ground patch are described as circular arcs. As illustrated in Figure 3.1, the radius of the circular arc is given by the range distance, the length and width of the arc are provided respectively by the azimuth and range resolution, the angle of the arc is determined by the antenna beamwidth.

Though InSAR (see Section 2.6) can generate high-precision topographic maps of the Earth, it implicitly assumes that all scatterers only appear on the surface level. However, the assumption does not hold in the following scenarios:

1. The surface topography is steep enough to generate a critical projection of the scatterers in the slant imaging geometry (called layover in InSAR).
2. The imaged area is characterized by a high spatial density of strong scatterers, e.g. urban areas.
3. Radiation penetrates under the surface such as forested areas, glaciers and arid zones.

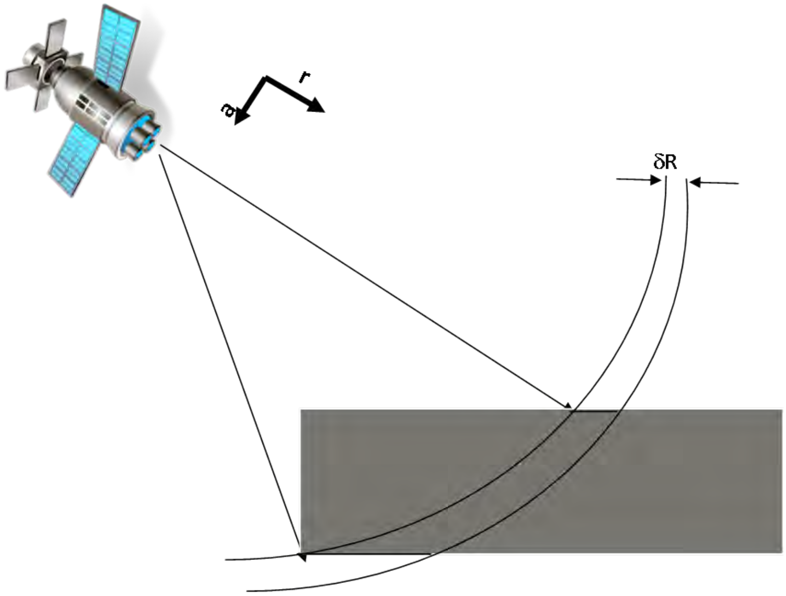

Figure 3.1: Illustration of SAR image projection. Reflections from all scatters within the circular ring are recorded in the same pixel.

In these conditions, the signal received in a pixel contains the superposition of responses from multiple scatterers. Existing InSAR and DInSAR algorithms cannot separate the multiple scatterers in the same pixel, resulting in degraded performances in these situations. Precise target height estimation, precise target geolocation, as well as tracking the number of scatterers can be important issues that need to be further addressed for better monitoring over these complex scenarios.

To overcome limitations of conventional 2-D SAR imaging in these conditions, we introduce a new SAR technique called SAR tomography (TomoSAR). SAR tomography uses multiple SAR images of the same area acquired from slightly different orbits to establish a synthetic aperture in the elevation direction. Through this scheme, SAR tomography is able to achieve a full 3-D reconstruction of the mapped scene. In this chapter, we cover the relevant theory for the introduction and discussion of SAR tomography. Based on the theory, we establish the signal model and propose the Capon beamformer as the reconstruction algorithm. Finally, we compare the performance of the proposed Capon beamformer with the traditional Fourier based method via simulation.

3.1 State of the Art for SAR Tomography

The idea of tomographic imaging was first introduced to the SAR community in 1990s [Piau (1994); Jakowatz and Thompson (1995); Homer et al. (2002)] as a way to overcome limitations of the standard 2-D imaging. Similar to computed axial tomography (CAT) in medical imaging, it uses images acquired from various locations to form a synthesized aperture in the elevation dimension. SAR tomography raises great research interests due to a large number of potential applications ranging from geology, biomass estimation, forestry, detection of buried structures for archaeology to civil applications. The first experiment was carried out in a laboratory with ideal experimental conditions [Pasquali et al. (1995)] or by using airborne systems [Reigber and Moreira (2000)]. Since then, the technique has developed considerably. Current research is mainly carried out to explore applications of SAR tomography and to develop better methodologies for tomographic reconstruction.

However, research on 3-D SAR tomography using spaceborne systems is still quite limited and not yet well assessed [Fornaro et al. (2005); Homer et al. (2002); She et al. (2002)]. Notwithstanding, developments of SAR tomography for spaceborne systems will join the vast potentials of advanced imaging techniques to the synoptic view capabilities [Gini and Lombardini (2002)], and are also fundamental to future four-dimensional (4-D,space-time) SAR imaging, i.e., to techniques that not only separate point scatterers interfering in the same azimuth-range resolution cell, but also estimate their relative deformations [Fornaro et al. (2009)].

Research on SAR tomography using spaceborne systems is still at an early stage and issues associated with real data processing need to be further addressed and solved.

3.2 SAR Tomography Problem Formulation

3.2.1 Geometry Model of SAR Tomography

SAR tomography uses a stack of SLC SAR images obtained by multiple parallel baselines to reconstruct scatterers located at the same azimuth-range resolution cell, but at different elevation locations. The geometry of multiple baseline SAR tomography is depicted in Figure 3.2.

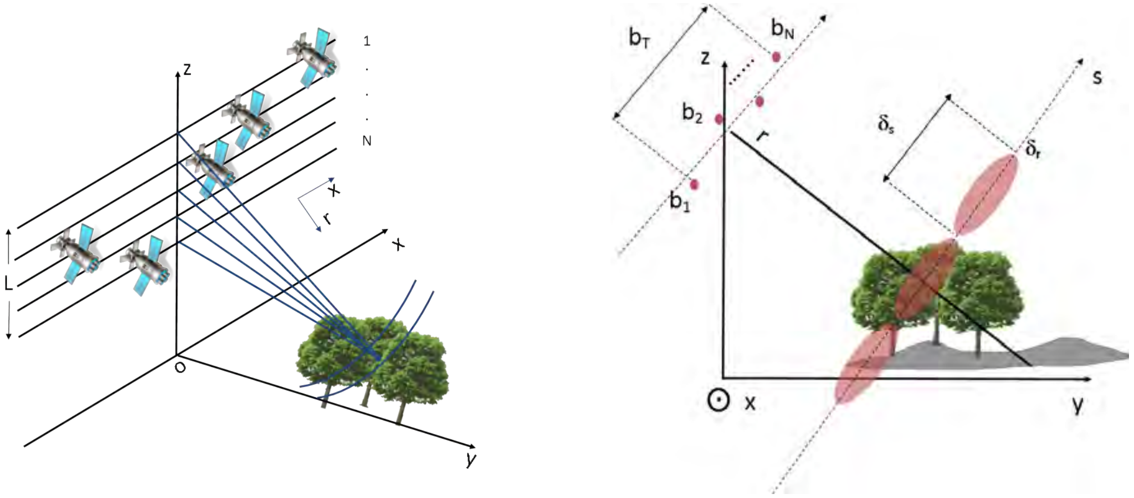

(a) Acquisition geometry of multiple baseline SAR tomography.

(b) Simplified geometry in the slant range - elevation plane

Figure 3.2: Geometry of multiple baseline SAR tomography. A forest area is seen by N sensors on parallel flight track.

For the system depicted in Figure 3.2, we have N SAR passes over a forest area to enable SAR tomography, each one observing the scene from a slightly different look angle. All passes are parallel for sake of simplicity. In each pass, the sensor is moving along the azimuth direction x and transmits coherent phase modulated pulses in the range direction r at a regular time interval. y denotes the ground range direction and s denotes the elevation direction. The distance seperating two sensors is called a baseline. The baseline distance between the master sensor and the nth sensor, noted as b_n, can be decomposed into $b_{\|n}$, a component parallel to the slant-range direction, and a perpendicular one $b_{\perp n}$, aligned with the cross-range direction.

A single SLC SAR image gathers the returns acquired by the radar on the desired zone. After that, each image has been focused, registered on a common grid and phase flattened referring to a common track. The main problem in SAR tomography is to develop retrieval algorithms for obtaining elevation reflectivity profiles from the data stack. The pipeline of SAR tomography for forest height reconstruction is showed in the following Figure 3.3.

3.2.2 Signal Model of SAR Tomography

To develop the retrieval algorithm, a signal model relating the obtained signal to the elevation reflectivity profile need to be developed first. The simplified geometry in only slant range and elevation plane is shown in Figure 3.4.

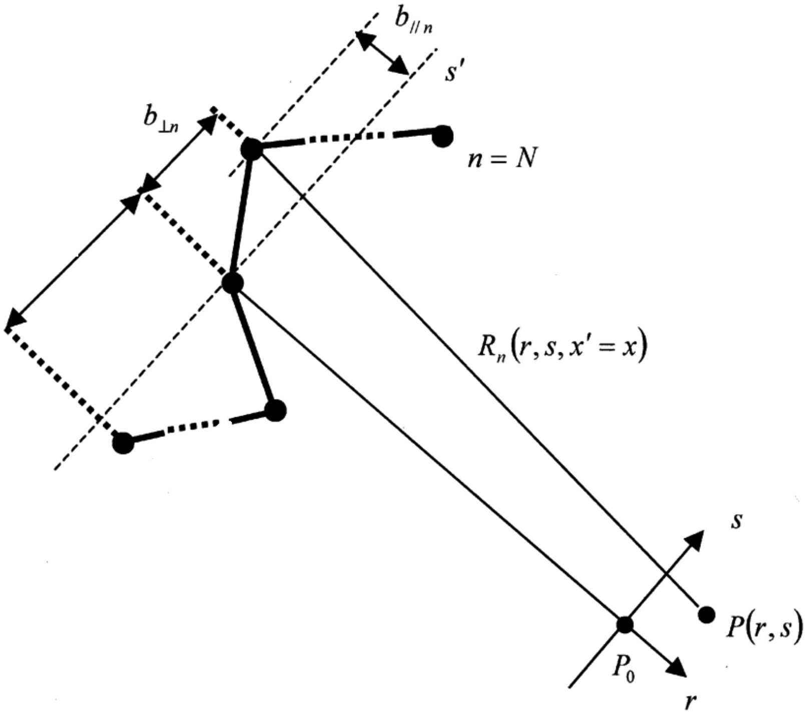

Figure 3.4: Multipass acquisition geometry in the slant range - elevation plane, s denotes the elevation direction, r denotes the slant range direction and $(b_{\|n,} b_{\perp n})$ is the relative position of the nth sensor.

For a scatterer P located at position (x, r, s), with the reflectivity as $\gamma(r, \dot{x}, s)$ and the distance to the nth sensor as $R_n(r, s)$, the resulting radar return at nth sensor from the scatterer P is

$$\gamma(x, r, s) \cdot \exp\left[-j\frac{4\pi}{\lambda}R_n(r, s)\right] **f(x, r) \tag{3.1}$$

where $**$ represents the convolution operation, λ is the operating wavelength, and the function $f(x, r)$ is the post focusing 2-D Point Spread Function (PSF). Typically, with high resolution, the function is given by

$$f(x,r) = \text{sinc}\left(\frac{r}{\Delta r}\right)\text{sinc}\left(\frac{x}{\Delta x}\right), \tag{3.2}$$

where Δx and Δr are the azimuth and range resolution, respectively. Each pixel represents an area whose essential azimuth and range extension is given by Δx and Δr. Referring to Figure 3.4 and applying the Fresnel approximation, the distance can be expressed as :

$$R_n(r,s) = \sqrt{(r-b_{\|n})^2 + (s-b_{\perp n})^2} \approx r - b_{\|n} + \frac{(s-b_{\perp n})^2}{2(r-b_{\|n})}. \tag{3.3}$$

Now expanding to the situation with multiple scatterers, the received radar returns at nth sensor from all the scatterers within the patch can be modeled by the integral in the following form [Bamler and Hartl (1998)]:

$$y_n(x',r') = \int\int dx\,dr\,f(x'-x,r'-r)\int ds\,\gamma(x,r,s)\cdot\ \exp\left[-j\frac{4\pi}{\lambda}R_n(r,s)\right], n=0,\ldots\ldots,N \tag{3.4}$$

This is the fundamental relationship between the multibaseline signal and the complex reflectivity profile. For the sake of simplicity, we assume the post focusing PSF to be approximately the 2-D Dirac function (super high resolution in range and azimuth). Thus, we can simplify a 3-D estimation problem to one-dimensional, only in the elevation direction s where, for each image, the integral applies to an extended region in the presence of subsurface penetration. The result after simplification is

$$f(x'-x,r'-r) = \delta(x'-x)\delta(r'-r) \tag{3.5}$$

$$y_n(x,r) = \int \gamma(x,r,\text{s})\exp\left[\text{j}\frac{4\pi}{\lambda r}R_n(s)\right]ds. \tag{3.6}$$

From Equation 3.3, we can see that the phase factor in Equation 3.6 comprises a quadratic phase term. This distortion can be compensated by multiplying the received signal with the phase factor corresponding to the echo of the center elevation target P_0. This step is often referred to as deramping in SAR processing jargon [Reigber and Moreira (2000)]. Denoting g_n as the received signal y_n after deramping , we have

$$g_n = y_n \exp\left[+j\frac{4\pi}{\lambda}R_n(0)\right] = \int \gamma(s)\exp\left[-j\frac{4\pi}{\lambda}\left(R_n(s) - R_n(0)\right)\right] ds \tag{3.7}$$

where

$$\begin{aligned} R_n(s) - R_n(0) &= |r_0 - b_{\|n}| + \tfrac{(s-b_{\perp n})^2}{2|r_0-b_{\|n}|} - \left(|r_0 - b_{\|n}| + \tfrac{(b_{\perp n})^2}{2|r_0-b_{\|n}|}\right) \\ &= -\tfrac{b_{\perp n}}{|r_0-b_{\|n}|}s + \tfrac{s^2}{2|r_0-b_{\|n}|}. \end{aligned} \tag{3.8}$$

Inserting Equation 3.8 to 3.7, we get

$$g_n = \int \gamma(s)\exp\left[-j\frac{4\pi}{\lambda}\frac{s^2}{2(r-b_{//n})}\right] \cdot \exp\left[j\frac{4\pi}{\lambda}\frac{b_{\perp n}s}{r-b_{//n}}\right] ds. \tag{3.9}$$

Note that the deramped signal has an s^2 dependent phase factor. If only amplitude is of interest, it becomes irrelevant. Otherwise, when the signal phase characteristics are important, this term should be removed via a post processing phase compensation step. For the rest of the analysis, we incorporate this factor into the unknown reflectivity function so that the mathematical relationship to be considered in the following text is

$$g_n = \int \gamma(s)\exp\left[j2\pi\frac{2}{\lambda}\frac{b_{\perp n}}{r-b_{//n}}s\right] ds = \mathrm{FT}\left[\gamma(s)\right]|_{\zeta_n} = g(\zeta)\,|_{\zeta_n}, \qquad n = 0,\ldots N \tag{3.10}$$

where

$$\zeta_n = \frac{2b_{\perp n}}{\lambda(r-b_{//n})} \approx \frac{2b_{\perp n}}{\lambda r}. \tag{3.11}$$

By analyzing Equation 3.10, we can see that the received signals at different orbit locations, in any fixed range and azimuth position, are samples of the Fourier transform (FT) of the reflectivity function along the elevation direction at the frequency described in Equation 3.11. Thus, the complex reflectivity along the elevation direction can be retrieved by simply taking the Fourier transform of the received signals. For data uniformly sampled at a sufficient rate, the discrete values of the reflectivity function along the elevation direction can be directly retrieved via discrete Fourier transform (DFT).

3.3 Limitations of Fourier Based Inversion Method in Spaceborne SAR Systems

However, for most spaceborne repeat-pass acquisition schemes, ideal uniformly spaced parallel flight tracks cannot be obtained. Baselines are usually distributed randomly and have a limited number. As the consequence, with the classical Fourier based method, the resolution of the reconstruction will be quite poor. In the signal processing perspective, the point spread function has high side-lobes, reducing the resolution of the elevation focusing [Reigber and Moreira (2000)].

The relationship between the achievable resolution and the baseline distribution is given by

$$\delta_z = \frac{\lambda r}{2b_{max}} sin(\theta) \tag{3.12}$$

where θ is the radar look angle and b_{max} the total perpendicular baseline span. Equation 3.12 defines the Rayleigh limit, well known in the field of array processing. From the equation, we can see that using the Fourier based method, the elevation dimension resolution is fundamentally limited by the extent of the total baseline. In SAR tomography, in order to remain coherent among all the SLC images, the total baseline b_{max} cannot be longer than the critical baseline B_{crit}. For L-band ALOS PALSAR sensor (detailed parameters are listed in Table 3.1), the critical baseline is 6.5 *km*. Then the elevation resolution can not be higher than

$$\delta = \frac{\lambda r}{2b_{max}} = \frac{0.23\dot{\times}8.49 \times 10^5}{2 \times 6500} m = 15.02\,m. \tag{3.13}$$

This resolution is too coarse for most applications. Thus, more advanced inversion methods are requested to improve the performance.

3.4 Capon Beamforming For Tomographic Processing

One alternative to improve the vertical resolution and suppress the sidelobes is to exploit super-resolution techniques. First, we formulate the problem in a linear system framework. The acquisition geometry depicted in Figure 3.4 and the signal model in Equation 3.10 allow us to cast the tomographic profile reconstruction in the array signal processing framework, where the cross-track array is synthesized by the multiple SAR passes. The continuous model of Equation 3.6 can be discretized along the elevation dimension. Consider an azimuth–range resolution cell (x,r) that contains K scatterers located at different heights. For the kth scatterer, s_k denotes its elevation location and $\gamma(x,r,s_k)$ denotes its reflectivity coefficients. The received signal at the nth pass is

$$y_n(x,r) = \sum_{k=1}^{K} \gamma(x,r,s_k)\exp(j\frac{4\pi}{\lambda r}b_n s_k). \tag{3.14}$$

Further formulated in matrix format, we have the system equation as

$$\mathbf{Y} = \sum_{k=1}^{K} \gamma(x,r,s_k)\mathbf{a}(s_k) = \mathbf{A}\gamma \tag{3.15}$$

where $\mathbf{Y} = [y_1(x,r), y_2(x,r), ..., y_n(x,r), ...y_N(x,r)]^T$ is the measurement vector with N elements, the vector $\gamma = [\gamma(x,r,s_1), \gamma(x,r,s_2), \cdots, \gamma(x,r,s_3), \cdots, \gamma(x,r,s_K)]^T$ with K elements represents the reflectivity coefficients of scatterers in the elevation dimension, and the steering vector $\mathbf{a}(s_k)$ contains the phase information associated with the scatterer located at s_k

$$\mathbf{a}(s_k) = [exp(j4\pi b_1 s_k/\lambda r),\ exp(j4\pi b_2 s_k/\lambda r), \dots exp(j4\pi b_N s_k/\lambda r)]^T. \tag{3.16}$$

The steering Matrix $\mathbf{A}$ consists of K steering vectors corresponding each to a scatterer in the elevation dimension

$$\mathbf{A} = [\mathbf{a}(s_1), \dots \mathbf{a}(s_K)]. \tag{3.17}$$

Consequently, it is possible to apply spatial spectral estimation methods to obtain an estimate of the elevation reflectivity vector γ.

Beamforming is a widely used technique in spatial spectral estimation [Monzingo and Miller (1980)Van Veen and Buckley (1988)]. It allows spatial filtering to separate the signal arriving from a desired direction, and at the same time, suppress interference and noise arriving from other look directions. A beamformer typically weights the signal from each sensor by a properly designed gain and phase shift to obtain the desired output, in the same manner as an FIR filter. The following Figure 3.5 shows the scheme of a spatial filter:

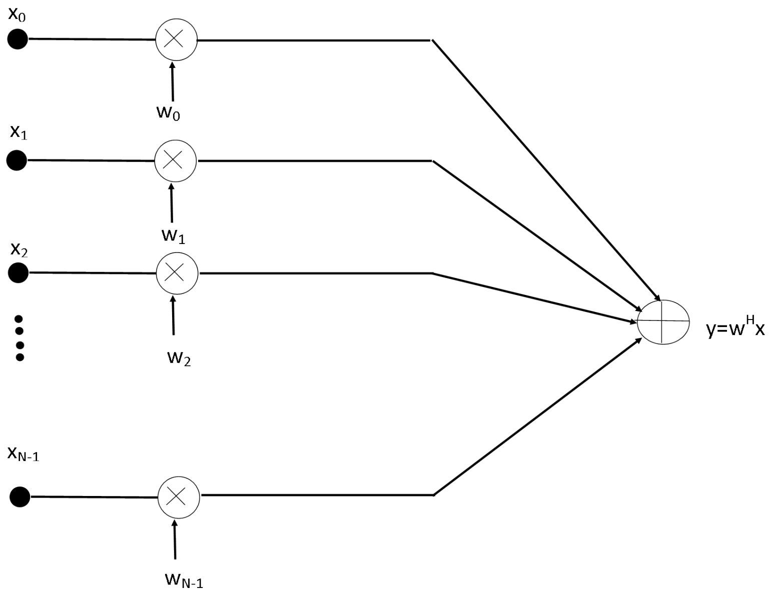

Figure 3.5: Illustration of an array beamformer system

When designing a beamformer, the essential problem is to design a spatial filter as a weight vector w for each elevation location s_k so that the output signal approximates the original signal. Beamformers can be classified as either data independent or data adaptive, depending on the choice of weight vectors. The classical Capon beamformer [Capon (1969)] belongs to non parametric and adaptive beamforming approaches. It adaptively selects the weight vector to minimize the array output power while subject to the constrain that the signal of interest (SOI) does not suffer from any distortion. The combined beamformer output at location s_k is given by

$$y_c[s_k] = w^H\mathbf{Y} = w^H\mathbf{a}(s_k)\gamma(s_k) + \sum_{i\neq k}^{K} w^H\mathbf{a}(s_i)\gamma(s_i) + w^H\mathbf{e} \tag{3.18}$$

where $\mathbf{Y}$ is the measurement vector, $w \in C^N$is the weight vector, $y_c[s_k]$ is the beamformer output at s_k location, $\mathbf{a}(s_k) = [a_{1k}\, a_{2k} \dots a_{Nk}]^T$ is the steering vector at s_k location, $\mathbf{e}$ is the additive thermal noise vector, and $(\cdot)^H$ denotes the conjugate transpose. To recover $\gamma(s_k)$, which is the signal of interest, it has to satisfy the constrain that $w^H\mathbf{a}(s_k) \approx 1$. The other signal, which are interference and noise, should be minimized. This is equivalent to minimize the overall received signal variance, including the desired signal, interference and noise. Thus, it is referred to as a minimum variance beamformer (MVB). The optimal weight vector w can be solved as:

$$w_{capon} = \underset{w}{arg\,min}\,(w^H R_y w), \qquad s.t.\, w^H\mathbf{a}(s_k) = 1. \tag{3.19}$$

The constraint in the above optimization is to prevent the distortion of the desired signal. Usually, the covariance matrix R_y is estimated from multilook samples. Denoting $Y(l)$ as the measurement vector at lth look, the estimation is done through

$$R_y = \frac{1}{L}\sum_{n=1}^{L} Y(l)Y(l)^H. \tag{3.20}$$

The Capon beamformer has an analytical solution given by

$$w_{mv} = \frac{R_y^{-1}\mathbf{a}(s_k)}{\mathbf{a}(s_k)^H R_y^{-1}\mathbf{a}(s_k)}. \tag{3.21}$$

Thus the resulting estimated signal power for Capon beamforming is

$$P(s_k) = \frac{1}{\mathbf{a}^H(s_k)R_y^{-1}\mathbf{a}(s_k)}. \tag{3.22}$$

By computing this output for each elevation location s_k, a 3-D reflectivity reconstruction can be obtained.

Distance from Scene center	r	848.965 km
Orthogonal baseline range	$b_\perp$	4126 m
Wavelength	λ	0.23m
Number of Acquisition	N	10
look angle	θ	23.6
Critical Baseline	B_{crt}	12.592 km

Table 3.1: System parameters for simulation

3.5 Simulation of the Capon Beamformer Performance

In this section, the comparison between the Fourier based method and the Capon beamformer is implemented by simulation and analysis. First, we simulate a data vector received from a point scatterer located at zero height, with SNR of 25dB, taking 16 looks. System parameters are initialized with respect to the ALOS satellite mission as listed in Table 3.1.

The baseline distribution used for the simulation is from a real ALOS dataset (listed in Table 7.3)

$$b = [-4126, -3588, -2909, -2149, -1844, -1672, -1248, -1235, -800, 0][m]. \tag{3.23}$$

To clarify the influence of the nonuniform sampling and its effect, we simulate a uniformly distributed baseline with the same number of acquisitions and range for comparison. The uniformly distributed baseline is listed as:

$$b_{uni} = [-4126, -3667.6, -3209.1, -2750.7, -2292.2, -1833.8, -1375.3, -916.9, -458.4, 0]. \tag{3.24}$$

With a total perpendicular baseline range of $4126m$, the elevation resolution is

$$\delta = \frac{\lambda r}{2b_{max}} = \frac{0.23\dot{\times}8.49 \times 10^5}{2 \times 4126} m = 24.3\,m. \tag{3.25}$$

The reconstructed profile obtained using the Fourier based method is shown in Figure 3.6a, with amplitudes normalized w.r.t the peak value and in dB for easier comparison.

	Fourier based method	Capon beamformer
Resolution (-6 *dB* main lobe width)[m]	25.2	0.8
Side lobe level [dB]	-6.9	-25.7

Table 3.2: The performance comparison between the Capon beamformer and the Fourier base method.

When the Capon beamformer is applied, the reconstructed profile is also shown in Figure 3.6b for comparison.

From Figure 3.6, we first notice that the nonuniform baseline sampling does not impact the system performance much in either Fourier method or Capon beamforming. It is apparent that with Fourier based method, the reconstructed profile of the point scatterer is defocused and has high side lobes. However, with the same nonuniform baseline range, the Capon beamformer has improved the resolution (measured with -6dB main lobe width) by $24.4m$ and suppressed the side lobe level by $18.8\ dB$ (Table 3.2). Thus, the Capon beamformer can significantly improve the reconstruction performance.

3.6 Survey on Other Tomographic Focusing Methods

Vertical dimension focusing is the essential part of the tomographic processing. Both Fourier focusing and Capon beamforming as introduced above are non parametric methods, which means that they do not require any particular model assumptions. Beyond the Fourier based focusing and Capon beamforming, other super-resolution model-based methods have also been proposed by many researchers, including multiple signal classification (MUSIC) [Lombardini and Reigber (2003); Lombardini et al. (2009)] and the weighted subspace fitting (WSF)[Lombardini et al. (2009)]. However, all of these algorithms are based on the assumption that the vertical profile is a superposition of several point-like sources. For truly distributed complex scenarios, e.g., forests, significant model mismatch leads to biased estimations.

Compressed sensing (CS), a new and generalized approach to sensing problems, has also been introduced in the field of SAR tomography [Zhu and Bamler (2012)]. Compressed sensing assumes the vertical scatterers to be sparse and recover the sparse components through an optimization process. Therefore it can be easily adapted to applications in high resolution urban scenes. For scenarios with distributed scatterers from forests, which violates the sparsity assumption, the method can be extended through reconstructing in a sparse wavelet basis [Aguilera et al. (2013)]. The drawback of compressed sensing reconstruction is that its computation is burdensome.

Another alternative approach, applicable to the forest scenario, is to use polarization diversity to separate ground and canopy components by exploiting their uncorrelated polarimetric response. Under this assumption, the covariance matrix of the received signal can be modeled as a sum of two Kronecker products for ground and canopy, respectively. The Kronecker product is composed of a polarimetric component and a structure component. After the separation, the standard tomographic techniques can be subsequently applied on the structure components separately. The covariance matrix decomposition technique has shown great potential in forest scenarios [Tebaldini (2008)].

3.7 Summary

Theoretically, SAR tomography can be used to retrieve the elevation profile of the imaged scenes. The received signals at different orbits and the elevation profile form a Fourier pair. The imaging resolution of spaceborne SAR tomography is limited by the total length of perpendicular baselines, which has to be less than the critical baseline to ensure good coherence over all the SAR images. When a traditional method based on Fourier transform is used, the resolution in the elevation dimension is quite poor and the side lobe level is high. Thus Fourier based methods turn out to be inadequate for the vertical structure estimation. Adaptive beamforming techniques, such as the Capon beamformer, are hence used in this thesis. The simulation experiment comparing the two methods indicates that using Capon beamforming, higher resolution can be achieved and side lobes can be effectively suppressed.

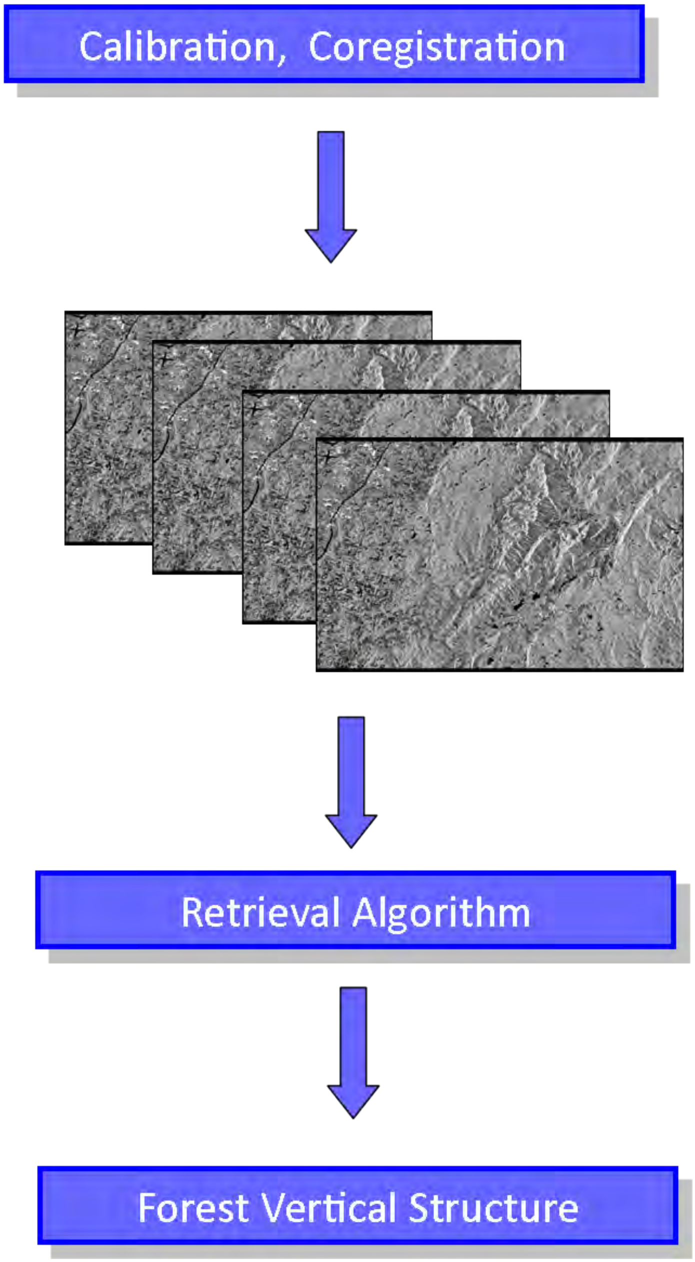

Figure 3.3: Pipeline of SAR tomography. The key step is to develop retrieval algorithms for obtaining elevation reflectivity profiles from the data stack.

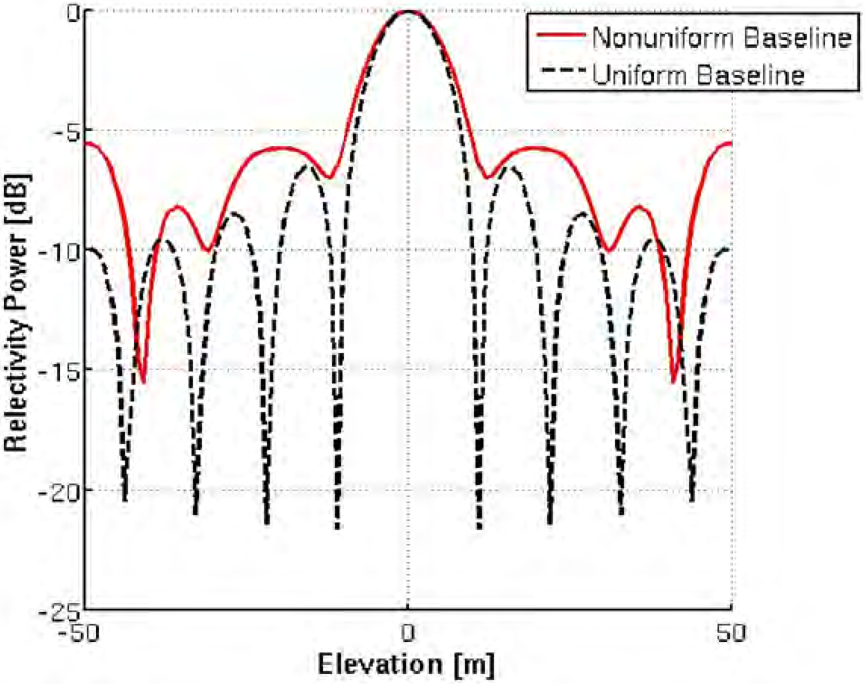

(a) Impulse response of the Fourier based beamformer

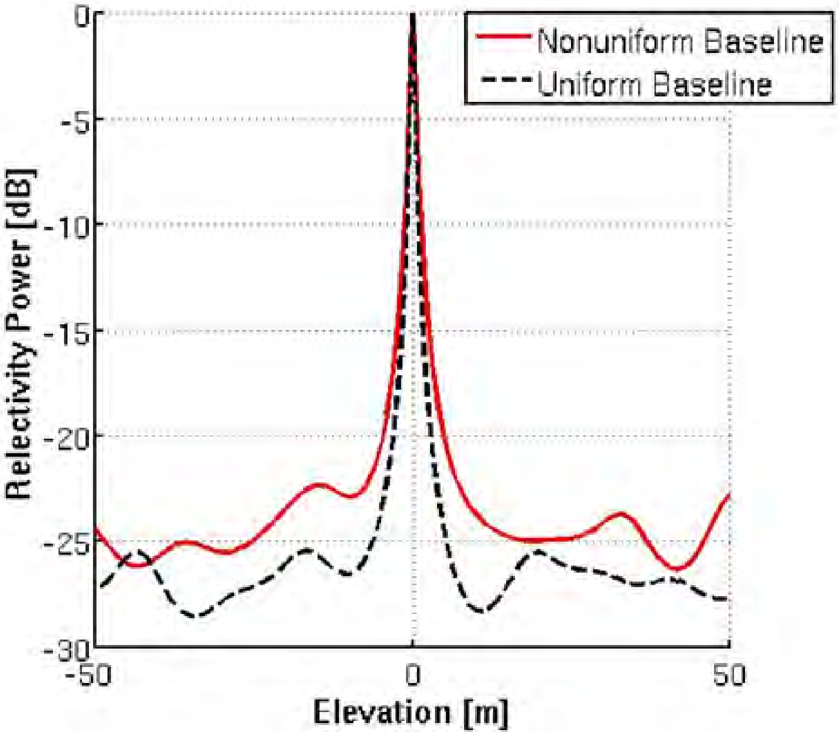

(b) Impulse response of the Capon beamformer

Figure 3.6: Comparison the reconstruction result between the Fourier based method and the Capon beamformer. Red line indicates the result from the nonuniformly sampled baseline distribution while dashed line indicates the result from uniformly sampled baseline.

Chapter 4

Distributed Scatterers in Forest Areas

In the previous chapter, we demonstrated in theory that SAR tomography has the capability to reconstruct the 3D structure of imaged scenes. However, applying SAR tomography for reconstructing forest heights is still a challenging task. This is mainly due to various noise sources in spaceborne SAR images and the complexity of scattering in forest areas. In this chapter, we investigate the speckle noise caused by distributed scatterers in forests, followed by a proposed spatially adaptive speckle filter as the remedy.

4.1 The Expected Vertical Structure of Forests

We begin with a brief discussion about the radar backscattering from forest areas. Excellent previous studies have been done on examining the radar backscatter properties from forest areas [e.g., Freeman and Durden (1998); Sarabandi and Lin (2000); Hyde et al. (2007); Ulaby et al. (1986); Wegmuller and Werner (1995); Dobson et al. (1992); Ranson et al. (1997)]. The backscatter signals from forests depend on the microwave wavelength used by the radar. Widely used microwave frequencies for operational SAR are X-band ($\lambda = 3.1 - 3.5\,cm$), L-band ($\lambda = 24\,cm$) and P-band ($\lambda = 30 - 60\,cm$). Most scattering occurs when the particles are on the scale of the radar wavelength. Thus in the case of forests, L-band backscatter arises more from the trunk and branches of the trees whereas X-band backscatter arises more from their leaves and needles. Also the penetration depth of the microwave in forests varies depending on the frequency. While L- and P-band can penetrate deep into forests, X-band can get get reflection from the canopy level. The resulting forest backscatter seen by SAR systems using different frequencies is shown in Figure 4.1.

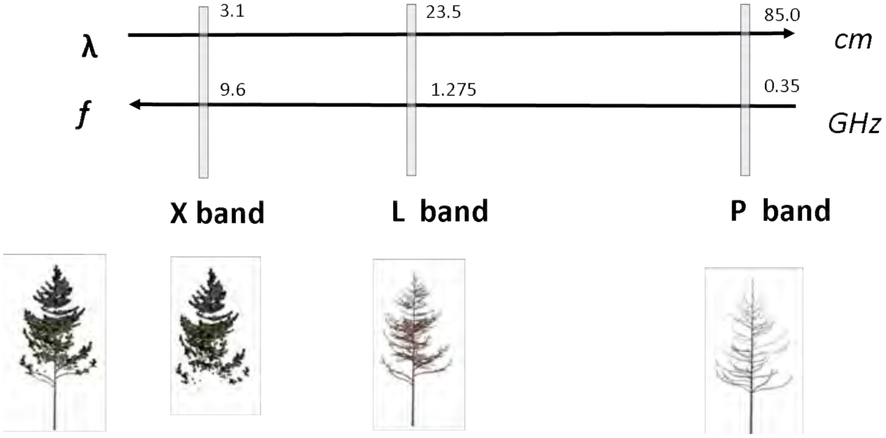

Figure 4.1: Different views of the forest structure seen by SAR systems using different frequency bands. Low frequency microwaves with long wavelength can penetrate deep into forests and can see the forest structure from canopy to the ground. High frequency microwaves can only get reflections from the canopy.

Thus, L- and P-band SAR systems are preferred for forest height estimation for two reasons: 1) L- and P-band microwaves can penetrate the tree canopy and get backscattering from the canopy to the ground; 2) the longer wavelength scatterers like the truck and branches, are more stable, remaining highly coherent over the acquisition period [Le Toan et al. (1992); Schmullius and Evans (1997)].

In L- and P-band systems, forest areas are characterized as the ensemble of the terrain, trunks and canopies, which also include the leaves and branches. There are typically four scattering mechanisms in measured radar returns from forests in L- and P-band:

- Backscattering from canopy;
- Backscattering from ground;
- Double bounce backscattering due to trunk-ground interactions;
- Double bounce backscattering due to canopy-ground interactions.

For single polarization SAR data, different scattering mechanisms cannot be separated but their spatial locations can. In this case, the canopy backscatter gives rise to a distributed scattering mechanism whose equivalent phase center is located above the ground, depending on the canopy height. The ground backscatter and the canopy ground interaction give rise to a distributed, ground locked scattering mechanism. The trunk-ground interaction is equivalent to a point-like scatterer whose phase center is ground locked. Consequently, the associated Fourier spectrum of a forest scene along the elevation direction is an ensemble of an isolated narrow peak at the ground and an angular spread above the ground. The following Figure 4.2 is a schematic illustration of the forest vertical structure.

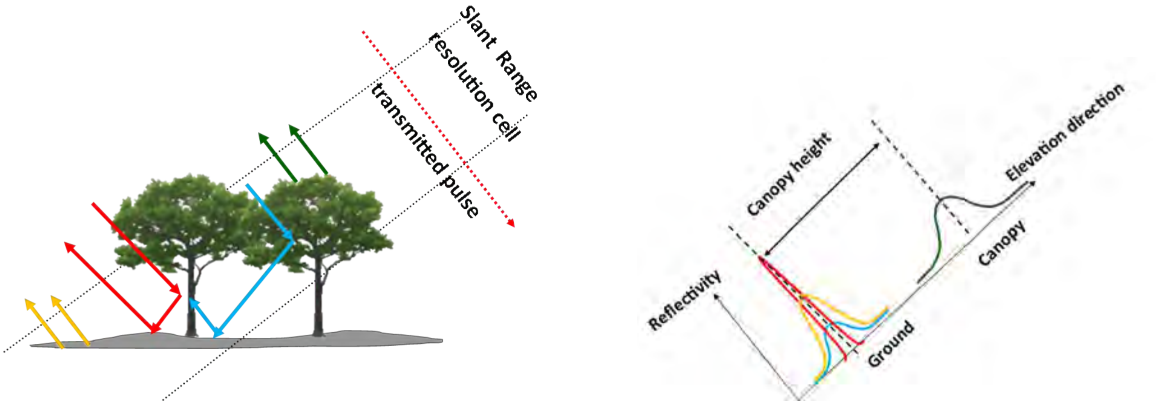

Figure 4.2: The expected vertical reflectivity distribution for single polarizated SAR in forest areas. Yellow: ground scatterring; red: Trunk-ground scattering; yellow; green: canopy backscattering; blue: canopy-ground scattering.

In summary, the forest scattering in SAR imagery consists of a canopy layer and a ground layer. The ground layer consists of all scattering contributions whose phase delays correspond to the absolute ground height z_0. This includes the direct surface scattering at the ground level, the double-bounce scattering between the ground and the tree trunks and branches, and the diffuse volume scattering from a thin layer of underground. The canopy layer represents the scattering contributions from tree canopies.

4.2 Distributed Scatterers and Speckle Noise

From Chapter 2, we know that the received signal at each pixel in a SAR image is a coherent sum of individual reflections from all scatterers within the given resolution cell. When there is only one dominant scatterer within the resolution cell, the received signal shows high phase stability over the whole time period of observation. These targets, often correspond to pointwise deterministic scatterers, are generally called persistent scatterers (PS). Man-made structures and boulders can all generate good PS [Ferretti et al. (2000, 2005); Colesanti et al. (2003)]. However, when there exist many elemental scatterers within the resolution cell, the received signal exhibits strong fluctuations with angle or time. Consequently, the intensity and the phase of the final received signal are no longer deterministic. These targets, referred to as distributed scatterers (DS), usually correspond to natural areas like vegetation or rough surface. The scattering phenomenon of distributed scatterers can be illustrated in Figure 4.3.

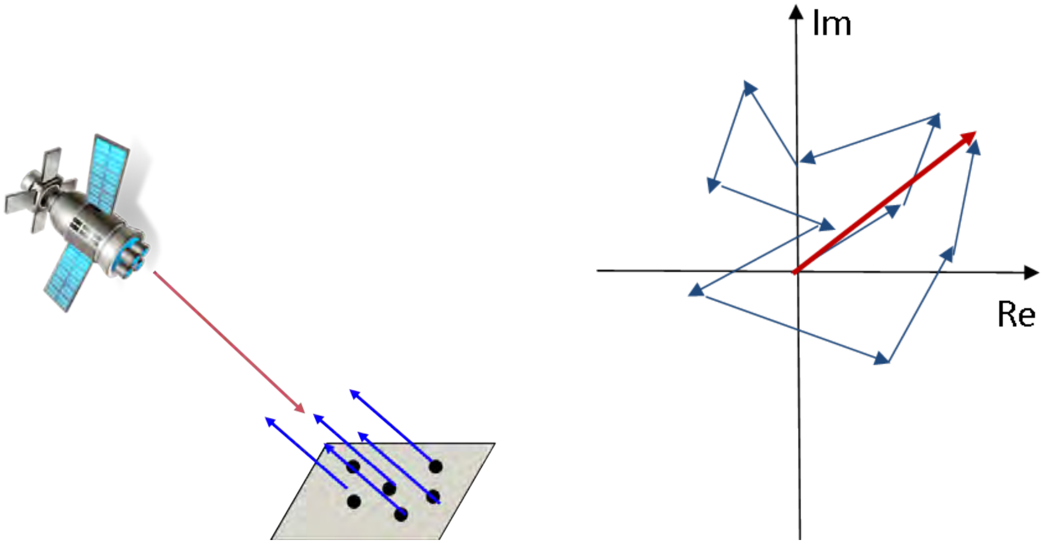

(a) SAR illuminating distributed scatterers (b) Resulting phase of distributed scatterers

Figure 4.3: The radar return from discributed scatterers. For a resolution cell contains many elementary scatterers, the resulting reflected response is the coherent sum of all elemental scatterers. Thus, distributed scatterers show random constructed or destructive returns.

Unlike persistent scatterers, distributed scatterers are strongly affected by temporal, geometrical and volumetric decorrelation, leading to a lower SNR. Consequently, estimating parameters from distributed scatterers is much harder. The forest canopy, with its radar returns from all the leaves and branches, is a typical distributed scatterer. This noise effect can be detected directly from the granular appearance of SAR images on forest areas. The presence of speckle noise can decrease the utility of SAR imagery by reducing the ability to detect ground targets and obscuring the recognition of spatial patterns. For SAR tomography, without removing the speckle noise, the measured SAR signal is of no meaning for fully developed distributed scatterers.

To mitigate the randomness from the forest distributed scatterers, a speckle filter is a prerequisite for tomographic applications in forest areas.

4.3 Spatially Adaptive Speckle Filter

4.3.1 Statistical Properties of Fully Developed Speckle

Consider a regular surface seen by a radar, each image pixel for this surface contains a large number of elementary scatterers. The reflected response can be expressed in following equation:

$$Ge^{j\phi} = \sum_{k=1}^{N} G_k e^{j\phi_k}, \tag{4.1}$$

where G is the amplitude response from the coherent sum of all the scatterers, G_k is the amplitude response from k th elemental scatterer, ϕ is the phase response from the coherent sum of all the scatterers, ϕ_k is the phase response from kth elemental scatterer and N is the total number of scatterers in one pixel. When the following conditions as explained in [Goodman (1976)] are satisfied:

- The response of each scatterer is independent of the others.
- The amplitude G_k and the phase ϕ_k are independent.
- The variables G_k are distributed according to the same probability density function.

- The phase variables ϕ_k are uniformly distributed between $-\pi$ and π.

Then according to the central limit theorem, the received SAR signal can be described by a zero-mean Gaussian variable. In this case, the received signal with the fully developed speckle is usually represented under the form of a simple product model as follows :

$$y = \gamma \cdot \eta, \tag{4.2}$$

where y represents a complex specked scattering coefficient, γ is the original unspeckled scattering coefficient, and η the multiplicative speckle noise. The speckle term η is composed of independent real and imaginary parts, following a circular Gaussian distribution. The multiplicative SAR signal model has been validated over homogeneous agriculture and natural areas, widely used in the modeling, processing and analyzing SAR signals in natural areas [Nyoungui et al. (2002); Lee et al. (1999); Liew et al. (1995)].

4.3.2 Distributed Scatterer Signal Model for SAR Tomography

Accordingly, the signal model of SAR tomography in natural environments with multiple distributed scatterers should be modified to include the multiplicative speckle noise [Gini and Lombardini (2005)]. Extend the model to the multiple scatterers scenario as

$$y_m(x,r) = \sum_{k=1}^{N_s} \gamma_k a_{mk} \eta_{mk}(x,r) + w_m(x,r),$$

where $y(\cdot)$ is the received signal at mth orbit location, γ_k is the reflectivity of kth scatterer, a_{mk} is the phase signature of the kth scatterer to the mth sensor, $\eta_{mk}(x,r)$ is the multiplicative speckle noise term and $w_m(x,r) \sim CN(0,\sigma_w^2)$ is the thermal noise term at a given azimuth range location (x,r). When the multiplicative speckle noises are independent and identically distributed (IID), following the zero mean, circular Gaussian distribution with unity variance, the expected value of correlation between mth and nth received signals is derived as

$$E\left[y_n(x,r) y_m^H(x,r)\right] = \sum_{k=1}^{N_s} \gamma_k^2 a_{nk} a_{mk}^H + \sigma_w^2 \delta_{n-m}. \tag{4.3}$$

Letting $\mathbf{Y}= [y_1\, y_2\, \cdots y_N]^T$ represents the $N \times 1$ vector of multibaseline SAR data at a given location, the expected value of the covariance matrix for the vector Y is

$$R_y = E\left[YY^H\right] = \sum_{k=1}^{N_s} \gamma_k^2(\mathbf{a}_k\mathbf{a}_k^H) + \sigma_w^2 I. \tag{4.4}$$

From the above equations, we can see that the expected covariance matrix of distributed scatterers do not have the speckle noise terms, and thus can be treated as persistent scatterers. The Capon beamformer can also be applied to the distributed scatterers in SAR tomography. Estimating the covariance matrix for the distributed scatterers is equivalent to removing the speckle noise.

4.3.3 The Box Filter

To suppress the fluctuations caused by the speckle noise, we can apply the fundamental result from probability theory that the average of L identically distributed, uncorrelated random variables has the same mean, but $\frac{1}{\sqrt{L}}$ of the standard deviation of one component.

The concept of multilooking is to average a given pixel only with its neighbors which present similar scatter properties. The procedure is a weighted averaging of neighboring complex pixels using a given kernel. This operation is always performed under the hypothesis of statistical homogeneity of the averaged pixels. For the fully developed speckles, assuming ergodicity, after averaging L surrounding pixels, the speckle noise is reduced to:

$$E(\eta) = 1 \quad ; \qquad Var(\eta) = \frac{1}{L} \tag{4.5}$$

Thus, in theory, multilooking would help to reduce the speckle noise. Previous research has also proved it to be an effective method for reducing speckle noise on real SAR data [Lee (1980, 1981)].

The simple box filter is among the most widely used speckle filters in image processing. It is a spatial averaging filter in which all coefficients are equal. The output of such a linear smoothing filter is simply the average of the pixels in the neighborhood of the pixel mask. By replacing the value of every pixel by the average of the pixel values in the neighborhood of the filter mask, the process reduces the speckle noise. A 5 × 5 box filter kernel is shown in Figure 4.4a.

4.3.4 The Spatially Adaptive Speckle Noise Filter

In practice, as the size of the kernel increases, the hypothesis that all the pixels within the kernel are from the homogeneous region soon loses its validity. The sample population will in fact include pixels generated by very different scattering phenomena, such as forests, fields, and streets, and hence possess different statistical properties. Spatially adaptive filters provide a good solution to increase the kernel size with the ability to discard pixels with different properties. A potential kernel with a 5 × 5 spatial adaptive filter is shown in Figure 4.4b.

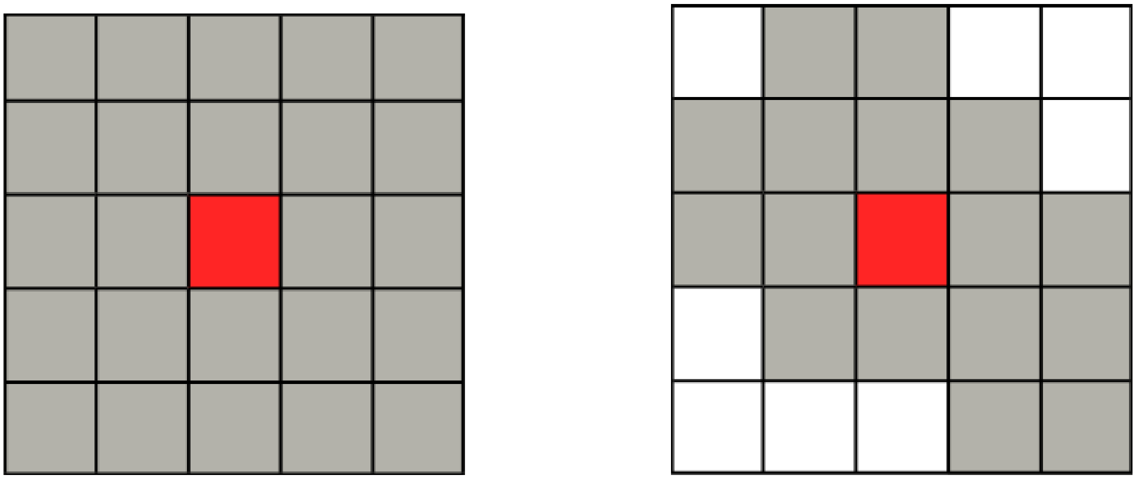

(a) 5 × 5 box filter

(b) 5 × 5 spatial adaptive filter

Figure 4.4: The difference between the 5×5 box filter and the 5×5 spatially adaptive filter. The box filter includes all the adjacent pixels while the spatially adaptive filter only selects the pixels from the homogeneous region.

Compared to the box filter, the spatially adaptive filter is necessary in order to:

- limit the averaging to only those pixels that respect the homogeneity hypothesis;
- preserve the spatial resolution;

- preserve the statistical characteristics of the signal.

4.3.5 The Pixel Selection Algorithm

For designing a spatially adaptive filter in SAR tomgraphy, the key issue is to identify sets of pixels of the homogeneous region from a stack of N SAR images. The amplitude of the complex radar return has been proved to be a suitable measure for distinguishing between different areas inside an synthetic aperture radar image, thus it can also be used to select a suitable set of pixels to average.

First, we have a stack of N complex SAR images co-registered to sub-pixel accuracy and calibrated for each resolution cell. For each resolution, we wish to determine which of the surrounding pixels present a similar statistical behavior. This is possible by noting that for each pixel, we have N realizations of the process that generated the pixel amplitudes by sampling the stack temporally, naturally assuming that the process can be considered stationary over time. This set of N observations can then be used in order to check the degree of similarity between pixel and those of the surrounding pixels, retaining statistically similar pixels while discarding others. The search is constrained to a closed box region around the reference pixel and the measurement we use is the amplitude of the pixel. In the set of N SAR images, let d be the data vector

$$d = [d(1),\, d(2),\, \ldots d(N)]^T \tag{4.6}$$

where ^{T} is transposition, d(n) is the received SAR amplitude signal of nth image of the dataset. For point scatterers, d is a deterministic vector, while for distributed scatterers, d is a random vector. Suppose we have two data vectors d_1 for a image pixel p and d_2 for image pixel q. Since both pixels are from natural areas, vector $d_1$and d_2 are both random vectors following two random processes. Determining whether two random processes follows the same distribution is a common problem in statistics, where it is usually referred to as a goodness of fit test. The problem can be generally defined in a hypothesis testing framework as a test of the null hypothesis : $H_0 : F_{d_1} = F_{d_2}$ that the two distribution of F are the same.

The Kolmogorov-Smirnov test is one of the most popular nonparametric goodness-of-fit test [Lilliefors (1967); Massey Jr (1951)]. It is based on a measure of the maximum distance between the two cumulative distribution functions (CDF). In our case, the two-sample Kolmogorov-Smirnov statistic is

$$D_{KS} = \underset{x}{sup} \left| \widehat{F_p}(x) - \widehat{F_q}(x) \right|, \tag{4.7}$$

where $\widehat{F_p}(\cdot)$ is the CDF of pixel p , $\widehat{F_q}(\cdot)$ is the CDF of pixel q , x is the SAR amplitude value, and D_{KS} is the maximum distance between the two CDFs. If D_{ks} is less than some threshold (0.3 is the threshold chosen for our test), two pixels p and q are considered from the same region. This can be illustrated in following Figure 4.5.

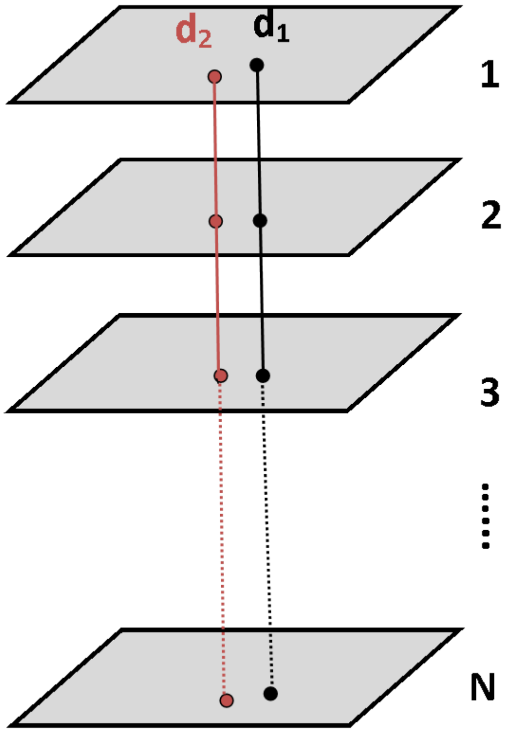

(a) Two nearby pixels for testing whether they from the same distribution

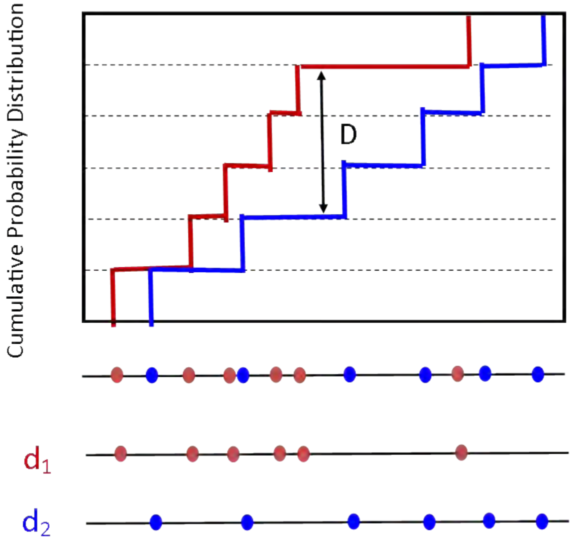

(b) CDF of two pixels

Figure 4.5: The Kolmogorov-Smirnov test for two pixels within the same window. If the largest gap between the CDF of two pixels is below the threshold, the two pixels are regarded from the same distribution and thus, can be grouped together.

The spacial adaptive speckle filter can be applied in the following steps:

1. For each image pixel p, within an estimation window centered on p , select all the surrounding pixels to identify whether these pixels sharing the same statistics as p.
2. By applying the two-sample KS test to amplitude data vectors, find all pixels which are considered as statistically homogeneous with p from all selected surrounding ones .
3. Averaging the covariance matrix of pixel p with the covariance matrix of all surrounding pixels who are considered statistically homogenous with p to reduce speckle noise.

In the following section, we will test the spatially adaptive filter with the real SAR data.

4.4 Test the Spatially Adaptive Speckle Filter on SAR Images

We test the spatially adaptive speckle filter with real ALOS SAR data collected arround Tomhannock Reservoir, a man-made reservoir 6.5 miles northeast of Troy in the town of Pittstown, New York. Figure 4.6 shows the image of this area from Google Map and the corresponding SAR image.

When the phase information of an interferogram of this area is shown in Figure 4.7, we can see that the phase information is quite random. This is due to the fact that this area comprises of forests, vegetated areas and water, of which all are distributed scatterers in radar reflection. Thus, the phase signal is corrupted by speckle noise. Without filtering, the phase information from distributed scatterers cannot be used.

Two different filters for multilooking processing are applied and their results are compared. Figure 4.8a shows the phase image of an interferogram after applying a 5×5 box filter. Though the result shows reduction of the speckle noise, much of the phase information in edge areas of the interferogram is also lost as a cost. In comparison, Figure 4.8b shows corresponding interferometric phase image after a 5×5 spatially adaptive speckle

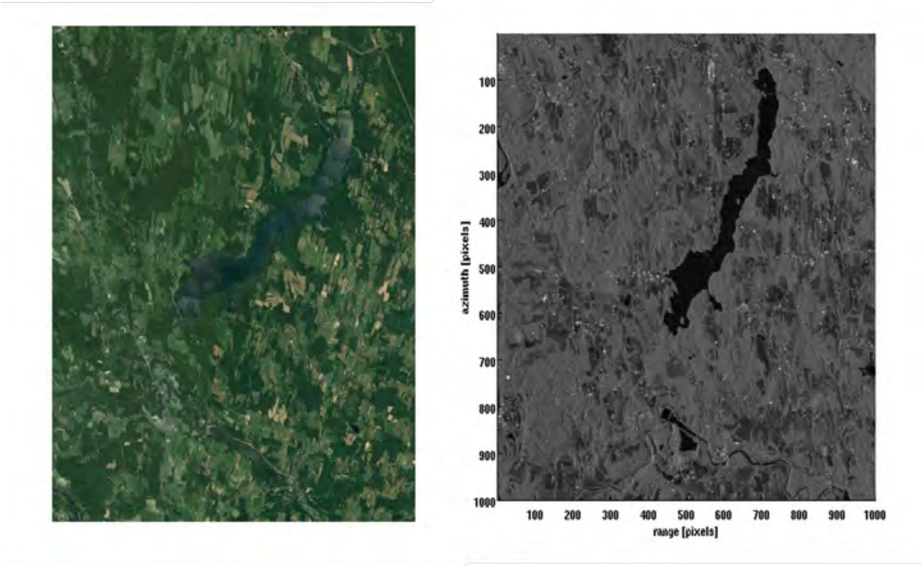

Figure 4.6: Tomhannock Reservoir Area in Google Map and SAR magnitude image

filter. The spatially adaptive speckle filter shows the advantage of reducing the speckle noise while preserving the phase information in all image structures.

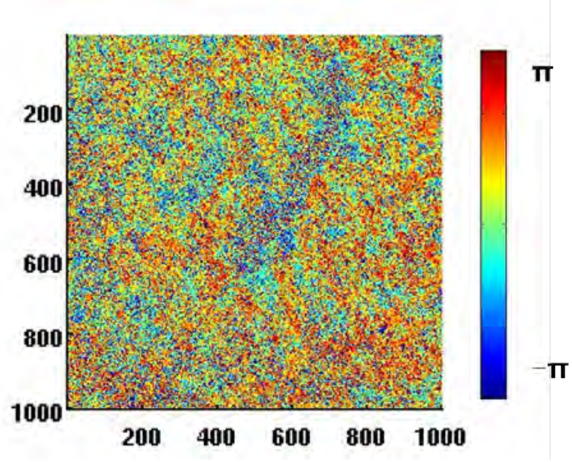

Figure 4.7: Interferometric phase image from Tomhannock Reservoir Area

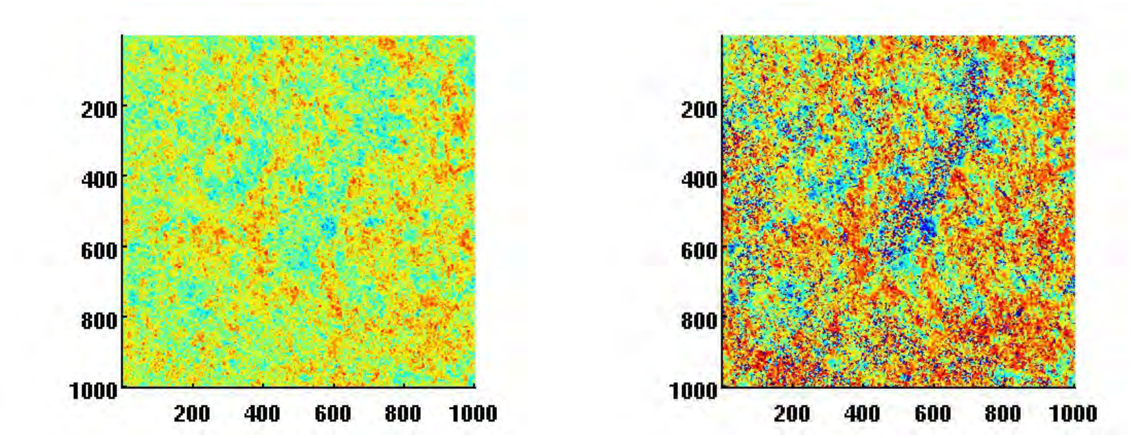

(a) filtered interferometric phase image after applying a 5 × 5 box filter

(b) filtered interfermetric phase image after applying the 5 × 5 spatially adaptive speckle filter

Figure 4.8: Comparing the filtered interferometric phase image between the 5×5 box filter and the spatially adaptive speckle filter . The result shows that the spatially adaptive speckle filter can effectively reduce the speckle noise and preserve the phase information.

4.5 Conclusion

In this chapter, the radar return from forest areas is investigated. We see that the vertical reflectivity profile of forests at L- and P-band is composed of two layers, one located at ground level and the other on the canopy level. The canopy backscatter is a distributed scatterer, which leads to severe speckle noise in the returned signal. The analysis of the statistics of canopy speckle noise conclude that multilook processing is effective to remove the speckle noise. We developed a spatially adaptive filter to reduce the speckle noise as well as preserve the detailed phase information for all interferograms. Using real L-band SAR data, we show that the spatially adaptive filter has better performance as compared to the commonly used box filter.

Chapter 5

Phase Noise in SAR Tomography

In the previous two chapters, we developed the retrieval algorithm, the Capon beamformer, and the spatially adaptive speckle filter for using SAR tomgraphy in forest areas. Theoretically, we prove that the forest vertical structure can be retrieved through SAR tomography. In practice, there are still two noise sources in spaceborne repeat-pass SAR data that will potentially inhibit the tomographic applications in forest areas. These two noise sources are phase noise and temporal decorrelation. In this chapter, we investigate the phase noise and its impact on SAR tomography. First, we explain the different sources of phase noise in spaceborne SAR data, focusing on the dominant one, atmospheric propagation delay. Then, we examine the impact of phase noise on SAR tomography in theory and via simulation. In the last section, we propose a robust algorithm to improve the performance of the Capon beamformer in the presence of phase errors.

5.1 Phase errors in Spaceborne SAR Images

5.1.1 Importance of Accurate Phase Measurement

From Chapter 3, we can see that SAR tomography is based on the analysis of the distance between targets to different SAR sensor locations. The distance measurement in radar technique is obtained through the delay measurement, then converted to distance based on the velocity of microwave propagation in the medium between the sensor and the target. Acquiring accurate phase information is the key to the precise parameter inversion.

5.1.2 Components of Phase Noise

A number of random phase errors are introduced during the phase signal acquisition. The phase noise has been intensively studied in InSAR research [Hooper et al. (2004)] and can be modeled as:

$$\phi_{error} = \phi_{def} + \phi_{atm} + \phi_{orb} + \phi_{\varepsilon} + \phi_{n}, \tag{5.1}$$

where ϕ_{def} represents the phase due to deformation, ϕ_{ε} refers to the error introduced by using imprecise topographic information, ϕ_{orb} refers to the error introduced due to imprecise orbits information in mapping the contributions of Earth ellipsoidal surface, ϕ_{atm} corresponds to the difference in atmospheric propagation times between the two acquisitions used to form the interferogram and ϕ_{n} represents the phase noise due to the scattering background and other noise terms. Among those error sources, the dominant one for spaceborne SAR systems is the atmospheric propagation delay.

5.1.3 Origin of Atmospheric Propagation Delay

The atmospheric propagation delay is the main phase error source for the spaceborne repeat-pass system. It was first observed in interferograms by Goldstein [Goldstein (1995)]. The atmosphere is divided into many different layers, out of which two major layers, troposphere and ionosphere, are responsible for the propagation delay. The propagation delay is mainly due to changes in the refractive index of the medium, as illustrated in Figure 5.1. These changes are caused by dispersive effects in the ionosphere and by air pressure, temperature and water vapor in troposphere.

The lowest part of Earth's atmosphere, from the surface to 20 km altitude, is referred to as the troposphere. It contains 80% of the atmosphere's mass and 99% of the water vapor. It is well known that electromagnetic waves are delayed (slowed down) when they travel through the troposphere. In addition, differences in temperature, pressure, and water

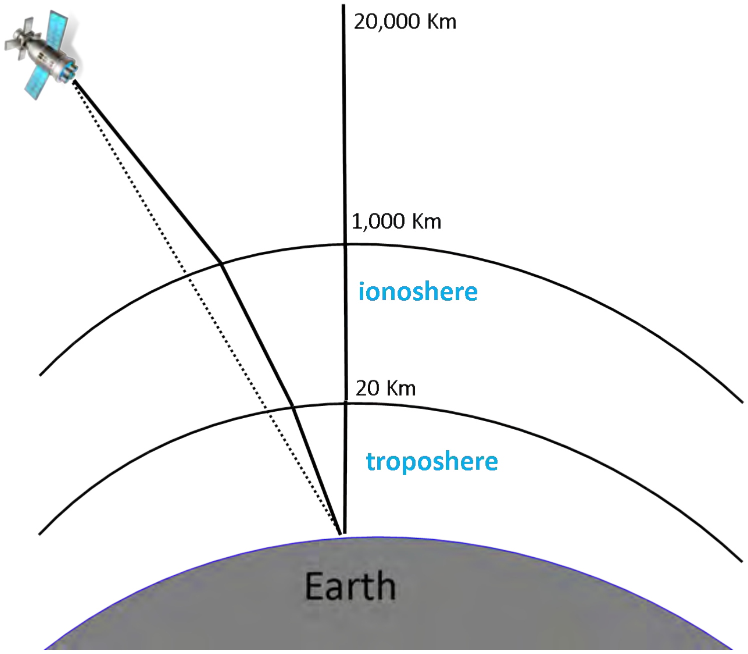

Figure 5.1: Origin of the atmospheric propagation delay

vapor content of the troposphere at the times of SAR acquisitions can result in variations in the refractive index and thus in the phase signals in repeat-pass measurements. Zebker et al. [Zebker et al. (1997)] reported, for example, that spatial and temporal changes of 20% in the relative humidity of the troposphere could lead up to 10 to 14 cm errors in the measured ground deformations and 80 to 290 m errors in derived topographic maps for baselines ranging from 100 m to 400 m in the case of the SIR-C/X-SAR. A number of researchers have concluded that the tropospheric effects are a limiting factor for wide spread applications of repeat-pass InSAR [Rosen et al. (1996); Massonnet and Feigl (1995)].

The ionosphere is the upper part of the atmosphere extending from 50 to 1000 km altitude. Energetic radiation from Sun ionizes molecules in the ionosphere to create a mix of free electrons, ions and gases. Contrary to the effects of the troposphere, the ionosphere tends to accelerate the phases of electromagnetic waves when they travel through the medium. The zenith ionospheric range error is proportional to the total electron content (TEC) in the ionosphere. For example, for C-band SAR, a TEC of $1x10^{16}m^2$ causes a phase shift of about half a cycle [Hanssen (2001)]. The ionosphere is however a dispersive medium affecting the radar signals proportionately to the square of the wavelength [Curlander and McDonough (1991)]. For example, if the ionosphere causes 1.5 m range errors to the C-band (λ= 5.6 cm) signals, it will cause about 24 m range errors to the L-band (λ = 23 cm) signals if the same imaging geometry and atmospheric conditions are assumed.

5.2 Previous Studies on Mitigating Propagation Delays

Numerous previous studies have focused on the quantification and mitigation of propagation delays using various approaches. One way to mitigate the atmospheric phase errors in a time series is to apply filtering techniques, such as temporal plus spatial filters as suggested by Berardino et al. [Berardino et al. (2002)]. The choice of the filter in this approach is subjective, leading to the concern of smoothing out signals over the same time scales as the noise.

Other studies propose more complicated but direct methods for estimating and removing the effects of atmospheric delays. Proposed methods include using GPS data [Onn and Zebker (2006)] and radiometric data to produce zenith path delay difference maps for InSAR atmospheric corrections, for instance using either MODIS (Moderate Resolution Imaging Spectrometer, for the ENVISAT system only) [Li et al. (2005)], or MERIS (Medium Resolution Imaging Spectrometer, for the ENVISAT system only) [Li et al. (2006)]. Other approaches use weather models together with radiometric data to generate an instant water vapor map, such as MERIS with MM5 [Puysségur et al. (2007)], or use a weather model only to predict atmospheric delays [Foster et al. (2006)]. These imagery based or model based approaches may provide estimates of water vapor distribution from independent data sources at the time the SAR image was acquired. However, these approaches have limited applications for older SAR images, since MODIS and MERIS were launched in 1999 and 2002, respectively. Radiometric systems require solar illumination, so they cannot be used to correct for SAR images acquired at night. Some calibration approach is also necessary for the user to accommodate the radiometric data to different study areas. GPS-based approaches are limited by the density and existence of GPS stations in some remote area. Moreover, the efficacy of modeling based approaches is still debated, especially the extent to which they consistently reduce or add noise to interferometric observations.

5.3 The Impact of Phase Errors on Capon Beamforming

Previous research have concluded that the atmospheric disturbance is a limiting factor for wide spread applications of repeat-pass InSAR. In this thesis, we will extend the discussion in repeat-pass SAR tomography.

Though physical origins of phase errors vary, their impacts on the SAR image can be similar in that they both introduce compensated delays of radar echoes as they travel back to the SAR sensor. Let $\mathbf{y}(\mathbf{x},\mathbf{r})$ be the received N dimensional complex data vector collected at (x,r) location, whose elements are $\{y_k(x,r)\}_{n=1}^{N}$. $\mathbf{e}(\mathbf{x},\mathbf{r})$ is the N-dimensional phase disturbance and each element $\{e_k(x,r)\}_{n=1}^{N}$ is modeled as a set of independent random variables. A reasonable choice is $\mathbf{e}(x,r) \sim N(0,\sigma^2\mathbf{I})$, a set of real valued Gaussian variables. Accounting for the phase noise, the observed signal can be written as:

$$\mathbf{y}(x,r) = \mathbf{y_0}(x,r) \odot exp(j\mathbf{e}(x,r)), \tag{5.2}$$

where $\mathbf{y_0}(\mathbf{x},\mathbf{r})$ represents the perfectly calibrated data vector and $\odot$ is the Hadamard product, performing an element by element product. Recall from Chapter 3, the reflectivity profile in elevation and the received signal forms a Fourier pair. It is easy to show the impact of phase errors on the reconstruction as

$$\hat{\gamma}(x,r) = \mathscr{F}(y_n(x,r)exp[je_n(x,r)]). \tag{5.3}$$

From the Equation 5.3, it follows that the microscopical effect of phase errors is to defocus the reconstructed elevation profile due to the convolution with the Fourier transform of $exp\,[je_n]$. The effect of these phase errors is severe in tomographic applications, leading to a strong worsening in the estimation of the vertical profiles which is characterized by a loss of height resolution and inflated sidelobes. To get a flavor of this effect, a simulation is conducted. The baseline is the same as used in Chapter 3. The data received is from a point-like scatter located at zero height, with SNR of 15 dB. The residual path delays are simulated as independent Gaussian random variables with standard deviation $0.25\,\lambda$. The number of looks used in the reconstruction is 16.

We compare the performance of the Fourier based beamformer and Capon beamformer in the presence of phase noise. The obtained profiles shown in dB with respect to the peak power, are in Figure 5.2. It is apparent that the phase errors is almost negligible using the Fourier based method, while they have a more detrimental effect on the Capon beamformer. In Capon beamforming, the resulting profile with phase errors exhibits a much poorer peak sidelobe ratio and a reduced resolution compared with error-free case.

5.4 Robust Capon Beamforming Method

In Chapter 3, we showed the Capon beamformer, based on adaptive selection of the weight vector for minimizing the array output power, has a better resolution and much better interference rejection capability than the traditional Fourier based method. However, in SAR tomographic application, the unavoidable phase errors make the steering vector imprecise, seriously degrading the overall performance of the system.

The interest in increasing robustness against uncertain steering vectors for Capon beamformer has long existed in array signal processing fields [Li and Stoica (2005); Cox et al. (1987); Stoica et al. (2002); Lorenz and Boyd (2005)]. Many approaches have been proposed during the past decades to improve the robustness of the Capon beamformer, including diagonal loading [Li et al. (2003)] and a subspace-based adaptive beamforming method [Burgess and Van Veen (1996)]. However, those suggested methods are rather ad hoc in that the choice of their parameters is not directly related to the uncertainty of the steering vector. In this section, we will adopt a robust algorithm for Capon beamformer which has a firm theoretical basis and is a natural extension of the Capon beamformer to the case of uncertain steering vectors [Li and Stoica (2005)].

5.4.1 Spherical Uncertainty Set

The robust beamforming problem is to extend the Capon beamformer so as to be able to accurately determine the power of signal of interest even when only the imprecise knowledge of its steering vector $\mathbf{a}(\theta)$ is available. More specifically, to account for the array steering vector errors, we assume the real steering vector as $\mathbf{a}_0$, the known steering vector as $\bar{\mathbf{a}}$, then

$$[\mathbf{a}_0 - \bar{\mathbf{a}}]^H \mathbf{C}^{-1} [\mathbf{a}_0 - \bar{\mathbf{a}}] \leq 1 \tag{5.4}$$

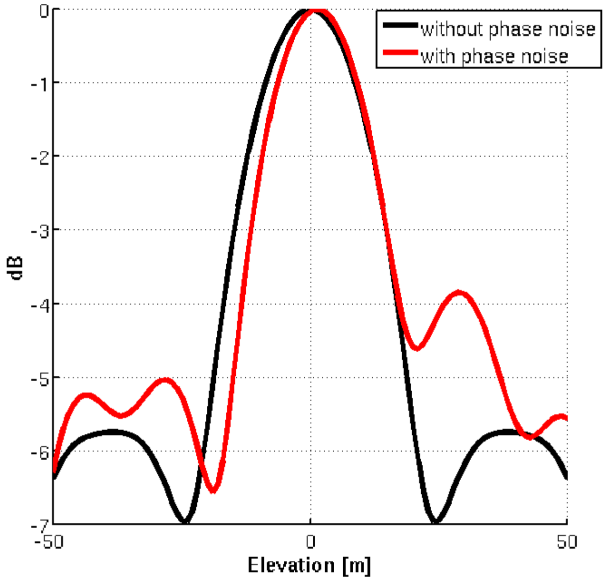

(a) The Fourier based method

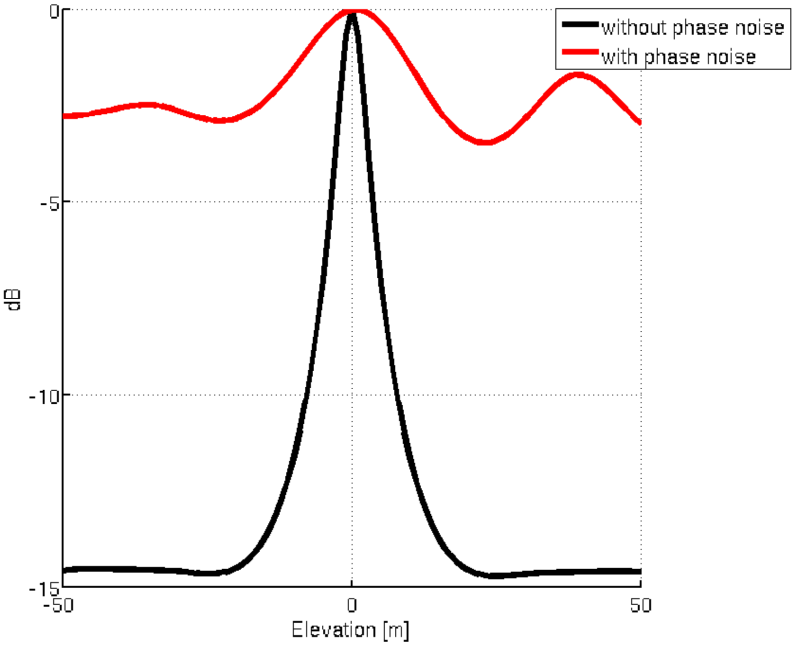

(b) The Capon beamformer

Figure 5.2: Effects of Phase errors in SAR tomography. Black line indicate the error free case while red line shows the reconstruction result in the presence of phase errors. The performance of the Capon beamformer suffers a lot, requiring a more robust version.

where C is a given positive definite matrix. Without loss of generality, consider the spherical constraint situation, where $\mathbf{C} = \varepsilon\mathbf{I}$, then referring to Chapter 3, the Capon beamformer under a spherical constraint would be :

$$\min_{\mathbf{a}} \mathbf{a}^H \mathbf{R}^{-1} \mathbf{a} \qquad subject\ to \, \|\mathbf{a} - \bar{\mathbf{a}}\|^2 \leq \varepsilon. \tag{5.5}$$

To exclude the trivial solution $\mathbf{a} = \mathbf{0}$, we add the constraint:

$$\|\bar{\mathbf{a}}\|^2 > \varepsilon. \tag{5.6}$$

Since the optimal solution will occur on the boundary of the constrain set, we can reformulate as the following quadratic problem with a quadratic equality constraint:

$$\min_{\mathbf{a}} \mathbf{a}^H \mathbf{R}^{-1} \mathbf{a} \qquad subject\ to \, \|\mathbf{a} - \bar{\mathbf{a}}\|^2 = \varepsilon. \tag{5.7}$$

The problem can be solved efficiently by using the Lagrange multiplier approach

$$F(\mathbf{a}, \lambda) = \mathbf{a}^H R^{-1} \mathbf{a} + \lambda \left(||\mathbf{a} - \bar{\mathbf{a}}||^2 - \varepsilon \right) \tag{5.8}$$

where $\lambda \geq 0$ is the Lagrange multiplier. Differentiation of Equation 5.8 with respect to $\mathbf{a}$ gives the optimal solution $\mathbf{a_0}$ as :

$$\mathbf{R}^{-1}\mathbf{a}_0 + \lambda(\mathbf{a}_0 - \bar{\mathbf{a}}) = 0. \tag{5.9}$$

The Lagrange multiplier λ is obtained by the solution of the constraint equation:

$$\left\|(\mathbf{I} + \lambda\mathbf{R})^{-1}\bar{\mathbf{a}}\right\|^2 = \varepsilon. \tag{5.10}$$

5.4.2 Efficient Algorithm for Solving the Optimization Problem

We adopted the approach proposed in [Li et al. (2003)] for solving the above robust Capon beamformer. The steps for computing the optimal beamformer are as follows:

1. Determine the eigen-decomposition of the sample covariance matrix $R = U\Gamma U^H$ and set $b = U^H \bar{a}$

2. Solve the following equation

$$\sum_{l=1}^{L} \frac{|b_l|^2}{(\gamma_l+\lambda)^2} = \varepsilon \tag{5.11}$$

to get the Lagrange multiplier λ, where γ_l is the corresponding eigenvalue for sample covariance matrix R. Using the knowledge that the solution is unique and the function is monotonic, the equation can be solved through Newton's method. Also noting that λ belongs to the interval

$$\frac{\|\bar{\mathbf{a}}\|-\sqrt{\varepsilon}}{\gamma_1\sqrt{\varepsilon}} \leq \lambda \leq \frac{\|\bar{\mathbf{a}}\|-\sqrt{\varepsilon}}{\gamma_L\sqrt{\varepsilon}}. \tag{5.12}$$

3. Calculate an estimate of the unknown steering vector $\mathbf{a}$:

$$\mathbf{a_0} = \bar{\mathbf{a}} - \mathbf{U}(\mathbf{I}+\lambda\Gamma)^{-1}\mathbf{U}^*\bar{\mathbf{a}}. \tag{5.13}$$

4. The estimated power finally yields

$$\sigma_0^2 = \frac{1}{\bar{\mathbf{a}}^*(\lambda^{-2}\mathbf{I}+2\lambda^{-1}\Gamma+\Gamma^2)^{-1}\Gamma\mathbf{U}\mathbf{U}^*\bar{\mathbf{a}}} \tag{5.14}$$

5.4.3 Numerical Simulation

We apply the robust Capon beamformer to the case with random phase errors and compare the results with the conventional Capon beamformer. The simulation parameters are the same with the ones used in Section 5.3. The result is reported in Figure 5.3. The robust Capon beamformer can improve the result, even still not able to recover the noise free situation.

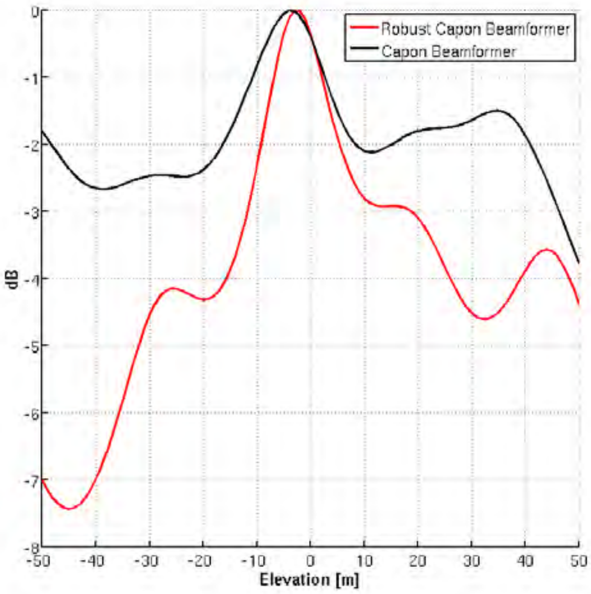

Figure 5.3: Comparison of the robust Capon beamformer and Capon beamformer in the presence of random phase errors. The Robust Capon beamformer can still improve the performance.

5.5 Discussion

Phase noise in spaceborne repeat-pass systems is a hard problem to tackle and will hang over all SAR interferometry applications for a long time. Although a number of methods have been proposed and validated in previous research, each has its pros and cons.

In this chapter, we investigate the impact of phase noise on SAR tomography both in theory and simulation. We notice that the presence of phase noise, the performance of the Capon beamformer is heavily degraded. Thus, we propose to use the robust Capon beamformer for spaceborne SAR tomography and show the improvement in the reconstruction.

Despite the progress already made in the research, further studies are still necessary to develop more effective methods for the mitigation of the atmospheric delays. For future research, a better solution should consider acquiring a number of SAR scenes within short time span, incorporating the information of atmospheric conditions (e.g., cloud conditions) from the external available data (e.g., GPS data, high-resolution meteorological data), and acquire data during dawn or dusk to reduce atmospheric effects.

Chapter 6

Temporal Decorrelation over Forest Areas

Tomographic applications require multiple SAR acquisitions over the same area. In a repeat-pass system, the whole acquisition necessarily spans a long period of time. The time between the acquisitions allows changes in the geometry and dielectric constant of the observed objects to occur. Such changes lead to temporal decorrelation, as described in Section 2.6.5.

Changes in forests originate from physical changes of vegetation and ground properties that occur during the acquisition time span. The physical changes can be anthropogenic or natural. Anthropogenic changes include deforestation, plough and irrigation. Natural changes come from biological growth, wind perturbation and variations in weather conditions. For example, wind perturbs the location and the orientation of scattering elements in the radar resolution cell. Rain and temperature transitions may alter the moisture content and the dielectric properties of the vegetated surface. Those physical changes have different temporal scales. The wind perturbation has a short temporal scale on the order of seconds or minutes, while vegetation growth can only affect a long time period. All these temporal changes will inevitably lead to signal changes, and thus fundamentally inhibit the parameter inversion.

Over a short repeat-pass period (i.e., scale of minutes to a few hours), temporal decorrelation over forests usually may be neglected [Lavalle et al. (2012)] but is significant at longer time scales [Zebker and Villasenor (1992); Hagberg et al. (1995)]. The repeat-pass spaceborne SAR system has a typical repeat cycle between 20-50 days and a SAR image stack can take up to more than one year to collect. Thus, the presence of temporal decorrelation is particularly a crucial issue and causes significant uncertainties in parameter estimates for tomographic applications over a vegetated land surface. In fact, NASA-JPL and ESA have recognized the temporal decorrelation as a major limiting factor for SAR tomography in forest monitoring.

In this chapter, we first empirically analyze temporal decorrelation in forest areas from L-band SAR data, and then investigate the impact of temporal decorrelation on the tomographic inversion through simulations. Remedies are mentioned as a proposal for future systems.

6.1 Observation of Temporal Decorrelation in L-band SAR data

Temporal decorrelation in spaceborne L-band SAR data over forest areas was first observed in Seasat data [Zebker and Villasenor (1992)]. The temporal decorrelation is usually quantified through coherence (see Section 2.6.5) in the SAR community. Generally, temporal decorrelation decreases with time, but the coherence level and the decrease rate vary according to different scatterer properties. Stable scatterers, like rocks and urban structures, show high coherence during repeated acquisitions and decrease slowly over time. In comparison, natural scatterers, especially vegetation and forests, have relatively low coherence and lose their coherence quickly over a short period of time.

To demonstrate this, we present an empirical coherence analysis from a L-band SAR dataset near the Harvard Forest (detailed information in Table 7.3). The dataset incorporates both urban areas and forest areas, making it convenient for comparison. The selected pairs for the coherence analysis are listed:

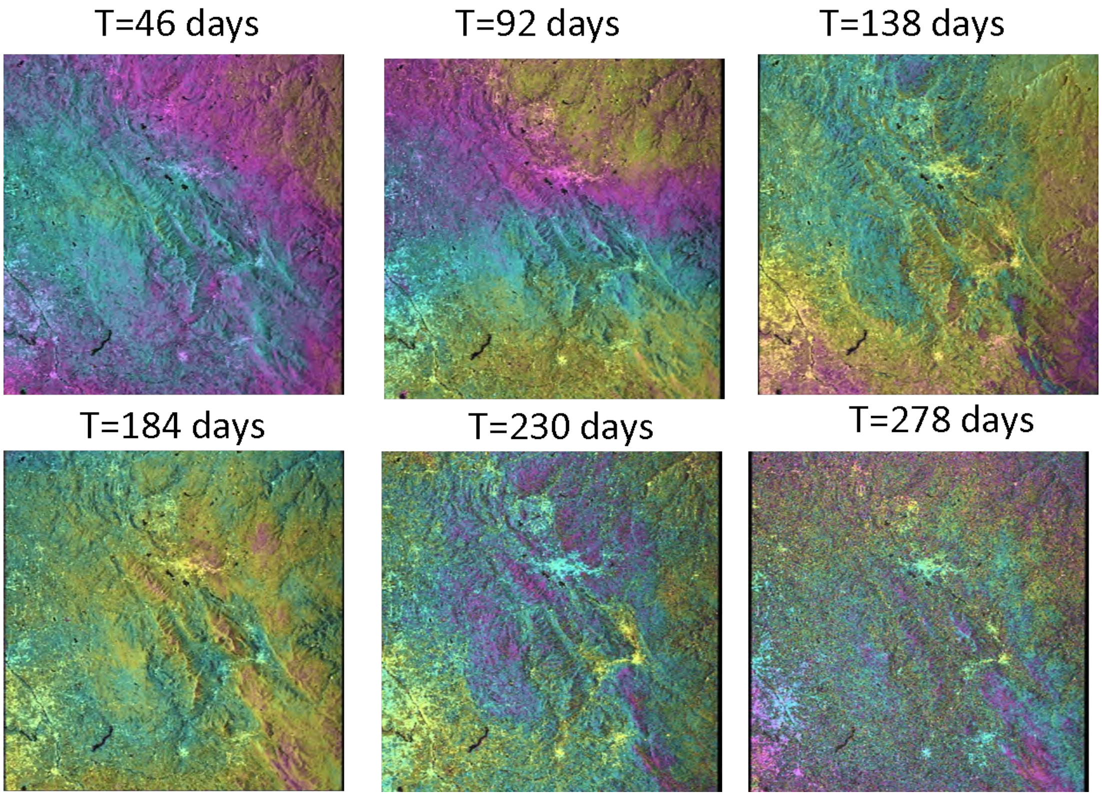

Figure 6.1: Interferograms of SAR images with different temporal baselines. From the interferograms, we can easily notice the drop of coherence as the time interval increases.

Data Pair	Perpendicular Baseline(m)	Temporal Baseline(days)
ALPSRP256740840-263450840	435	46
ALPSRP236610840-250030840	424	92
ALPSRP229900840-250030840	596	138
ALPSRP229900840-256740840	609	184
ALPSRP263450840-229900840	1044	230
ALPSRP270160840-229900840	1844	276

Table 6.1: Selected SAR pairs for the coherence analysis

The interferograms of these pairs are shown in Figure 6.1.

In this dataset, we select one region with dominant urban structures and another with forests for further comparison. The selected areas are marked in Figure 6.2.

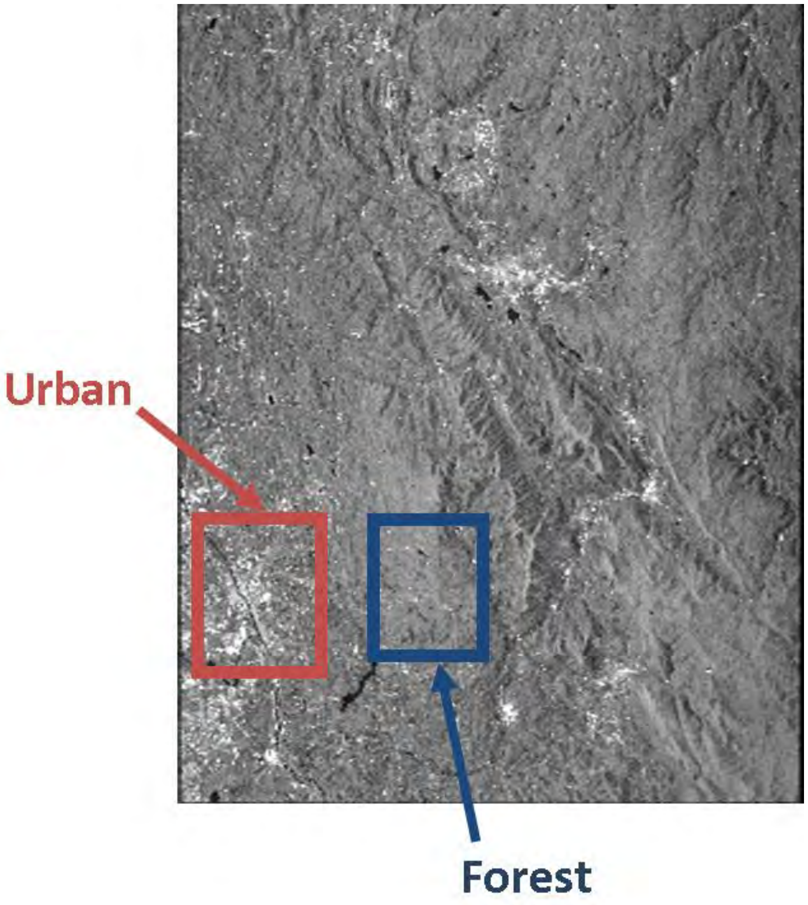

Figure 6.2: Selected urban and forest area from the original SAR image.The red box shows the select urban region while the blue box shows the selected forest region.

The formula for estimating coherence through ensemble averaging has been shown in Section 2.6.3, Equation 2.21. The estimated coherence of urban and forest regions is calculated after taking $L = 4 \times 4$ looks in the azimuth and range directions. Assuming only temporal and geometric decorrelation occur for all the interferograms, the temporal decorrelation can be estimated after removing the geometric decorrelation factor from the coherence. The formula for computing the geometric decorrelation is listed in Section 2.6.3 Equation 2.25.

Figure 6.3 shows the coherence map in the urban region with the increasing temporal baseline. Each pixel of the coherence map is the estimation of the coherence, ranging from 0 to 1. Though the overall coherence decreases with the increasing time interval, scatterers

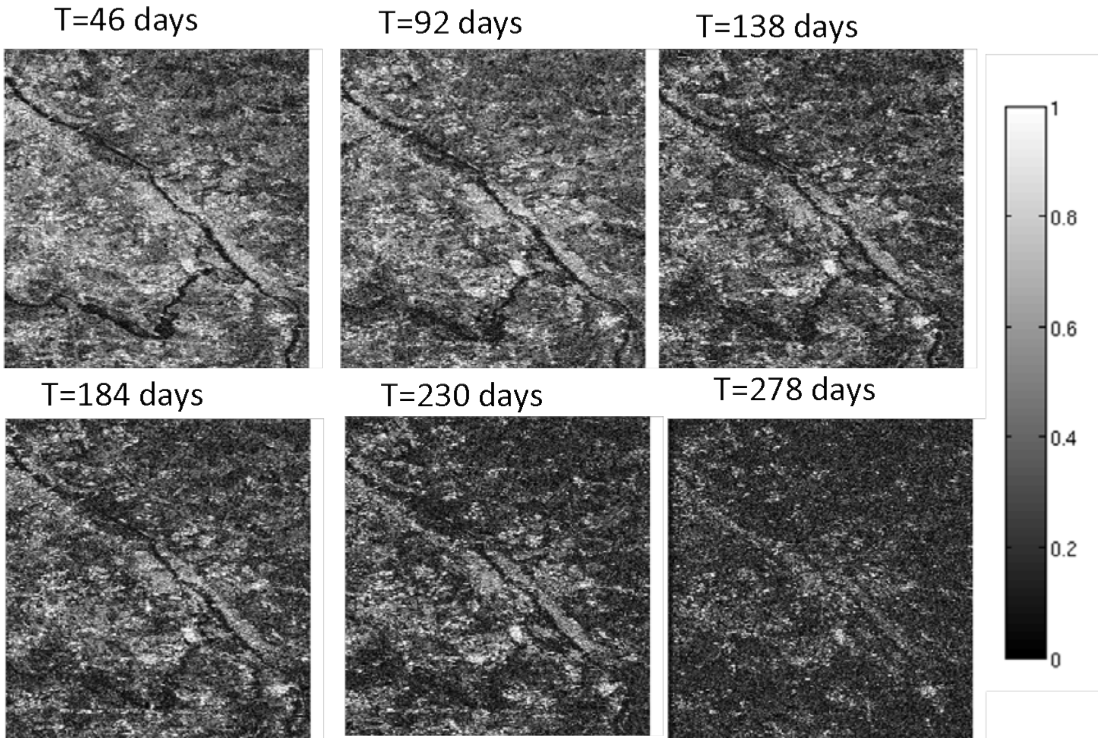

Figure 6.3: Observed coherence in a urban area after 46 days 92 days, 138 days, 184 days, 230 days and 278 days

from the urban region still remain highly correlated. The man-made buildings along the river show quite high coherence level over the whole period.

For the forest area, the coherence map with different time interval is also shown in Figure 6.4. Compared with the urban area, the coherence value with the same time interval is lower. Also, the coherence in forest regions drop quickly after a certain period of time, e.g., the average coherence after 138 days is below 0.3.

We calculate the mean value and the standard deviation of coherence in both regions for further comparison. Figure 6.5 shows the mean coherence and standard deviation with acquisition time. From this figure, the forest area has lower coherence value than the urban area with the same temporal baseline. In the meanwhile, the coherence in the forest area drop quickly. After 138 days, the coherence has already dropped to below 0.3. Forest regions are more susceptible to temporal changes.

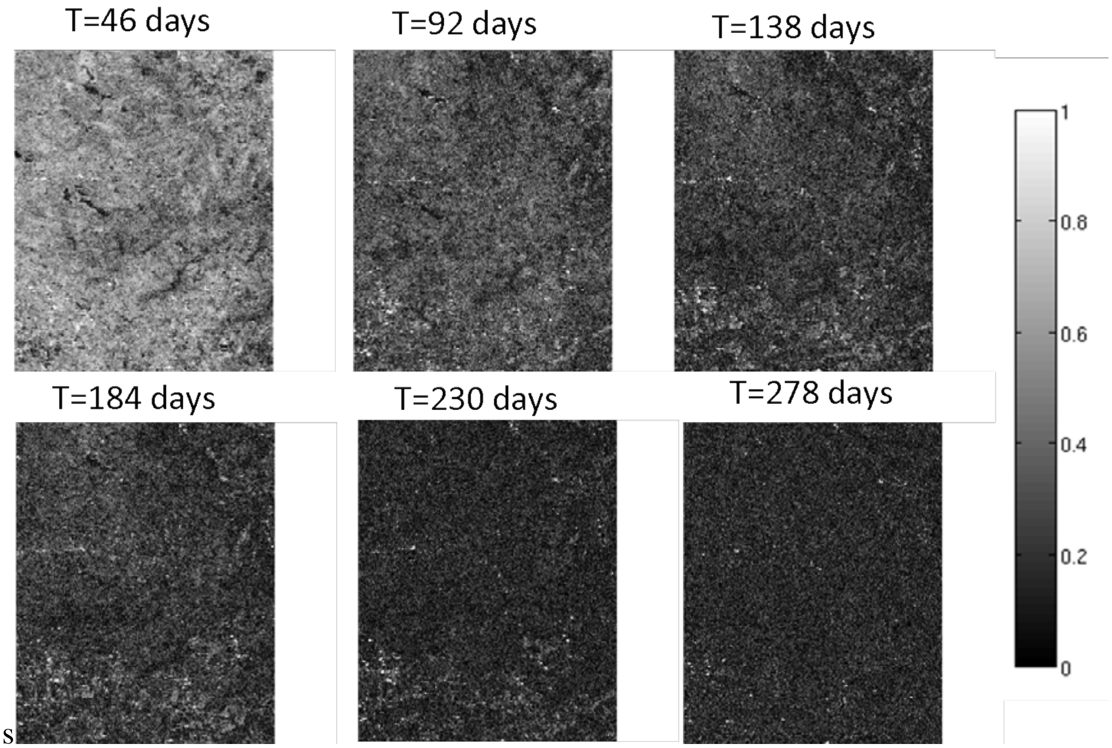

s

Figure 6.4: Observed coherence in a forest area after 46 days 92 days, 138 days, 184 days 230 days and 278 days

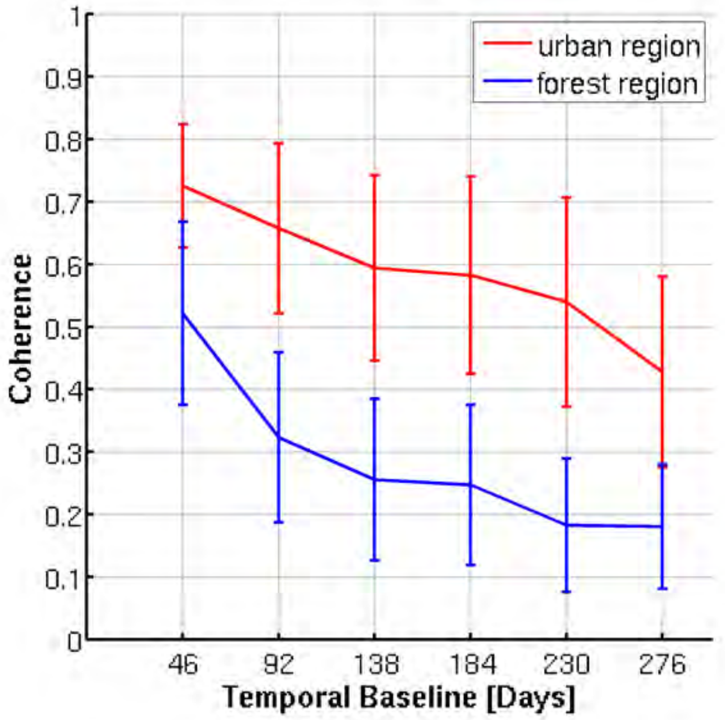

Figure 6.5: The mean and standard deviation of coherence in the urban and forest area

6.2 Impact of Temporal Decorrelation on Tomographic Inversion

We now investigate the impact of temporal decorrelation on SAR tomography through simulation. The baseline-time acquisition pattern used in the simulation is shown Figure 6.6, as the same as was used in Chapter 3. For the sake of generality, the time is normalized to the unit repeat time. One repeat time unit is 46 days.

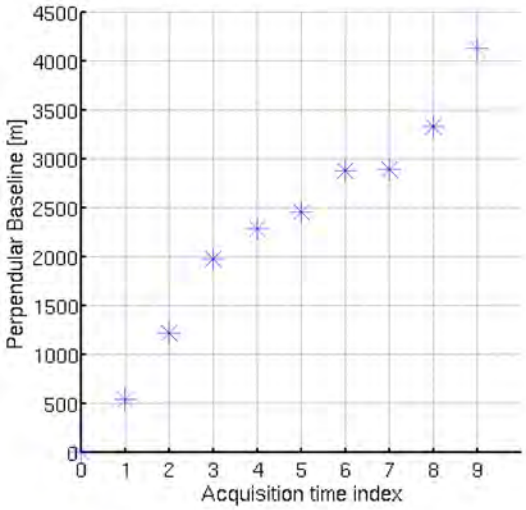

Figure 6.6: Baseline-time acquisition pattern used in the simulation.One repeat time unit is 46 days.

The temporal decorrelation pattern is simulated using an ensemble of 5000 elemental point scatterers with Brownian motion. Different average speeds of Brownian motion can represent different decorrelation patterns. The coherence after each revisit time is calculated as temporal decorrelation. For an L-band system, the different average Brownian motion speed and the corresponding temporal decorrelation pattern is shown in Figure 6.7.

Adding these temporal decorrelation patterns to a scatterer located at 0 meter, the tomographic reconstruction for various temporal decorrelation patterns is shown in Figure 6.8.

From Figure 6.8, we can see that temporal decorrelation has a blurring effect on the tomographic reconstruction. When the decorrelated scatterer is among with other scatterers, the blurring would make the decorrelated signal undetectable. We simulate a typical forest scenario to illustrate the temporal decorrelation effect on the forest tomographic inversion.

In the simulation, a typical forest model with both canopy and ground scatter is concerned. The canopy scatterer is located at height of 30 m, while the ground scatterer is located at 0 m, with its power 1/5 of that from canopy (this is representative for L-band SAR data). We add the Brownian motion with average speed of 0.5 cm/revisit time unit

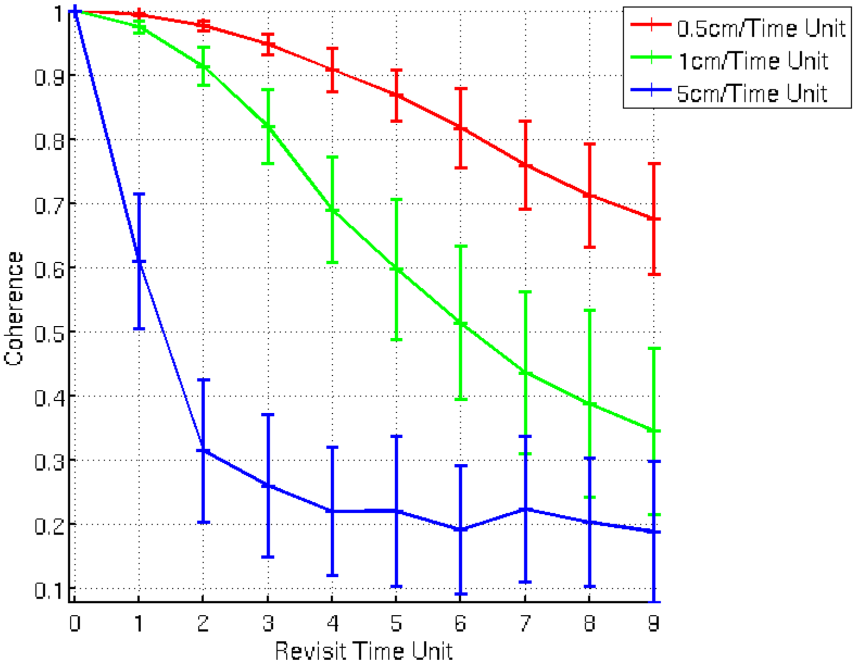

Figure 6.7: Temporal decorrelation with different repeat time lags. The decorrelation is simulated using 5000 elemental point scatterers with the Brownian Motion speed of 0.1cm, 1 cm and 5cm.

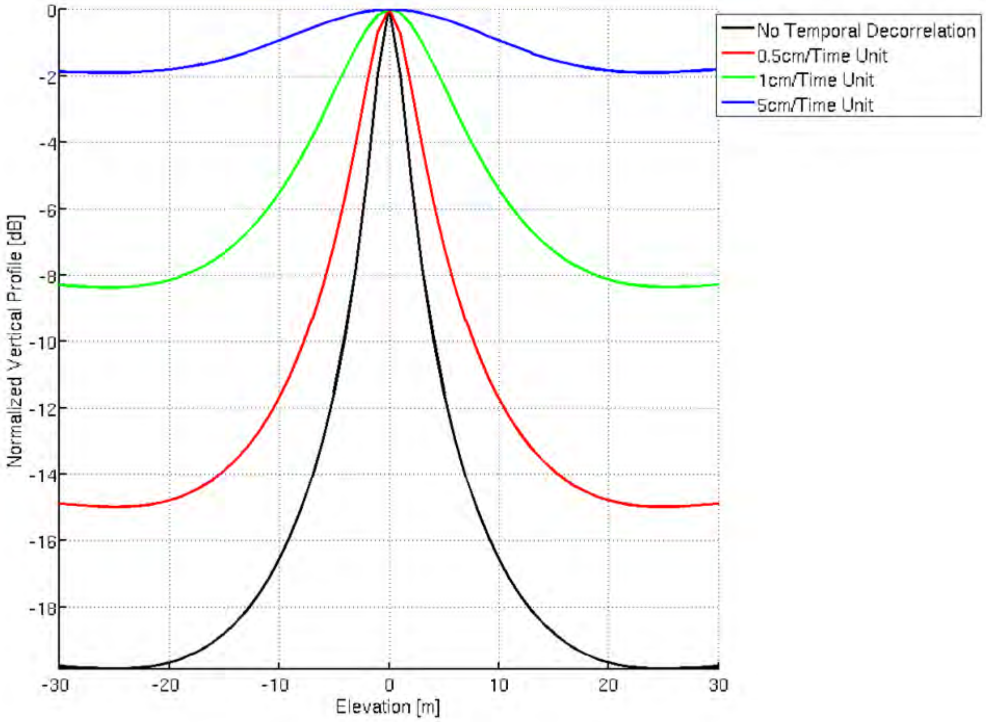

Figure 6.8: Tomographic inversion results for various temporal decorrelation patterns.

to simulate the stable ground scatterer and with average speed of 5 cm/revisit time unit for the canopy scatterer. The calculated coherence of the two temporal decorrelation patterns is showed in Figure 6.7. The number of acquisitions is 10 and the total SNR is 15 dB. The number of independent looks taken for the tomographic processing is 16. The result is the average of 20 Monte Carlo runs.

From Figure 6.9b, in the ideal case of absence of temporal decorrelation, the reconstructed profile includes one dominant peak in the canopy location and another peak in the ground location, corresponding to the canopy scatterer and the ground scatterer. The two scatterers can be visibly separated and the canopy height can be easily measured. However, when the long-term temporal decorrelation of the canopy and ground scatterers is considered, the obtained tomographic profile is shown with blue lines. In this case, the canopy signal suffers from a loss of coherence and is blurred in the reconstruction. Thus, it will potentially lead to a loss of accuracy in the estimation of the forest height.

From the simulation, we conclude that the temporal decorrelation results in a blurred reconstruction and also weakens the canopy backscatter signal. Accuracy in the estimation of canopy height can also be lost with higher temporal decorrelation. This limits the usable time span of multiple SAR images for tomographic applications to ensure sensible results.

6.3 Longer Wavelength to Reduce Canopy Temporal Decorrelation

One way to reduce temporal decorrelation is using lower frequency microwaves. Microwaves are sensitive to objects and movements of a size the same order of its wavelength. Thus, with longer wavelength, small movement will be invisible and the coherence will be improved. Figure 6.10 shows the coherence of the same Brownian movement speed under L-band ($\lambda = 0.23\,m$) and P-band ($\lambda = 0.74\,m$) systems. Compared to L-band, scatterers with the same Brownian motion speed in P-band systems show higher coherence for all the different time intervals. Especially, scatterers with rapid motion speed of 5 cm/revisit time, which is typical for the forest canopy, remain high coherent values in a long time period.

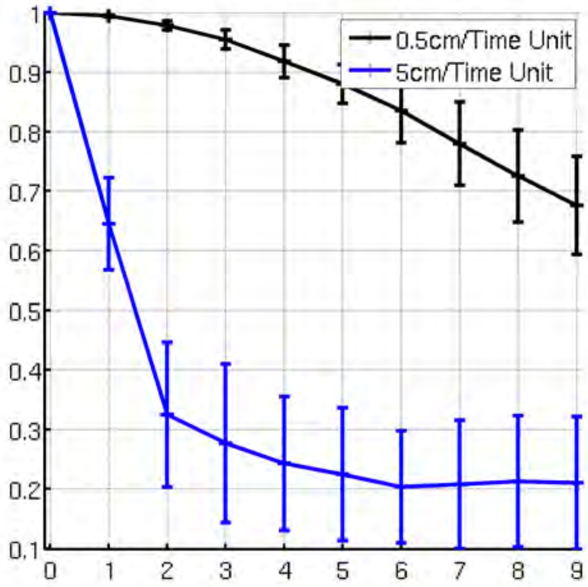

(a) Simulated ground and canopy temporal coherence pattern

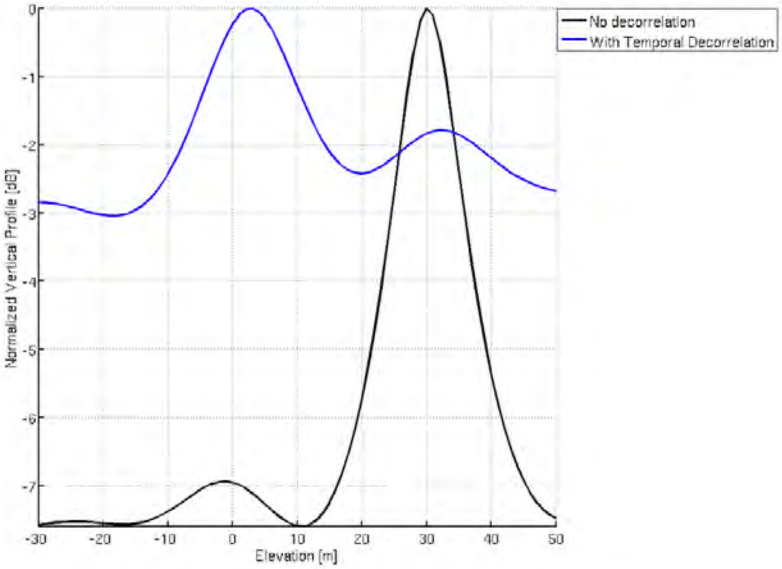

(b) Simulated forest tomographic reconstruction with and without temporal decorrelation.

Figure 6.9: Reconstructed forest elevation profile with and without temporal decorrelation. Without the temporal decorrelation, the dominate scatterer is from the canopy and the height of canopy can be easily inverted. With temporal decorrelation, the canopy scatterer is much weakened compared with the ground scatterer, making the estimation of forest heights much difficult.

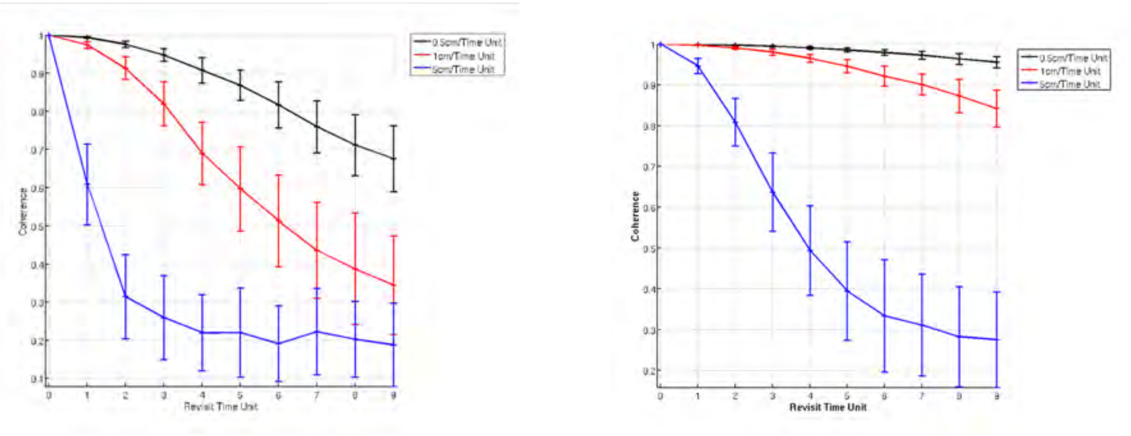

(a) Coherence at L-band

(b) Coherence at P-band

Figure 6.10: Coherence of the same Brownian motion speed in L-band and P-band systems. Scatterers with the same speed show higher coherence in P-band systems.

P-band microwaves can also penetrate the canopy, thus getting the reflection from both the canopy and the ground. For future missions in forest applications, we suggest to use P-band instead of L-band.

6.4 Suggestion for Future Missions

From the above empirical temporal decorrelation analysis from the real L-band SAR data, we conclude that a forest region has quite low temporal coherence and the coherence value drops quickly. As expected, temporal decorrelation will severely degrade the performance of the tomographic inversion. Unfortunately, temporal decorrelation can not be compensated for. In order to successfully apply SAR tomography in forest areas, on the data acquisition level, future SAR missions should aim for both short revisit times and a longer wavelength. In addition, on the data processing level, algorithms which are robust to temporal decorrelation should be considered. The robust Capon beamformer, proposed in Section 5.4, can also help to reduce the impact of temporal decorrelation.

Chapter 7

Case Studies on Real Spaceborne Data

In this chapter, we describe experiments on real spaceborne SAR images of forest areas acquired by ALOS to validate the effectiveness of the proposed tomographic algorithm. We will see that besides its application in forest biomass estimation, SAR tomography, especially with high spatial resolution SAR images acquired from the German TerraSAR-X and the Italian COSMO-SkyMed, is a powerful tool for urban monitoring. In urban areas, obtaining detailed 3D models of individual structure on ground and its deformation with high-resolution has an important advantage in the urban monitoring, security and the management of risk situations. Thus, we also include an urban area to demonstrate the potential of our tomographic technique.

In this chapter, we first briefly introduce the characteristics of the ALOS SAR sensor used in this study, and then analyze two SAR datasets used for the urban and forest areas respectively. The corresponding reconstruction results and further discussion are also reported.

7.1 ALOS Spaceborne SAR

The Advanced Land Observing Satellite (ALOS) is Japan's Earth observation satellite, developed by Japan Aerospace Exploration Agency (JAXA) [Rosenqvist et al. (2004, 2007)]. Since its launch in January 24th, 2006, ALOS has contributed to the fields of mapping, precise regional land coverage observation, disaster monitoring and resource surveying.

Figure 7.1: Artist's view of the deployed ALOS spacecraft in orbit, ALOS launched by JAXA in 2006, stopped working in 2011.

ALOS has three sensors: the Panchromatic Remote-sensing Instrument for Stereo Mapping (PRISM), which comprises of three sets of optical systems to measure precise land elevation; the Advanced Visible and Near Infrared Radiometer type 2 (AVNIR-2), which observes what covers land surfaces; and the Phased Array type L-band Synthetic Aperture Radar (PALSAR), which enables day-and-night and all-weather land observation. PALSAR is a fully polarimetric instrument, operating in fine-beam mode with single polarisation (HH or VV), dual polarisation (HH+HV, or VV+VH), or full polarimetry (HH+HV+VH+VV). It also features a wide-swath ScanSAR mode, with single polarisation (HH or VV). The center frequency is 1270 Mhz (23.6 cm), with a 28 MHz bandwidth in fine beam single polarisation mode, and 14 MHz in the dual-, quad-pol and ScanSAR modes. The off-nadir angle is variable between 9.9° and 50.8° (at mid-swath), corresponding to a 7.9 - 60.0° incidence angle range. In 5-beam ScanSAR mode, the incidence angle range varies from 18.0° to 43.0°. The characteristics of the PALSAR instrument are given in Table 7.1.

7.2 Data Processing Pipeline

The tomographic processing pipeline used in our case study is summarized in Figure 7.2. The detailed processing steps is listed as follows:

Parameter Name	Value
Orbit Direction	Ascending
Altitude	706 km
Radar wavelength	23.61 cm
PRF	1915.709 Hz
Incidence Angle	24.0
Swath Width	12.44 km
Azimuth Resolution	4.45 m
Range Resolution	9.52 m
Temporal Baseline	46 days

Table 7.1: Characteristics of ALOS PALSAR sensor

- SAR images acquired at different baseline locations are focused and co-registered to a common grid.
- The covariance matrix for each pixel is computed through generating the interferograms of each pair and power images of each SLC.
- Phases of all interferograms is flattened to remove topography contribution and then a low pass spacial filter is applied to the flattened phases to remove atmospheric phase noise.
- For forest regions, the spatially adaptive speckle filter is applied to remove the speckle.
- The Capon beamformer is applied to get the tomographic inversion results.

Since the reconstruction is in the elevation direction (perpendicular to the slant-range azimuth plane), the final result needs to be converted to the vertical height direction. The conversion from the elevation s to the height direction can be easily done through geometry:

$$h = s \cdot sin\theta \tag{7.1}$$

where θ is the SAR looking angle.

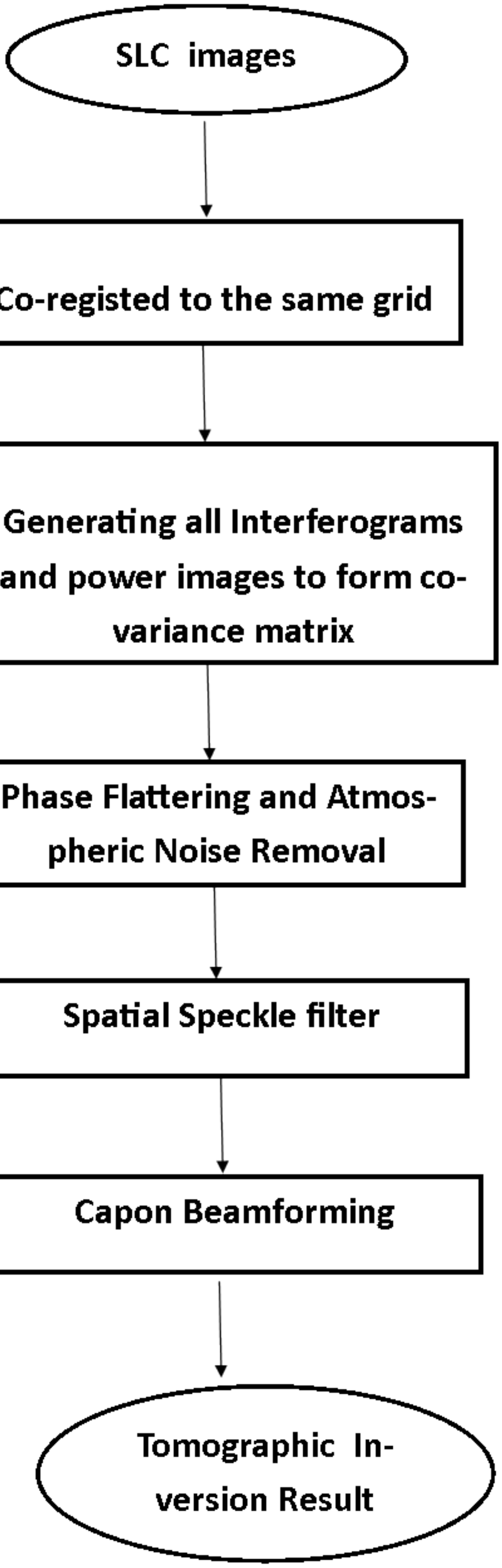

Figure 7.2: Pipeline of SAR tomography

File Name	Acquisition Date	Perpendicular (m)	Temporal Baseline (days)
ALPSRP147650740	2008-11-01	0	0
ALPSRP167780740	2009-03-19	604	138
ALPSRP181200740	2009-06-19	1419	230
ALPSRP187910740	2009-08-04	1002	276
ALPSRP208040740	2009-12-20	2334	414
ALPSRP221460740	2010-03-22	3255	505
ALPSRP228170740	2010-05-07	3410	551
ALPSRP234880740	2010-06-22	3458	597

Table 7.2: The San Francisco Bay Area ALOS dataset

7.3 Case Study in Urban Regions

In the first case study, we investigate tomographic 3D results in an urban area. The SAR data is acquired by ALOS in the San Francisco Bay area. The dataset consists of 8 images in HH mode, spanning a temporal interval of nearly two years. The Google Map image and the SAR image are shown in Figure 7.3.

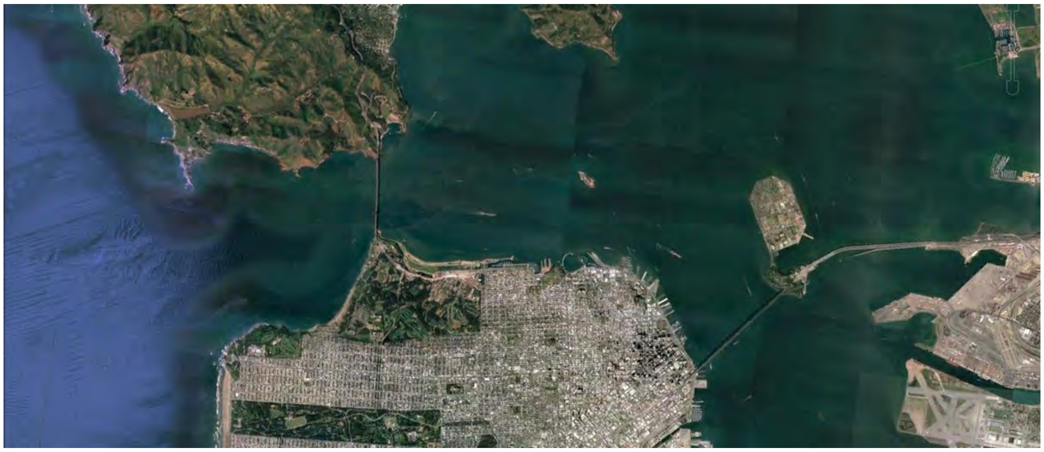

(a) Google Map image

(b) ALOS SAR Image

Figure 7.3: The Google Map image and SAR image of the San Francisco Bay Area

We select the Golden Gate Bridge from the whole image for the study, as shown in Figure 7.4a. The Golden Gate Bridge is tall enough for scatterers from the towers and bridge body to separate in range distance. The two long range line we see in the SAR image is the projection of the bridge towers into the range-azimuth plane.

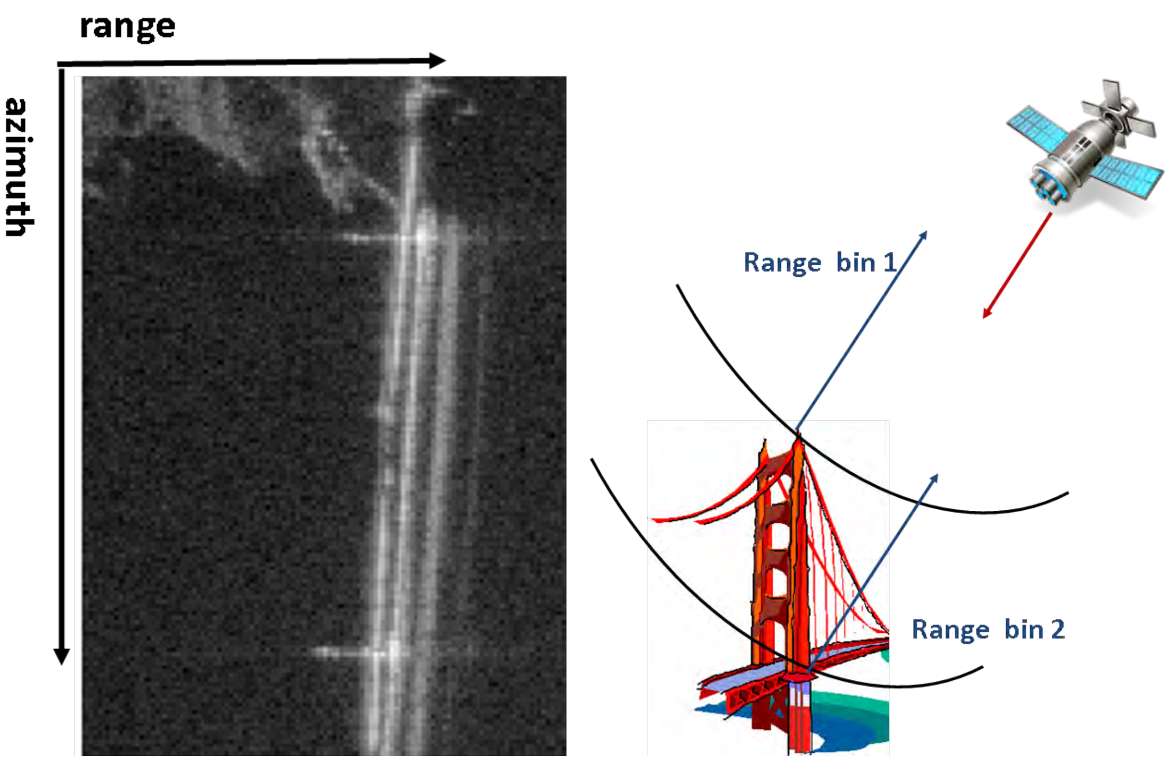

(a) SAR image of Golden Gate Bridge. The two horizontal bins on the bridge is the projection of the tower.

(b) The tower is tall enough to generate radar returns in different range locations.

Figure 7.4: The SAR image of the Golden Gate Bridge. The bridge tower is tall enough to separate the scatters of the same elevation to different range location, resulting two range bins in the SAR image.

In the SAR image, the Golden Gate Bridge is seen as threefold, each at a different phase and time delay due to multiple signal paths to the bridge. Figure 7.5 shows three principle ray paths that give rise to the observed multiple bridges. The shortest path, which appears at the smallest slant range is the direct path from antenna to bridge to antenna. The longest path corresponds to the wave traveling from the antenna to the water, reflecting off the water to the underside of the bridge, and then returning to the antenna by way of the water again. This echo is seen to be much brighter than the direct path. The third bridge image, intermediate in rage compared to the first two, results from rays that travel from antenna to bridge to water to antenna and simultaneously, the reverse of this path. Each has the same path length thus appear at the same point in the image.

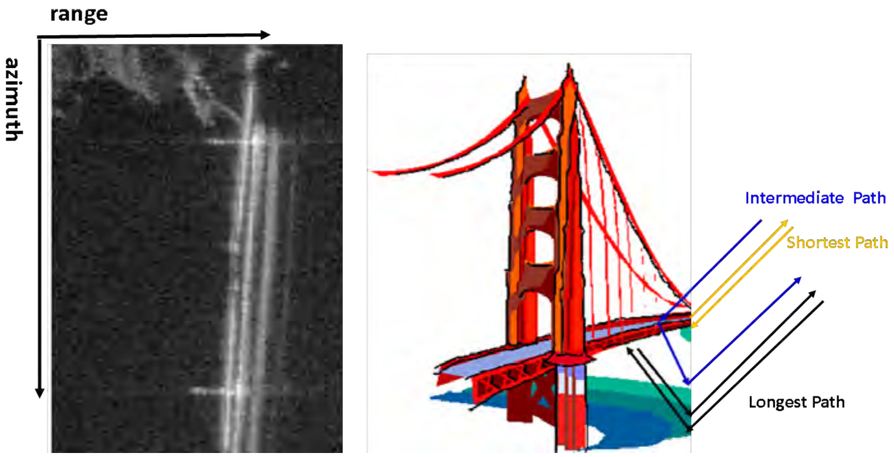

Figure 7.5: Ray paths leading to the observed triplicated Golden Gate Bridge in the SAR image.

For the tomographic reconstruction purpose, we sum up the pixels of the same azimuth position (roughly the same bridge location) to simulate the layover situation and reconstruct the elevation profile of the summed pixels. The reconstructed result is shown in Figure 7.6.

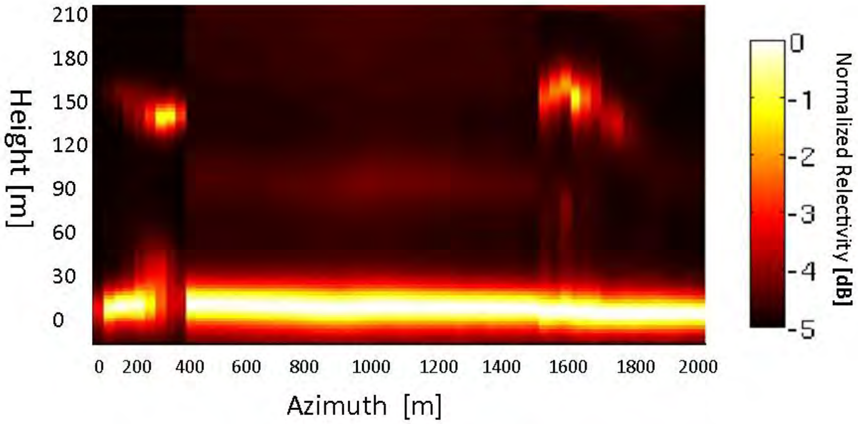

Figure 7.6: Tomographic profile of the Golden Gate Bridge

The two towers can be visibly seen from the reconstructed result. The center height of the tower scatter to the bridge is about 120*m* in height. The reported maximum height of tower to bridge is $152\,m^1$. Hence the reconstructed result is fairly close with the actual height.

In a further demonstration, we select an urban area profile with dense buildings. There are typically two main scatterers for buildings, one from roof and the other from double bounce between ground and wall. Thus, the tomographic reconstruction in Figure 7.8 shows two groups of sparse scatterers, one group located at low elevation representing the double bounce reflector between ground and wall, and the other located at high elevation representing the roof reflectors.

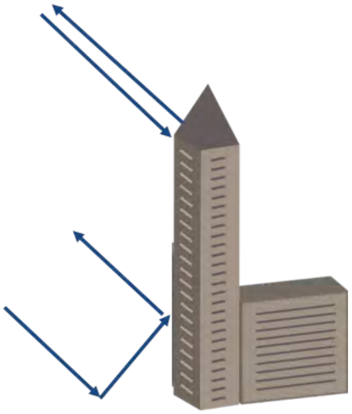

Figure 7.7: Two scatterers for buildings. One is directly from the roof top and the other is from the double bounce between ground and the building wall.

---

[1] The data is quoted from http://goldengatebridge.org/research/factsGGBDesign.php

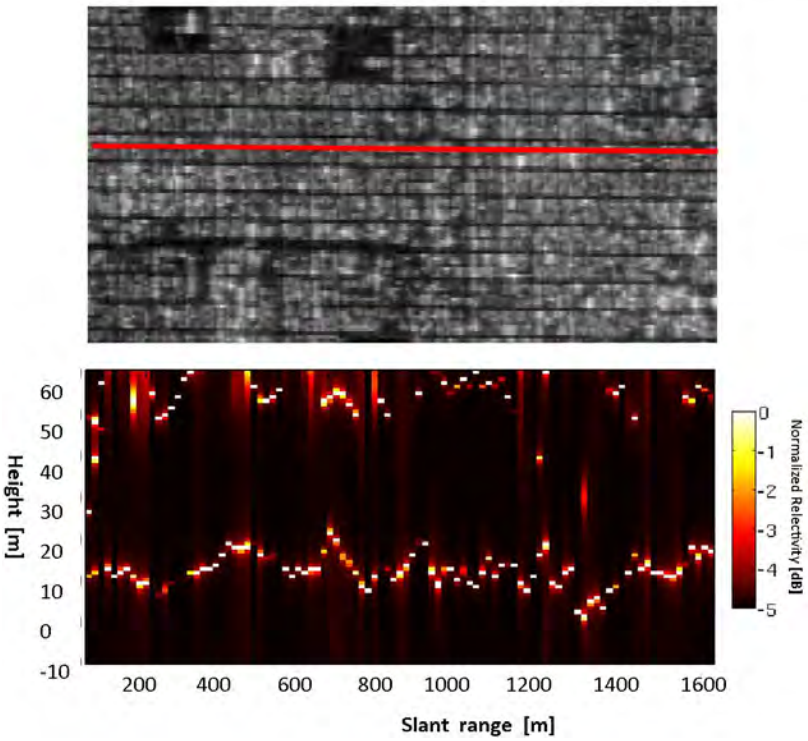

Figure 7.8: The reconstructed tomographic profile in the urban area with dense buildings.The red line indicates the test slice used for the experiment. From the reconstruction, we can see the two groups of sparse scatterers, one representing the roof reflectors and the other presenting the ground-wall double bounce reflectors.

7.4 Case Study in Forest Regions

Now, in this section, we show the tomographic analysis results for Harvard Forest, Massachusetts[2]. The dataset consists of $N = 10$ L-band SAR images, listed in Table 7.3.

Figure 7.9 shows an optical view of the forest from the Google Earth along with an L band SAR image of selected region from this dataset.

---

[2] http://harvardforest.fas.harvard.edu/

File Name	Acquisition Date	Perpendicular (m)	Temporal Baseline (days)
ALPSRP189640840	2009-08-16	0	0
ALPSRP196350840	2009-10-01	538	46
ALPSRP209770840	2010-01-01	1217	138
ALPSRP223190840	2010-04-03	1977	229
ALPSRP229900840	2010-05-19	2282	275
ALPSRP236610840	2010-07-04	2454	321
ALPSRP250030840	2010-10-04	2878	413
ALPSRP256740840	2010-11-19	2891	495
ALPSRP263450840	2011-01-04	3326	505
ALPSRP270160840	2011-02-19	4126	551

Table 7.3: Harvard Forest Area ALOS Data Set

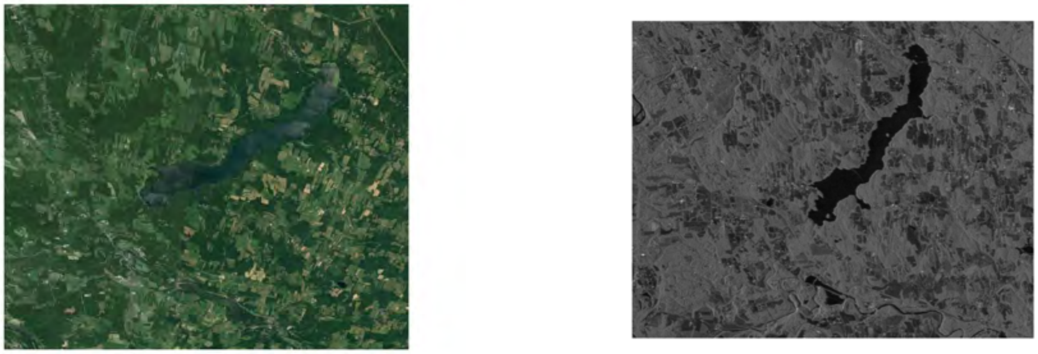

(a) Google Earth Image of the selection region in Harvard Forest

(b) SAR Image of the selection region in Harvard Forest

Figure 7.9: The Google Earth optical image and SAR image of the selection region in Harvard Forest.

After the tomographic processing, we convert the multibaseline images from different obits to a set of multilayer images. Each layer indicates the backscattered power in one height location.

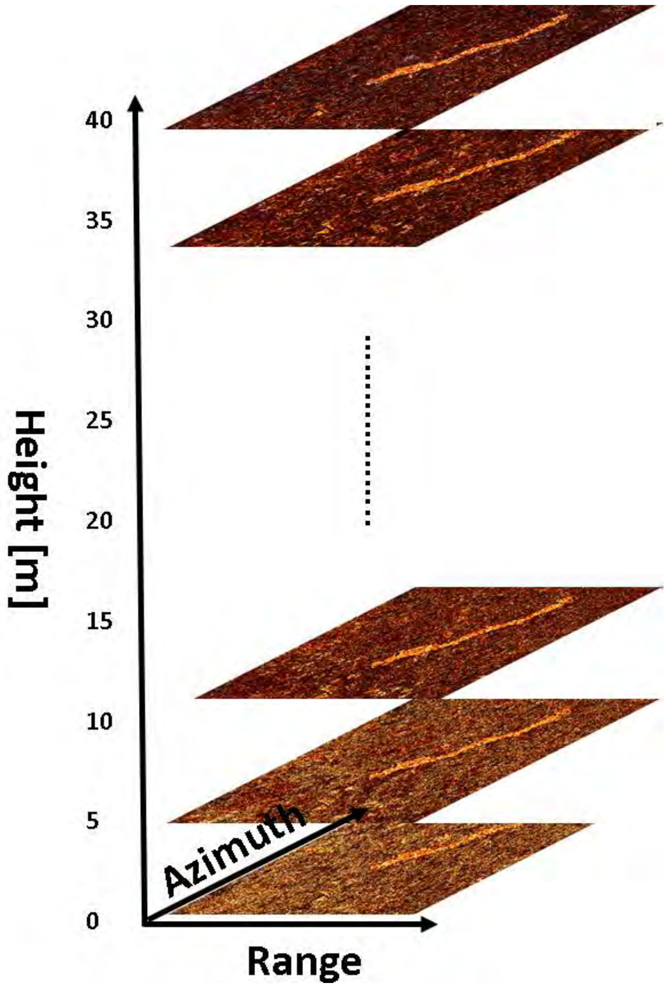

Figure 7.10: Multilayer Image. Each layer indicates the backscattered power in one height location.

Figure 7.11 shows the reconstructed reflectivity at different height locations. From this analysis, we find most of the reflection is from the ground level, and as the height increases, the general reflection level decreases.

Another way to view the vertical structure is to take a slice of the multi-layer data stack corresponding to a constant ground range or azimuth value. Here we display a slice of pixels at one azimuth position in the selected region, as shown in Figure 7.12. The slice chosen contains both dense forests and less vegetated ground. Thus it can used to show the tomographic performance in different types of vegetation.

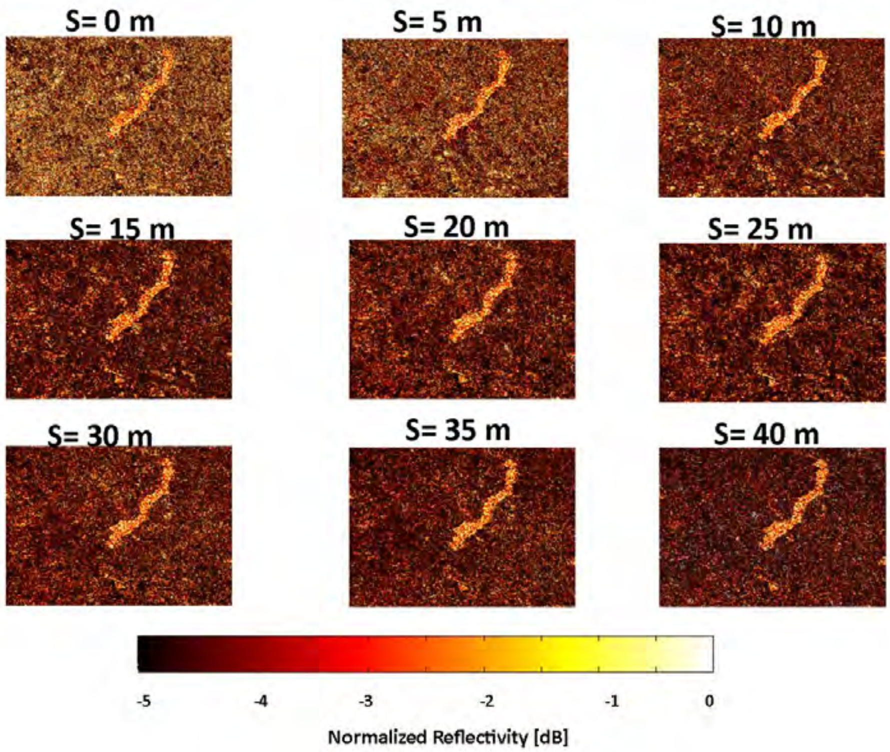

Figure 7.11: Normalized reflectivity for 9 tomographic layers associated with 9 different height locations: 0 m (ground layer), 5 m, 10m,15m, 20m, 25m, 30m, 35m and 40m.

Figure 7.12 shows the tomographic result corresponding to the solid line shown in the above optical image. The tomographic result is in general agreement with the scatterer distribution. In the densely forested region, since L-band microwaves are capable of penetrating the canopy, we can see the scattering from the canopy height and the ground level. In the less vegetated ground, the main scattering is largely centered near the ground level with little deviation caused by vegetation decorrelation.

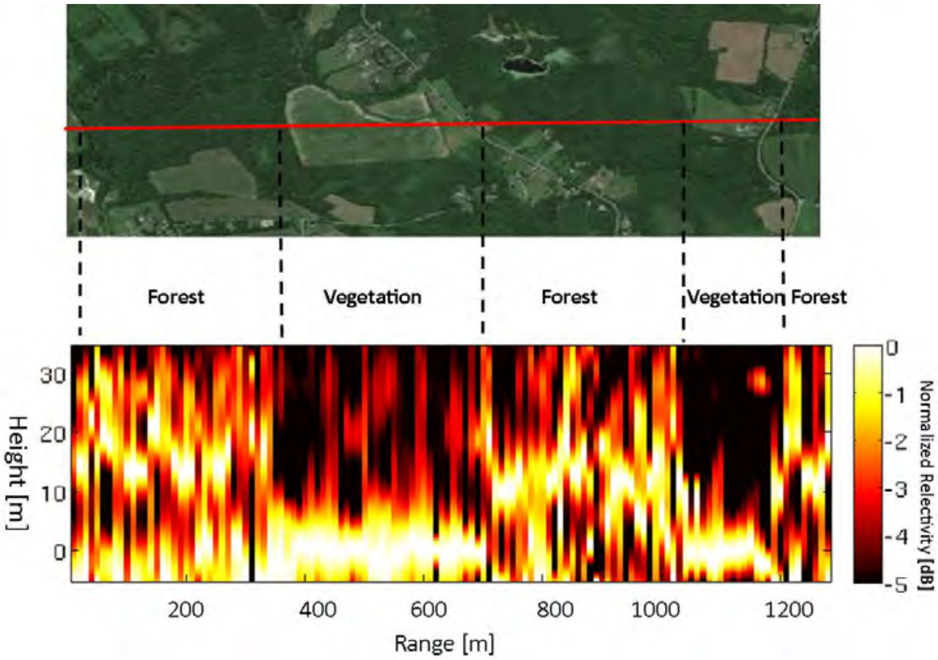

Figure 7.12: An example of the tomographic slice. The red line indicates the test slice used in the experimental. The intensity is normalized and displayed in dB so that the main scattering contribution can be distinguished easily.

The statistics of the estimated canopy height in the selected forest part are

$$h = 24.0299\,m, \Delta h = 9.1683\,m. \tag{7.2}$$

Once again, the reconstructed forest heights are a rough agreement with previous UAVSAR and Lidar measurements [Hensley et al. (2012)], which both estimate the canopy heights in this area between 15-30 m.

7.5 Discussion

In the above experiments, we saw that spaceborne SAR tomography at L-band can achieve satisfactory results in urban areas, where the scatterers are highly coherent during the acquisition time span. For forest areas, the L-band microwaves penetrate the canopy, resulting in both reflections from the canopy and ground. However, for L-band systems, the major scatter contribution is still from the canopy layer. Thus, SAR tomography is capable of estimating forest heights, leading to reasonable estimation of the biomass stored in forest regions. The loss of coherence due to distributed scatterers in canopy layer can be compensated through the spatially adaptive speckle filter. Though temporal decorrelation can still make the reconstruction blurred, the overall result is still acceptable for many uses.

Chapter 8

Summary and Future Work

8.1 Summary

In this thesis, we have validated that multi-baseline SAR tomography, which utilizes multiple SAR images acquired at different baseline locations to reconstruct the elevation dimension, can be used to retrieve forest heights. Compared to other methods, SAR tomography is nonparametric, easy to implement and is able to reconstruct the forest vertical structure. With a large amount of SAR images available in the near future, SAR tomography shows great potential in measuring global forest biomass.

The thesis covers the whole cycle of developing spaceborne SAR tomography for forest height estimation, from the problem formation phase to testing on real SAR data. Through this work, we have accomplished the following:

- Establishing the theory for SAR tomography. Through detailed mathematical signal modeling, we find that the received radar signal at different baseline locations and elevation scatter profile form a Fourier pair. This relationship establishes the theoretical foundation for our reconstruction algorithm.
- Applying the Capon beamforming method to improve the tomographic inversion results. For repeat pass spaceborne SAR tomography, the SAR images are limited in number and baseline locations are randomly distributed. Using the Fourier based

reconstruction method, the limited and unevenly distributed acquisitions would fundamentally constrain the resolution for SAR tomography. To overcome the resolution limitation and suppress sidelobes, we proposed to apply super-resolution beamforming methods. Among numerous super-resolution methods, we chose the Capon beamformer for its easy implementation. Through simulation, we have compared the Capon beamformer with the traditional Fourier based method and quantitatively shown its improvement in resolution and sidelobe suppression.

- Investigating the radar signature from forest areas in SAR images. For L- and P-band SAR, we identified the typical scattering mechanisms in forest areas and concluded that the forest vertical structure consist of two layers of scatterers, located in the canopy and at the ground level. Canopy scatter is distributed scatterers and consequently, the speckle noise associated with distributed canopy scatter will limit the inversion result. Thus, we propose a spatially adaptive speckle filter to reduce the speckle noise and preserve the detailed phase information.

- Investigating phase errors and their impact on SAR tomographic inversion. Phase errors, dominated by the atmospheric disturbances, are the main obstacle in repeat-pass spaceborne SAR tomography applications. First, we have modeled the phase errors and showed the corrupting effect on the Fourier spectrum. A simulation on both the Fourier based method and the Capon beamformer has shown the same effect: blurring the reconstructed spectrum. From the simulation, we see that Capon beamforming is quite sensitive to phase errors. Thus we proposed to use a robust Capon beamforming method and showed its improved performance in the presence of phase errors.

- Investigating temporal decorrelation and its effect on SAR tomographic inversion. In repeat-pass systems, long time intervals between acquisitions will allow physical changes to happen, especially in the forest region. In an empirical study on L-band SAR data, we calculated the temporal decorrelation and showed that the coherence in forest areas is low and drops quickly over time. We also investigated the impact of temporal decorrelation on tomographic inversion results, proving that temporal decorrelation would be the limiting factor for many forest applications. Thus for future forest missions, we suggest to shorten the repeat time and use P-band instead of L-band.

- Experimenting with real spaceborne L-band SAR data to test the algorithm proposed and validating the capability of SAR tomography for both urban and forest scenarios. We tested the proposed tomographic inversion algorithm in the San Francisco Bay Area as a urban example and Harvard Forest as a forest example. For urban areas, through SAR tomography, discrete scatterers can be separated and located at the corresponding height location. In forest areas, SAR tomography can also separate the canopy and the ground, giving a satisfactory estimate of canopy height.

8.2 Future Work

In this thesis, we have identified two major obstacles when applying spaceborne SAR tomography in forest regions. The two factors limiting its performance are :

- Atmospheric phase disturbances
- Temporal decorrelation

These two problems can not be easily compensated for through data processing methods. Thus, our recommendations for future SAR systems are:

1. reduce the time interval of repeat pass acquisitions,
2. use lower frequencies for forest areas, like P-band,
3. acquire data during dawn or dusk to reduce atmospheric effects.

In SAR processing, advanced processing strategies, such as persistent scatterers, adaptive phase noise filters and data fusion with other sensors, might also be investigated for further development in this field.

Bibliography

E. Aguilera, M. Nannini, and A. Reigber, “Wavelet-based compressed sensing for sar tomography of forested areas,” *IEEE Transactions on Geoscience and Remote Sensing*, vol. 51, no. 12, pp. 5283–5295, 2013.

R. Bamler and P. Hartl, “Synthetic aperture radar interferometry,” *Inverse problems*, vol. 14, no. 4, p. R1, 1998.

A. Beaudoin, T. Le Toan, S. Goze, E. Nezry, A. Lopes, E. Mougin, C. Hsu, H. Han, J. Kong, and R. Shin, “Retrieval of forest biomass from sar data,” *International Journal of Remote Sensing*, vol. 15, no. 14, pp. 2777–2796, 1994.

P. Berardino, G. Fornaro, R. Lanari, and E. Sansosti, “A new algorithm for surface deformation monitoring based on small baseline differential sar interferograms,” *IEEE Transactions on Geoscience and Remote Sensing*, vol. 40, no. 11, pp. 2375–2383, 2002.

D. E. Bunker, F. DeClerck, J. C. Bradford, R. K. Colwell, I. Perfecto, O. L. Phillips, M. Sankaran, and S. Naeem, “Species loss and aboveground carbon storage in a tropical forest,” *Science*, vol. 310, no. 5750, pp. 1029–1031, 2005.

K. A. Burgess and B. D. Van Veen, “Subspace-based adaptive generalized likelihood ratio detection,” *IEEE Transactions on Signal Processing*, vol. 44, no. 4, pp. 912–927, 1996.

J. Capon, “High-resolution frequency-wavenumber spectrum analysis,” *Proceedings of the IEEE*, vol. 57, no. 8, pp. 1408–1418, 1969.

S. R. Cloude and K. P. Papathanassiou, “Polarimetric sar interferometry,” *IEEE Transactions on Geoscience and Remote Sensing*, vol. 36, no. 5, pp. 1551–1565, 1998.

S. Cloude and K. Papathanassiou, “Three-stage inversion process for polarimetric sar interferometry,” *IEE Proceedings-Radar, Sonar and Navigation*, vol. 150, no. 3, pp. 125–134, 2003.

C. Colesanti, A. Ferretti, F. Novali, C. Prati, and F. Rocca, “Sar monitoring of progressive and seasonal ground deformation using the permanent scatterers technique,” *IEEE Transactions on Geoscience and Remote Sensing*, vol. 41, no. 7, pp. 1685–1701, 2003.

H. Cox, R. Zeskind, and M. Owen, “Robust adaptive beamforming,” *IEEE Transactions on Acoustics, Speech, and Signal Processing*, vol. 35, no. 10, pp. 1365–1376, 1987.

J. C. Curlander and R. N. McDonough, *Synthetic aperture radar*. John Wiley & Sons New York, NY, USA, 1991.

M. C. Dobson, F. T. Ulaby, T. LeToan, A. Beaudoin, E. S. Kasischke, and N. Christensen, “Dependence of radar backscatter on coniferous forest biomass,” *IEEE Transactions on Geoscience and Remote Sensing*, vol. 30, no. 2, pp. 412–415, 1992.

P. Falkowski, R. Scholes, E. Boyle, J. Canadell, D. Canfield, J. Elser, N. Gruber, K. Hibbard, P. Högberg, S. Linder *et al.*, “The global carbon cycle: a test of our knowledge of earth as a system,” *science*, vol. 290, no. 5490, pp. 291–296, 2000.

A. Ferretti, C. Prati, and F. Rocca, “Nonlinear subsidence rate estimation using permanent scatterers in differential sar interferometry,” *IEEE Transactions on Geoscience and Remote Sensing*, vol. 38, no. 5, pp. 2202–2212, 2000.

A. Ferretti, D. Perissin, C. Prati, and F. Rocca, “On the physical nature of sar permanent scatterers,” in *URSI Commission F Symposium on Microwave Remote Sensing of the Earth, Oceans, Ice and Atmosphere, Ispra, Italy*, 2005, pp. 20–21.

G. Fornaro, A. Pauciullo, and F. Serafino, “Deformation monitoring over large areas with multipass differential sar interferometry: a new approach based on the use of spatial differences,” *International Journal of Remote Sensing*, vol. 30, no. 6, pp. 1455–1478, 2009.

G. Fornaro, F. Lombardini, and F. Serafino, “Three-dimensional multipass sar focusing: Experiments with long-term spaceborne data,” *IEEE Transactions on Geoscience and Remote Sensing*, vol. 43, no. 4, pp. 702–714, 2005.

J. Foster, B. Brooks, T. Cherubini, C. Shacat, S. Businger, and C. Werner, “Mitigating atmospheric noise for insar using a high resolution weather model,” *Geophysical Research Letters*, vol. 33, no. 16, 2006.

G. Franceschetti and R. Lanari, *Synthetic aperture radar processing*. CRC press, 1999.

A. Freeman and S. L. Durden, “A three-component scattering model for polarimetric sar data,” *IEEE Transactions on Geoscience and Remote Sensing*, vol. 36, no. 3, pp. 963–973, 1998.

A. K. Gabriel, R. M. Goldstein, and H. A. Zebker, “Mapping small elevation changes over large areas: differential radar interferometry,” *Journal of Geophysical Research: Solid Earth*, vol. 94, no. B7, pp. 9183–9191, 1989.

F. Gini and F. Lombardini, “Multibaseline cross-track sar interferometry: a signal processing perspective,” *IEEE Aerospace and Electronic Systems Magazine*, vol. 20, no. 8, pp. 71–93, 2005.

——, “Multilook apes for multibaseline sar interferometry,” *IEEE Transactions on Signal Processing*, vol. 50, no. 7, pp. 1800–1803, 2002.

R. Goldstein, “Atmospheric limitations to repeat-track radar interferometry,” *Geophysical research letters*, vol. 22, pp. 2517–2517, 1995.

J. W. Goodman, “Some fundamental properties of speckle,” *JOSA*, vol. 66, no. 11, pp. 1145–1150, 1976.

H. Graven, R. Keeling, S. Piper, P. Patra, B. Stephens, S. Wofsy, L. Welp, C. Sweeney, P. Tans, J. Kelley *et al.*, “Enhanced seasonal exchange of co2 by northern ecosystems since 1960,” *Science*, vol. 341, no. 6150, pp. 1085–1089, 2013.

H. Haberl and K.-H. Erb, "Assessment of sustainable land use in producing biomass," *Renewables-Based Technology: Sustainability Assessment*, pp. 173–192, 2006.

J. O. Hagberg, L. M. Ulander, and J. Askne, "Repeat-pass sar interferometry over forested terrain," *IEEE Transactions on Geoscience and Remote Sensing*, vol. 33, pp. 331–340, 1995.

R. F. Hanssen, *Radar interferometry: data interpretation and error analysis*. Springer Science & Business Media, 2001, vol. 2.

S. Hensley, T. Michel, M. Neumann, M. Lavalle, R. Ahmed, R. Muellerschoen, B. Chapman, S. Oveisgharan, C. Jones, F. Lombardini *et al.*, "Multi-baseline uavsar repeat pass data of the harvard forest," in *Synthetic Aperture Radar, 2012. EUSAR. 9th European Conference on*. VDE, 2012, pp. 109–112.

J. Homer, I. Longstaff, Z. She, and D. Gray, "High resolution 3-d imaging via multi-pass sar," *IEE Proceedings-Radar, Sonar and Navigation*, vol. 149, no. 1, pp. 45–50, 2002.

A. Hooper, H. Zebker, P. Segall, and B. Kampes, "A new method for measuring deformation on volcanoes and other natural terrains using insar persistent scatterers," *Geophysical research letters*, vol. 31, no. 23, 2004.

P. Hyde, R. Nelson, D. Kimes, and E. Levine, "Exploring lidar–radar synergyâpredicting aboveground biomass in a southwestern ponderosa pine forest using lidar, sar and insar," *Remote Sensing of Environment*, vol. 106, no. 1, pp. 28–38, 2007.

M. L. Imhoff, "Radar backscatter/biomass saturation: Observations and implications for global biomass assessment," in *Geoscience and Remote Sensing Symposium, 1993. IGARSS'93. Better Understanding of Earth Environment., International*. IEEE, 1993, pp. 43–45.

M. Imhoff, "Radar backscatter and biomass saturation-ramifications for global biomass inventory ieee transactions on geoscience and remote sensing. 33 (2): 511–518. doi: 10.1109/36.377953 view article pubmed," *NCBI Google Scholar*, 1995.

C. V. Jakowatz and P. Thompson, “A new look at spotlight mode synthetic aperture radar as tomography: imaging 3-d targets,” *IEEE transactions on image processing*, vol. 4, no. 5, pp. 699–703, 1995.

J. R. Justus and S. R. Fletcher, “Global climate change.” Congressional Research Service, Library of Congress, 2001.

T. R. Karl and K. E. Trenberth, “Modern global climate change,” *Science*, vol. 302, no. 5651, pp. 1719–1723, 2003. [Online]. Available: http://science.sciencemag.org/content/302/5651/1719

J. Kellndorfer, W. Walker, L. Pierce, C. Dobson, J. A. Fites, C. Hunsaker, J. Vona, and M. Clutter, “Vegetation height estimation from shuttle radar topography mission and national elevation datasets,” *Remote sensing of Environment*, vol. 93, no. 3, pp. 339–358, 2004.

M. Lavalle, M. Simard, and S. Hensley, “A temporal decorrelation model for polarimetric radar interferometers,” *IEEE Transactions on Geoscience and Remote Sensing*, vol. 50, no. 7, pp. 2880–2888, 2012.

T. Le Toan, A. Beaudoin, J. Riom, and D. Guyon, “Relating forest biomass to sar data,” *IEEE Transactions on Geoscience and Remote Sensing*, vol. 30, no. 2, pp. 403–411, 1992.

J.-S. Lee, “Digital image enhancement and noise filtering by use of local statistics,” *IEEE transactions on pattern analysis and machine intelligence*, no. 2, pp. 165–168, 1980.

——, “Speckle analysis and smoothing of synthetic aperture radar images,” *Computer graphics and image processing*, vol. 17, no. 1, pp. 24–32, 1981.

J.-S. Lee, M. R. Grunes, and G. De Grandi, “Polarimetric sar speckle filtering and its implication for classification,” *IEEE Transactions on Geoscience and remote sensing*, vol. 37, no. 5, pp. 2363–2373, 1999.

J. Li and P. Stoica, *Robust adaptive beamforming*. John Wiley & Sons, 2005, vol. 88.

J. Li, P. Stoica, and Z. Wang, “On robust capon beamforming and diagonal loading,” *IEEE Transactions on Signal Processing*, vol. 51, no. 7, pp. 1702–1715, 2003.

Z. Li, J.-P. Muller, P. Cross, and E. J. Fielding, “Interferometric synthetic aperture radar (insar) atmospheric correction: Gps, moderate resolution imaging spectroradiometer (modis), and insar integration,” *Journal of Geophysical Research: Solid Earth*, vol. 110, no. B3, 2005.

Z. Li, E. J. Fielding, P. Cross, and J.-P. Muller, “Interferometric synthetic aperture radar atmospheric correction: medium resolution imaging spectrometer and advanced synthetic aperture radar integration,” *Geophysical Research Letters*, vol. 33, no. 6, 2006.

S. C. Liew, H. Lim, L. K. Kwoh, and G. K. Tay, “Texture analysis of sar images,” in *Geoscience and Remote Sensing Symposium, 1995. IGARSS’95.’Quantitative Remote Sensing for Science and Applications’, International*, vol. 2. IEEE, 1995, pp. 1412–1414.

H. W. Lilliefors, “On the kolmogorov-smirnov test for normality with mean and variance unknown,” *Journal of the American Statistical Association*, vol. 62, no. 318, pp. 399–402, 1967.

F. Lombardini, M. Pardini, G. Fornaro, F. Serafino, L. Verrazzani, and M. Costantini, “Linear and adaptive spaceborne threedimensional sar tomography: a comparison on real data,” *IET radar, sonar & navigation*, vol. 3, no. 4, pp. 424–436, 2009.

F. Lombardini and A. Reigber, “Adaptive spectral estimation for multibaseline sar tomography with airborne l-band data,” in *International Geoscience and Remote Sensing Symposium*, vol. 3, 2003, pp. III–2014.

R. G. Lorenz and S. P. Boyd, “Robust minimum variance beamforming,” *IEEE Transactions on Signal Processing*, vol. 53, no. 5, pp. 1684–1696, 2005.

Y. Malhi and O. L. Phillips, “Tropical forests and global atmospheric change: a synthesis,” *Philosophical Transactions of the Royal Society of London B: Biological Sciences*, vol. 359, no. 1443, pp. 549–555, 2004.

F. J. Massey Jr, “The kolmogorov-smirnov test for goodness of fit,” *Journal of the American statistical Association*, vol. 46, no. 253, pp. 68–78, 1951.

D. Massonnet and K. L. Feigl, “Discrimination of geophysical phenomena in satellite radar interferograms,” *Geophysical research letters*, vol. 22, no. 12, pp. 1537–1540, 1995.

T. Mette, K. Papathanassiou, I. Hajnsek, and R. Zimmermann, “Forest biomass estimation using polarimetric sar interferometry,” in *Applications of SAR Polarimetry and Polarimetric Interferometry*, vol. 529, 2003.

R. A. Monzingo and T. W. Miller, *Introduction to adaptive arrays.* Scitech publishing, 1980.

A. Moreira, “Digital beamforming: A paradigm shift for spaceborne sar,” in *2013 14th International Radar Symposium (IRS)*, vol. 1. IEEE, 2013, pp. 23–26.

——, “A golden age for spaceborne sar systems,” in *Microwaves, Radar, and Wireless Communication (MIKON), 2014 20th International Conference on.* IEEE, 2014, pp. 1–4.

A. N. Nyoungui, E. Tonye, and A. Akono, “Evaluation of speckle filtering and texture analysis methods for land cover classification from sar images,” *International Journal of Remote Sensing*, vol. 23, no. 9, pp. 1895–1925, 2002.

C. Oliver and S. Quegan, *Understanding synthetic aperture radar images.* SciTech Publishing, 2004.

F. Onn and H. Zebker, “Correction for interferometric synthetic aperture radar atmospheric phase artifacts using time series of zenith wet delay observations from a gps network,” *Journal of Geophysical Research: Solid Earth*, vol. 111, no. B9, 2006.

Y. Pan, R. A. Birdsey, J. Fang, R. Houghton, P. E. Kauppi, W. A. Kurz, O. L. Phillips, A. Shvidenko, S. L. Lewis, J. G. Canadell *et al.*, “A large and persistent carbon sink in the worldâs forests,” *Science*, vol. 333, no. 6045, pp. 988–993, 2011.

K. P. Papathanassiou and S. R. Cloude, “Single-baseline polarimetric sar interferometry,” *IEEE Transactions on Geoscience and Remote Sensing*, vol. 39, no. 11, pp. 2352–2363, 2001.

P. Pasquali, C. Prati, F. Rocca, M. Seymour, J. Fortuny, E. Ohlmer, and A. Sieber, “A 3-d sar experiment with emsl data,” in *Geoscience and Remote Sensing Symposium, 1995. IGARSS’95.’Quantitative Remote Sensing for Science and Applications’, International*, vol. 1. IEEE, 1995, pp. 784–786.

O. L. Phillips and S. L. Lewis, “Recent changes in tropical forest biomass and dynamics,” *Forests and global change. Cambridge University Press, Cambridge*, pp. 77–108, 2014.

P. Piau, “Performances of the 3d-sar imagery,” in *Geoscience and Remote Sensing Symposium, 1994. IGARSS’94. Surface and Atmospheric Remote Sensing: Technologies, Data Analysis and Interpretation., International*, vol. 4. IEEE, 1994, pp. 2267–2271.

B. Puysségur, R. Michel, and J.-P. Avouac, “Tropospheric phase delay in interferometric synthetic aperture radar estimated from meteorological model and multispectral imagery,” *Journal of Geophysical Research: Solid Earth*, vol. 112, no. B5, 2007.

C. L. Quéré, R. J. Andres, T. Boden, T. Conway, R. Houghton, J. I. House, G. Marland, G. P. Peters, G. Van der Werf, A. Ahlström *et al.*, “The global carbon budget 1959–2011,” *Earth System Science Data*, vol. 5, no. 1, pp. 165–185, 2013.

K. Ranson, G. Sun, J. Weishampel, and R. Knox, “Forest biomass from combined ecosystem and radar backscatter modeling,” *Remote Sensing of Environment*, vol. 59, no. 1, pp. 118–133, 1997.

A. Reigber and A. Moreira, “First demonstration of airborne sar tomography using multibaseline l-band data,” *IEEE Transactions on Geoscience and Remote Sensing*, vol. 38, no. 5, pp. 2142–2152, 2000.

E. Rodriguez and J. Martin, “Theory and design of interferometric synthetic aperture radars,” in *IEE Proceedings F-Radar and Signal Processing*, vol. 139, no. 2. IET, 1992, pp. 147–159.

P. A. Rosen, S. Hensley, H. A. Zebker, F. H. Webb, and E. J. Fielding, "Surface deformation and coherence measurements of kilauea volcano, hawaii, from sir-c radar interferometry," *Journal of Geophysical Research: Planets*, vol. 101, no. E10, pp. 23 109–23 125, 1996.

P. A. Rosen, S. Hensley, I. R. Joughin, F. K. Li, S. N. Madsen, E. Rodriguez, and R. M. Goldstein, "Synthetic aperture radar interferometry," *Proceedings of the IEEE*, vol. 88, no. 3, pp. 333–382, 2000.

A. Rosenqvist, M. Shimada, and M. Watanabe, "Alos palsar: Technical outline and mission concepts," in *4th International Symposium on Retrieval of Bio-and Geophysical Parameters from SAR Data for Land Applications*. Innsbruck, Austria, 2004, pp. 1–7.

A. Rosenqvist, M. Shimada, N. Ito, and M. Watanabe, "Alos palsar: A pathfinder mission for global-scale monitoring of the environment," *IEEE Transactions on Geoscience and Remote Sensing*, vol. 45, no. 11, pp. 3307–3316, 2007.

K. Sarabandi and Y.-C. Lin, "Simulation of interferometric sar response for characterizing the scattering phase center statistics of forest canopies," *IEEE Transactions on Geoscience and Remote Sensing*, vol. 38, no. 1, pp. 115–125, 2000.

C. Schmullius and D. Evans, "Review article synthetic aperture radar (sar) frequency and polarization requirements for applications in ecology, geology, hydrology, and oceanography: A tabular status quo after sir-c/x-sar," *International Journal of Remote Sensing*, vol. 18, no. 13, pp. 2713–2722, 1997.

Z. She, D. Gray, R. Bogner, J. Homer, and I. Longstaff, "Three-dimensional space-borne synthetic aperture radar (sar) imaging with multiple pass processing," *International Journal of Remote Sensing*, vol. 23, no. 20, pp. 4357–4382, 2002.

S. Silver, *Microwave antenna theory and design*. Iet, 1949, no. 19.

M. Simard, K. Zhang, V. H. Rivera-Monroy, M. S. Ross, P. L. Ruiz, E. Castañeda-Moya, R. R. Twilley, and E. Rodriguez, "Mapping height and biomass of mangrove forests in everglades national park with srtm elevation data," *Photogrammetric Engineering & Remote Sensing*, vol. 72, no. 3, pp. 299–311, 2006.

M. I. Skolnik, "Radar handbook," 1970.

M. Soumekh, *Synthetic aperture radar signal processing*. New York: Wiley, 1999.

P. Stoica, Z. Wang, and J. Li, "Robust capon beamforming," in *Signals, Systems and Computers, 2002. Conference Record of the Thirty-Sixth Asilomar Conference on*, vol. 1. IEEE, 2002, pp. 876–880.

B. D. Tapley, G. H. Born, and M. E. Parke, "The seasat altimeter data and its accuracy assessment," *Journal of Geophysical Research: Oceans*, vol. 87, no. C5, pp. 3179–3188, 1982.

S. Tebaldini, "Forest sar tomography: a covariance matching approach," in *2008 IEEE Radar Conference*. IEEE, 2008, pp. 1–6.

J. Tollefson, "Climate: Counting carbon in the amazon," *Nature*, vol. 461, no. 7267, p. 1048, 2009.

R. Touzi and A. Lopes, "Statistics of the stokes parameters and of the complex coherence parameters in one-look and multilook speckle fields," *IEEE Transactions on Geoscience and Remote Sensing*, vol. 34, no. 2, pp. 519–531, 1996.

F. T. Ulaby, F. Kouyate, B. Brisco, and T. L. Williams, "Textural infornation in sar images," *IEEE Transactions on Geoscience and Remote Sensing*, no. 2, pp. 235–245, 1986.

B. D. Van Veen and K. M. Buckley, "Beamforming: A versatile approach to spatial filtering," *IEEE assp magazine*, vol. 5, no. 2, pp. 4–24, 1988.

W. S. Walker, J. M. Kellndorfer, and L. E. Pierce, "Quality assessment of srtm c-and x-band interferometric data: Implications for the retrieval of vegetation canopy height," *Remote Sensing of Environment*, vol. 106, no. 4, pp. 428–448, 2007.

U. Wegmuller and C. L. Werner, "Sar interferometric signatures of forest," *IEEE Transactions on Geoscience and Remote Sensing*, vol. 33, no. 5, pp. 1153–1161, 1995.

R. Whittaker, F. Bormann, G. Likens, and T. Siccama, "The hubbard brook ecosystem study: forest biomass and production," *Ecological monographs*, vol. 44, no. 2, pp. 233–254, 1974.

C. A. Wiley, "Pulsed doppler radar methods and apparatus," Jul. 20 1965, uS Patent 3,196,436.

C. Willey, "Synthetic aperture radars–a paradigm for technology evolution," *IEEE Trans. Aerospace Elec. Sys*, vol. 21, pp. 440–443, 1985.

I. H. Woodhouse, "Predicting backscatter-biomass and height-biomass trends using a macroecology model," *IEEE Transactions on Geoscience and remote sensing*, vol. 44, no. 4, pp. 871–877, 2006.

H. A. Zebker and R. M. Goldstein, "Topographic mapping from interferometric synthetic aperture radar observations," *Journal of Geophysical Research: Solid Earth*, vol. 91, no. B5, pp. 4993–4999, 1986.

H. A. Zebker and P. Rosen, "On the derivation of coseismic displacement fields using differential radar interferometry: The landers earthquake," in *Geoscience and Remote Sensing Symposium, 1994. IGARSS'94. Surface and Atmospheric Remote Sensing: Technologies, Data Analysis and Interpretation., International*, vol. 1. IEEE, 1994, pp. 286–288.

H. A. Zebker and J. Villasenor, "Decorrelation in interferometric radar echoes," *IEEE Transactions on geoscience and remote sensing*, vol. 30, no. 5, pp. 950–959, 1992.

H. A. Zebker, P. A. Rosen, and S. Hensley, "Atmospheric effects in interferometric synthetic aperture radar surface deformation and topographic maps," *Journal of Geophysical Research: Solid Earth*, vol. 102, no. B4, pp. 7547–7563, 1997.

H. A. Zebker, S. Hensley, P. Shanker, and C. Wortham, "Geodetically accurate insar data processor," *IEEE Transactions on Geoscience and Remote Sensing*, vol. 48, no. 12, pp. 4309–4321, 2010.

X. X. Zhu and R. Bamler, “Super-resolution power and robustness of compressive sensing for spectral estimation with application to spaceborne tomographic sar,” *IEEE Transactions on Geoscience and Remote Sensing*, vol. 50, no. 1, pp. 247–258, 2012.